Search for best globular cluster candidates for H.E.S.S. and CTA

H Ndiyavala

26403366

Dissertation submitted in partial fulfilment of the requirements for the degree *Magister Scientiae* in Space Physics at the Potchefstroom Campus of the North-West University

Supervisor: Dr PP Krüger

Co-supervisor: Prof C Venter

November 2016

Dedication

This thesis is dedicated to my Heavenly Father, my God and Lord of my life.

"The Lord is my strength and my shield; my heart trusts in Him, and He helps me. My heart leaps for joy, and with my song I praise Him" (Psalm 28:7, New International Version (NIV) Bible).

It is also dedicated to my mother, who taught me that even the largest task can be accomplished if it is done one step at a time.

Acknowledgements

- Many thanks to my advisers Dr Paulus Krüger and Prof. Christo Venter for the continuous support of my MSc study, for their patience, motivation, and immense knowledge. Their guidance helped me during the time of research and writing of this thesis. I could not have imagined having better advisers and mentors for my MSc study.

- My sincere appreciation also goes to members and management of the Department of Physics and the Centre for Space Research at the North-West University (NWU) in South Africa for providing the facilities and a good atmosphere that led to the completion of my MSc study. A big thank you to Mrs Petro Sieberhagen for her kind and daily assistance on the administrative side. I would also like to thank Mr Mathew Holleran for his expertise in information technology and his willingness to help with settling of PC end-user issues. A big thank you to my friends Tania Garrigoux and Hassan Abdalla for many informative discussions.

- I would like to express my sincere gratitude to Mr Isak Davids, Dr Michael Backes and Dr Riaan Steenkamp from the University of Namibia (UNAM) for having stimulated my interest for postgraduate studies in Space Physics.

- I would also like to thank my family: my parents, Paulina Nakale and late Erastus Ndiyavala, and my sisters for supporting me spiritually throughout the writing of this dissertation and my life in general.

The financial assistance of the German Academic Exchange Service (DAAD) and North-West University towards this work is hereby acknowledged. Special thanks goes to Ms Martina Williams, the DAAD representative in Namibia, for her prompt and motherly approach in handling financial matters throughout my studies.

"In the beginning, there was darkness, and then – Bang! Giving birth to an endless expanding existence of time, space, and matter. Every day new discoveries are unlocking the mysterious, the mind-blowing, the deadly secrets of a place we call the Universe."

From "The Universe" series.

ABSTRACT

Globular clusters (GCs) are multi-wavelength objects. About 20 of these systems have been detected by the *Fermi* Large Area Telescope in the GeV band, whilst the ground-based Cherenkov telescope, the High Energy Stereoscopic System (H.E.S.S.), which is operated in a pointing mode at energies above 100 GeV, has only seen a single GC within our Galaxy, i.e., Terzan 5. H.E.S.S. has accumulated more data since their previous published analysis and thus I reanalysed the H.E.S.S. data for 15 non-detected GCs as well as for Terzan 5. I confirmed the detection of Terzan 5 (with a significance of 7.1σ for hard cuts) and that no individual GC or stacking analysis shows any significant excess emission. I found flux upper limits for the non-detected sources that are consistent with the published results. I furthermore present results from an emission code that models the spectral energy density of GCs by solving a Fokker-Planck-type transport equation for leptons and calculate inverse Compton and synchrotron radiation to make predictions for the flux expected from GCs. I performed a parameter study and constrained model parameters for three GCs using γ-ray and X-ray data. I accumulated parameters for all 16 Galactic GCs and used the code to study their detectability with H.E.S.S. and the Cherenkov Telescope Array (CTA), ranking them according to their predicted TeV fluxes. The spectrum of each cluster and therefore the detectability ranking is very sensitive to the choice of parameters. I expect H.E.S.S. to detect two more GCs, i.e., 47 Tucanae and NGC 6388, if the clusters are observed for 100 hours. The five most promising GCs for CTA are NGC 6388, 47 Tucanae, Terzan 5, Djorg 2, and Terzan 10. I lastly expect CTA to detect more than half of the known Galactic population, depending on observation time and model parameters.

Key words: globular clusters: general - pulsars: general - radiation mechanisms: non-thermal

OPSOMMING

Geslote stertrosse (GS) is multi-golflengte-voorwerpe. Sowat 20 van hierdie stelsels is waargeneem deur *Fermi Large Area Telescope* in die GeV-band. Aan die ander kant het die grond-gebaseerde Cherenkov-teleskoop, die *High Energy Stereoscopic System* (H.E.S.S.), wat in 'n gerigte modus by energieë meer as 100 GeV bedryf word, net 'n enkele GS binne die Melkweg waargeneem, d.i., Terzan 5. H.E.S.S. het meer data sedert hul vorige publikasie geakkumuleer. Dus het ek H.E.S.S.-data vir 15 nie-waargenome GSe asook vir Terzan 5 geheranaliseer. Ek kon die deteksie van Terzan 5 bevestig (met 'n beduidendheid van 7.1σ vir harde snitte) asook dat geen individuele GS-analise of stapel-ontleding beduidende straling toon nie. Ek het vloedbogrense vir die nie-waargenome bronne verkry wat in ooreenstemming met gepubliseerde resultate is. Ek beskryf voorts resultate van 'n stralingskode wat die spektrale energiedigtheid van GSe modelleer deur die oplossing van 'n Fokker-Planck-tipe transportvergelyking vir leptone en berekening van inverse-Compton- en synchrotron-straling, om sodoende voorspellings te maak vir die verwagte vloed van GSe. Ek voltooi 'n parameterstudie en beperk model-parameters vir sommige GSe m.b.v. γ-straal- en X-straal-data. Ek het parameters vir al 16 Galaktiese GSe versamel en die kode gebruik om hul waarneembaarheid met H.E.S.S. en die *Cherenkov Telescope Array* (CTA) te bestudeer. Ek kon ook 'n rangorde volgens hul voorspelde TeV-vloed opstel. Die vloedvoorspelling en dus die waarneembaarheidsposisie is baie sensitief vir die parameterskeuse. Ek verwag dat H.E.S.S. nog twee GSe, d.i., 47 Tucanae en NGC 6388, sal opspoor indien die trosse vir 100 ure waargeneem word. Die vyf mees belowende GSe vir waarneming met CTA is NGC 6388, 47 Tucanae, Terzan 5, Djorg 2 en Terzan 10. Ek verwag laastens dat CTA meer as die helfte van die bekende Galaktiese GS-populasie sal waarneem, afhangende van die toegewese waarnemingstyd en modelparameters.

Sleutelwoorde: geslote stertrosse: algemeen - pulsare: algemeen - stralingsmeganismes: nie-termies

Nomenclature

Each of the following listed abbreviations will be written out in full the first time it appears within the main text.

Those abbreviations that appear only once are not listed.

CMB	Cosmic Microwave Background
CR	Curvature Radiation
CTA	Cherenkov Telescope Array
CVS	Concurrent Versions System
FGST	*Fermi* Gamma-ray Space Telescope
FoV	Field of View
GCs	Globular Clusters
HAP	H.E.S.S. Analysis Package
HB	Horizontal Branch
H.E.S.S.	High Energy Stereoscopic System
IACT	Imaging Atmospheric Cherenkov Telescope
IC	Inverse Compton
ICS	Inverse Compton Scattering
K-N	Klein-Nishina
LAT	Large Area Telescope
LMXBs	Low Mass X-ray Binaries
LOS	Line-Of-Sight
MAGIC	Major Atmospheric Gamma Imaging Cherenkov
MSPs	Millisecond Pulsars
MSTO	Main Sequence Turn-Off
PSF	Point Spread Function
SED	Spectral Energy Distribution
SR	Synchrotron Radiation
TMVA	Toolkit Multivariate Data Analysis
VERITAS	Very Energetic Radiation Imaging Telescope Array System
VHE	Very High Energy

Contents

List of Figures

List of Tables

Chapter 1

Introduction

In recent years, the field of γ-ray astrophysics has rapidly developed. This is due to the impressive list of ground-based Imaging Atmospheric Cherenkov Telescopes (IACTs) and space-based instruments that are now operational. The currently operating ground missions committed to γ-ray astrophysics include the High Energy Stereoscopic System (H.E.S.S.), Very Energetic Radiation Imaging Telescope Array System (VERITAS), and the Major Atmospheric Gamma Imaging Cherenkov (MAGIC) telescopes that operate in the 100 GeV $-$ 100 TeV band. The launch of the *Fermi* Large Area Telescope (LAT), which is a γ-ray satellite orbiting Earth and operating at 20 MeV $-$ 300 GeV, has led to many discoveries, including the detection of GeV γ-rays from Globular clusters (GCs). The *Fermi* LAT has detected about 20 of these systems (Nolan et al., 2012). Complementary to *Fermi*, there is *AstroRivelatore Gamma a Immagini Leggero (AGILE)*, which is an X-ray and γ-ray instrument; however it has not detected any GC to date due to its lower sensitivity. The ground-based Cherenkov telescope, H.E.S.S., which is operated in a pointing mode (limiting the fraction of the sky it can annually observe), has only seen a single cluster within our Galaxy, i.e., Terzan 5 (Abramowski et al., 2011). Other Cherenkov telescopes could only produce upper limits (e.g., Anderhub et al. 2009). The future Cherenkov Telescope Array (CTA) will be about 10 times more sensitive than H.E.S.S. and is expected to see TeV emission from a few more GCs. GCs have also been detected in radio (e.g., Clapson et al. 2011) and as diffuse X-ray sources (e.g., Eger et al. 2010; Eger & Domainko 2012; Wu et al. 2014). They thus form an important class of Galactic emitters of broadband emission, and are exciting targets for deeper future observations with more sensitive telescopes.

Several models exist that predict the multi-wavelength spectrum radiated by GCs. Bednarek & Sitarek (2007) considered a scenario where leptons are accelerated by millisecond pulsars (MSPs) at relativistic shocks that are created during collisions of the pulsar winds inside the cores of these clusters. Harding et al. (2005) and Venter & de Jager (2005) furthermore modelled the cumulative GeV flux by assuming a pair-starved polar cap electric field. Venter & de Jager (2008) modelled the cumulative pulsed curvature radiation (CR) from 100 such pulsars by randomising over MSP geometry (magnetic inclination and observer angles) as well as period and period time derivative. Venter & de Jager (2010) refined this approach and Venter et al. (2009a) could predict the GeV spectrum of 47 Tucanae within a factor of two in both energy and flux level, prior to its detection by *Fermi* LAT. Cheng et al. (2010) considered an alternative scenario to produce GeV and TeV emission by calculating inverse Compton (IC) radiation from electrons and positrons upscattering the cosmic microwave background (CMB), stellar photons, and the Galactic background. There are also hadronic models that attempt to explain the observed TeV emission from Terzan 5 (Domainko, 2011).

1.1 Problem statement

As mentioned above, H.E.S.S. has detected only a single Galactic GC. Moreover, there are many unanswered questions about GCs. For example, since Terzan 5 is the only GC seen in VHE band, is it special, i.e., exceptionally bright? How many GCs are expected to be visible for H.E.S.S.? Will more Galactic GCs be visible to H.E.S.S. and CTA? Is it worthwhile allocating more observing time of H.E.S.S. to GCs? Since CTA will be ten times more sensitive than H.E.S.S., one would also like to know how many Galactic GCs might be detected by CTA. I have access to a leptonic (spherically symmetric, steady-state) model (Kopp et al., 2013) that has not yet been applied to different Galactic GCs and hence, in this work I will apply the model to several GCs. Another unanswered question is how the model behaves in multi-dimensional space if one changes parameters? Since there are some new multi-wavelength data, I will attempt to constrain the model parameters. These questions therefore prompt us to employ the spherically symmetric model to study the GC population detectability by H.E.S.S. and CTA and also to constrain the model parameters.

1.2 Research goal

My focus is on γ-rays, but I will also consider multi-wavelength data in the lower energy bands. I will analyse data taken with the H.E.S.S. telescope to search for the GCs, since the data on GCs have increased in the last years. My research aim is to study the detactability of GCs with H.E.S.S. and CTA. To do so I will accumulate the necessary parameters for 16 Galactic GCs, taking into account errors on these quantities, and then run a leptonic model to make predictions for the γ-ray flux expected from each GC for H.E.S.S. and CTA. The model I will use is a multi-zone, steady-state, spherically symmetric model that calculates the particle transport (including diffusion and radiation losses) and predicts the spectral energy distribution (SED) from GCs for a very broad energy range by considering synchrotron radiation (SR) as well as IC emission. Using this model I will identify GC candidates for further observation by H.E.S.S. and CTA by ranking them according to their predicted TeV fluxes. I will use the model results to do a population study (i.e., to determine how many GCs should be visible for CTA) and to select the five most promising sources for future observations by CTA. I will also constrain model parameters for the different sources using γ-ray and X-ray data and determine various parameters' values compatible with upper limits or measurements. In the process I will also be testing the model viability.

The rest of the thesis is structured as follows:

In **Chapter 2** the reader is presented with the necessary background of GCs and MSPs. I will summarise the characteristics and evolution of GCs. I will also discuss non-thermal radiation mechanisms and the current TeV γ-ray instruments.

In **Chapter 3** I present my new results of H.E.S.S. data analysis of GCs and also provides a discussion on a previous analysis by independent researchers.

In **Chapter 4** I will review the existing multi-wavelength spectral models for GCs, and the numerical model I focus on, including the definition of model parameters.

In **Chapter 5** I present a parameter study to further investigate the model's behaviour.

In **Chapter 6** I will present a list of the best candidate sources as predicted by the model for CTA (in terms of predicted VHE flux). The results of searches for the top candidates in H.E.S.S. data will also be presented. Finally, I will also constrain model parameters using multi-wavelength data.

Chapter 7 provides a conclusion of what has been achieved during the course of this study. The

main findings of the data analysis and parameter study will be presented, evaluated, and discussed. The implications of the results, and the future prospects will also be presented.

Chapter 2

Theoretical background

In this chapter, I will discuss some background on GCs and MSPs. I will give the definition of a GC and summarise its characteristics and evolution. I will then discuss SR and IC scattering, which are non-thermal radiation processes expected to operate in GCs, as well as (thermal) blackbody radiation. I will lastly discuss the H.E.S.S. telescopes and the future CTA, since the focus of this study is on the VHE γ-ray waveband.

2.1 Globular clusters

GCs are among the most ancient bound stellar systems in the Universe, consisting of $10^4 - 10^6$ stars (e.g., Lang 1992). An example, a famous cluster can be seen in Figure 2.1. They are normally associated with a host galaxy and most galaxies, including the Milky Way, are penetrated and surrounded by a system of GCs. There are nearly 160 known Galactic GCs (Harris, 2010) and they are spherically distributed about the Galactic Centre (Figure 2.2) lying at an average radius of $\sim$ 12 kpc. Galactic GCs have typical ages of 13 Gyr (placing a lower limit on the age of the Universe), with an age spread of less than 5 Gyr (Carretta et al., 2000). They are thus thought to form during the early stages of galaxy formation. The ages of GCs in other galaxies such as the small and large Magellanic clouds (SMC and LMC) are estimated to be less than 3 Gyr (Mould & Aaronson, 1979; Milone et al., 2009). Red giant stars, which have evolved beyond the main sequence, are the brightest members of GCs. GCs also contain exotic stellar members such as black holes, MSPs, white dwarfs, and cataclysmic variables. The peculiar properties of GCs have been useful in diverse

astrophysical disciplines such as cosmology, galaxy formation, stellar evolution, dynamics, as well as binary and variable stars (Harris, 1996, 2010). GCs are multi-wavelength objects and thus are visible from radio to γ-rays (see Figure 2.1 for an optical image of 47 Tucanae).

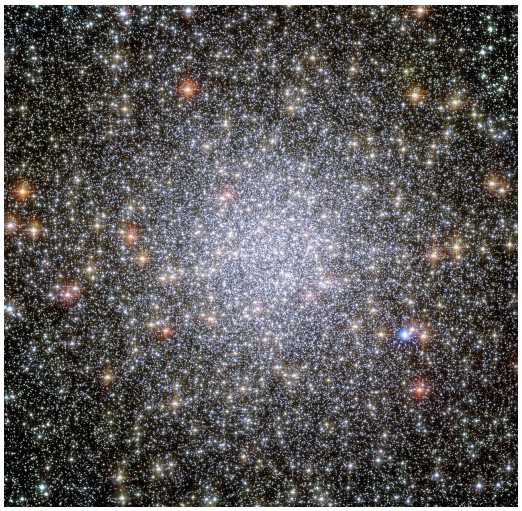

Figure 2.1: Hubble Space Telescope image of the second brightest Galactic GC in the night sky, i.e., 47 Tucane (https://en.wikipedia.org/wiki/File:Globular_cluster_47_Tucanae.jpg).

2.1.1 Stellar Populations in Globular Clusters, Distances, and Age Estimates

The stars in individual GCs have been formed at the same time, sharing the same chemical abundance, and lying at the same distance from us, thus GCs were originally thought to contain very homogeneous stellar populations (differing mostly in mass). GCs have structural properties like core, tidal, and half-mass radius.

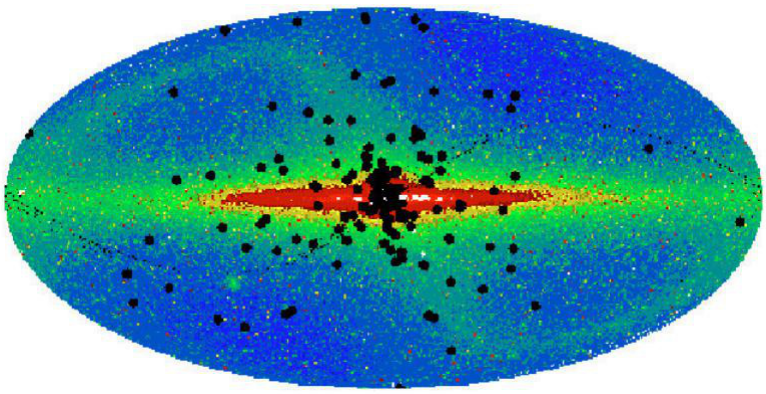

Figure 2.2: This figure shows the distribution of GCs in the Galaxy. The black circles represent the positions of GCs (Harris, 1996) on top of the COBE FIRAS 2.2 micron map of the Galaxy using a Mollweide projection (Benacquista, 2002).

The core radius is the distance from the centre of the cluster at which the apparent surface brightness of the cluster reduces by half. The tidal radius is the distance from the cluster core beyond which the gravitational influence of the Galaxy is larger than that of the GC, and the half-mass radius is the radius from the core including half of the total mass of the cluster.

Figure 2.3 shows the colour-magnitude diagram (CMD) of a typical GC, indicating a stellar population forming a distinct main sequence, main sequence turnoff (MSTO), horizontal and red-giant branch, RR Lyrae variable stars, and white dwarfs, indicating the luminosity and the surface colour (as well as summarising their evolution).

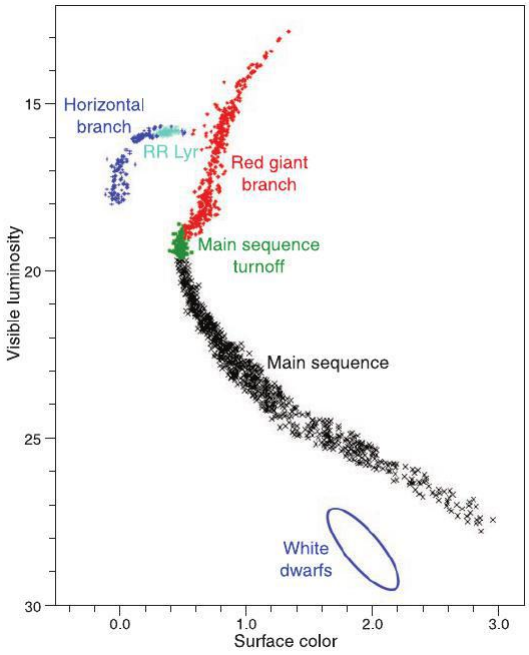

Figure 2.3: Luminosity versus the surface colour of the stars for a typical GC (Krauss & Chaboyer, 2003).

Since Galactic GCs are so old, most of the stars with masses above $\sim 0.8 M_{\odot}$ have already left the main sequence, and are on the red giant branch. The more massive stars have evolved past the red-giant and horizontal branches (HBs) and have become compact remnants (e.g., white dwarfs and MSPs) with low luminosity. The distance, age, and chemical composition, as well as other properties of GCs are estimated by measuring the magnitude of the MSTO. This is then compared to stellar evolutionary models.

Knowing the distance to a GC helps to determine the luminosity of its turnoff stars. There are various methods that can be used to estimate this distance. All of these methods depend on

different assumptions and calibration steps. The most common method for estimating the distance to the cluster involves "standard candles". In this method, one makes the assumption that some class of stars has the same intrinsic luminosity. The apparent luminosity (flux) of this class of stars is then observed and the distance to the GC is determined by comparing these two quantities. This has been done by using the HB stars (Gratton, 1998), which are stars burning helium into carbon in their cores, RR Lyrae stars (Benedict et al., 2002), which are a subclass of HB stars, main sequence stars (Chaboyer, 1999), and white dwarfs (Renzini et al., 1996). This approach has been successfully performed by determining the intrinsic luminosity of the standard candle accurately by using geometric methods or theoretical models. There are also other techniques for determining the distance to GCs such as studying the internal dynamics of the stars in GCs, and the statistical parallax technique (see Krauss & Chaboyer 2003).

Iben & Renzini (1984) estimated the age of the GC M9 to be 16 ± 3.5 Gyr, and the uncertainty was based on the uncertainty in visual magnitude $\triangle M(V)$. When they chose other values for the abundance of helium, the estimated age dropped to $\sim 14 \pm 3.5$ Gyr. The age of a GC cannot be accurately determined better than about ± 4 Gyr, if one only takes the HB and the absolute luminosities of the MSTO into account. Van den Berg et al. (1996) discussed the uncertainties in determining the age of the oldest GCs. The older stars (typically having a lower metallicity) have ages ~ 15 Gyr. Their estimated age decreases by 7% when helium diffusion is taken into account. Jimenez et al. (1996) used the HB morphology method in their study of M22, M5, M68, M107, M72, M92, M3, and 47 Tucanae. The estimated age of the oldest GCs was 13.5 ± 2 Gyr. The effect of helium diffusion and 1σ uncertainty in each of the parameters of mass and helium content give a lower limit for the age of the oldest cluster of 9.7 Gyr. Jimenez (1998) used the luminosity function method and obtained an age of M55 of $12 \pm 0,5$ Gyr. Strader et al. (2005) mention that GCs have ages of ~ 10 Gyr with an uncertainty of ~ 2 Gyr. Isochrone fitting, HB morphology, luminosity-function (Jimenez, 1998), and Bayesian-estimation (Jørgensen & Lindegren, 2005) methods are used to compute the ages of GCs.

2.1.2 Millisecond pulsars in globular clusters

Low-mass X-ray binaries (LMXBs), which are thought to be the progenitors of MSPs, are one stellar-type member occurring in GCs. Their presence in GCs is thought to be due to the ability of stars to form such systems via dynamical encounters, which correlates with the stellar encounter

rate (Gendre et al., 2003). Their abundance therefore implies the presence of a large number of GC MSPs. Abdo et al. (2010) indeed found a linear correlation between the inferred number of γ-ray MSPs and encounter rate, noting that $2\,600 - 4\,700$ Galactic GC MSPs should be observable in γ-rays. There is also a correlation between the number of radio GC MSPs and encounter rate (providing evidence that stellar dynamical interaction is needed for the formation of MSPs in GCs) as well as metallicity (i.e., the latter is indicative of higher star formation rates, and thus higher rates of supernovae that leads to more MSPs); see Hui et al. (2010). Furthermore, according to Hui et al. (2011), the MSP γ-ray luminosity correlates with encounter rate as well as with metallicity, which establishes a link between the GC γ-ray emission and their embedded population of MSPs (also validating idea that MSPs are the progeny of LMXBs). About 146 GC MSPs have been detected in 28 clusters[1], with 25 MSPs being detected in 47 Tucanae (Pan et al., 2016) and 34 MSPs in Terzan 5 (Massari et al., 2013). Figure 2.4 shows the catalogued distribution of the number of X-ray and radio MSPs detected in 26 GCs. This abundance of GC MSPs provides the basis for our spectral GC model (Chapter 4), which assumes that MSPs provide relativistic particles that can radiate via SR and IC (see Section 2.2).

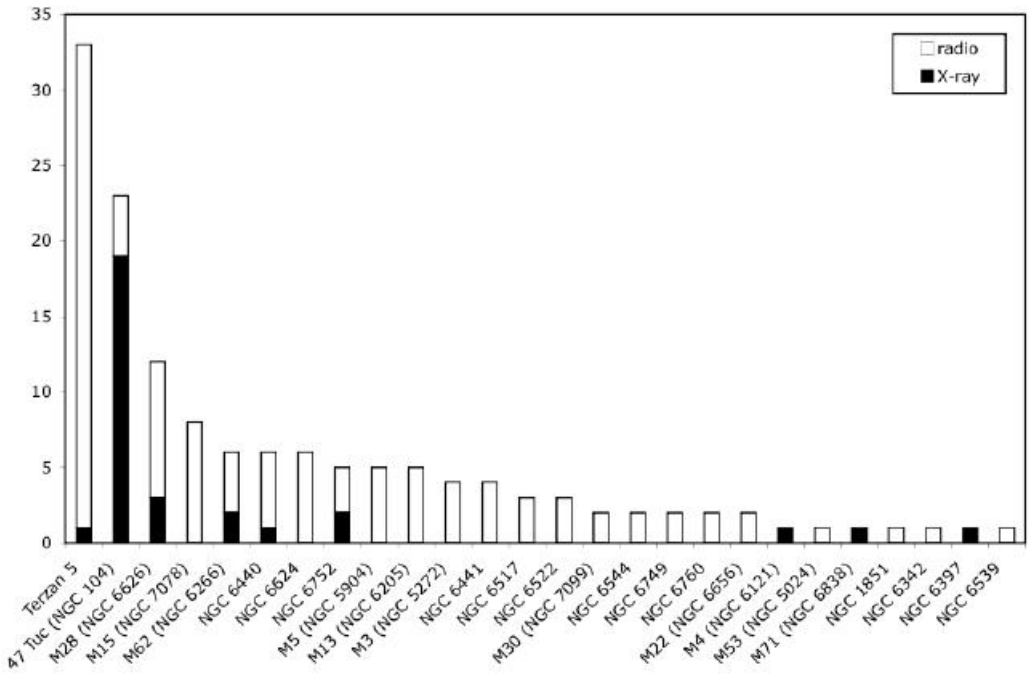

Figure 2.4: The number of radio and X-ray MSPs detected in several Galactic GCs (Becker et al., 2010).

[1] http://www.naic.edu/~pfreire/GCpsr.html

2.2 Radiation mechanisms

It is commonly believed that CR, SR, and IC are the three main mechanisms responsible for radiation from MSPs in GCs. CR is a primary (direct) pulsed emission component from the magnetospheres of pulsars. SR and IC are secondary (indirect) unpulsed emissions that occur when pulsars inject particles into the GCs and these radiate as they move through the cluster. I will not discuss CR because it is pulsed, and originates at a very localised site (within MSP magnetospheres). In this work I consider unpulsed and diffuse SR and IC emissions only. These two processes are described below. I also discuss blackbody emission in Section 2.2.3.

2.2.1 Inverse Compton scattering

During IC scattering, a photon scattered by a moving electron gains energy (i.e., this is a way of transferring energy and momentum from the electron to the photon). There are two IC regimes that are called the Thomson and the Klein-Nishina regime.

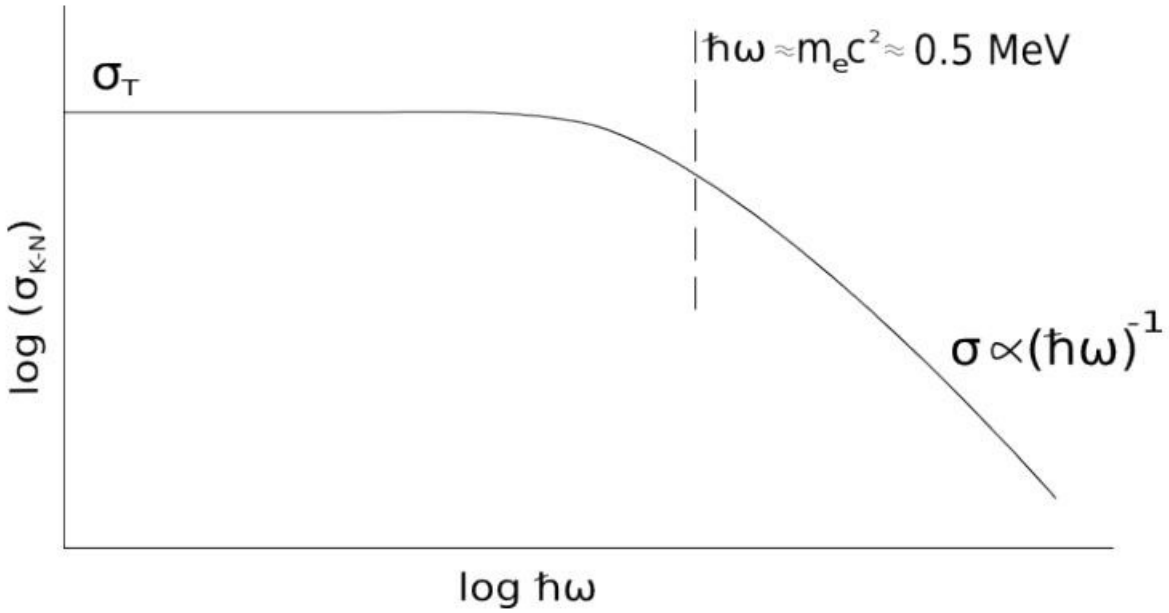

Figure 2.5: Aschematic diagram illustrating the dependence of the IC cross-section upon photon energy, with σ_T the Thomson cross section and σ_{KN} the Klein Nishina cross section (Longair, 1992).

Assume one is in the electron's rest frame and notes the energy ϵ' of the incoming photon in that

frame. If

$$\epsilon' \ll m_{\rm e}c^2, \tag{2.1}$$

where $m_{\rm e}$ is the mass of the electron and c is the speed of light, we are in the Thomson regime. Conversely, in the Klein-Nishina regime

$$\epsilon' \gg m_{\rm e}c^2. \tag{2.2}$$

For an isotropic distribution of incident photons, the average scattered photon energy $\langle\epsilon_1\rangle$ in the laboratory frame in the Thomson regime is (Blumenthal & Gould, 1970)

$$\langle\epsilon_1\rangle = \frac{4}{3}\gamma_{\rm e}^2\epsilon, \tag{2.3}$$

where ϵ is the energy of the soft (incident) photons and $\gamma_{\rm e}$ is the electron's Lorentz factor. The average scattered photon energy ϵ_1 in the lab frame in the Klein-Nishina (K-N) regime is (Blumenthal & Gould, 1970)

$$\langle\epsilon_1\rangle \sim \gamma_{\rm e}m_{\rm e}c^2. \tag{2.4}$$

The total energy loss rate of a single electron in the Thomson regime after averaging over electron direction is (Blumenthal & Gould, 1970)

$$P_{\rm ICS} = -\left(\frac{dE_{\rm e}}{dt}\right)_{\rm T} = \frac{4}{3}\sigma_{\rm T}c\beta^2\gamma_{\rm e}^2U_{\rm ph}, \tag{2.5}$$

where $\sigma_{\rm T} = (8\pi/3)r_0^2 = 6.65\times10^{-25}{\rm cm}^2$ is the Thomson cross section (Rybicki & Lightman, 1979), with r_0 the classical electron radius, $r_0 = e^2/m_{\rm e}c^2$, e the charge of the electron, and $U_{\rm ph}$ is the target photon energy density. Blumenthal & Gould (1970) derived the scattered photon distribution in the Thomson limit as

$$\frac{dN_{\gamma_{\rm e},\epsilon}}{dtd\epsilon_1} = \frac{\pi r_0^2 c}{2\gamma_{\rm e}^4}\frac{n(\epsilon)d\epsilon}{\epsilon^2}\left(2\epsilon_1\ln\frac{\epsilon_1}{4\gamma_{\rm e}^2\epsilon} + \epsilon_1 + 4\gamma_{\rm e}^2\epsilon - \frac{\epsilon_1^2}{2\gamma_{\rm e}^2\epsilon}\right), \tag{2.6}$$

where $n(\epsilon)$ is the number density of photons assuming an isotropic target photon field and an isotropic electron distribution. In the K-N regime, the total K-N cross-section is (Rybicki & Light-

man, 1979)

$$\sigma_{\rm KN} = \frac{3}{4}\sigma_{\rm T}\Big[\frac{1+x}{x^3}\Big(\frac{2x(1+x)}{1+2x} - \ln(1+2x)\Big) + \frac{1}{2x}\ln(1+2x)\frac{1+3x}{(1+2x)^2}\Big], \tag{2.7}$$

where $x \equiv h\nu/m_{\rm e}c^2$. In the K-N regime, the energy loss rate of a single electron for a blackbody photon distribution with temperature T as given by Blumenthal & Gould (1970) is

$$-\Big(\frac{dE}{dt}\Big)_{\rm KN} = \frac{1}{6}\pi r_0^2\frac{(m_{\rm e}ck_{\rm B}T)^2}{\hbar^3}\Big(\ln\frac{4\gamma_{\rm e}k_{\rm B}T}{m_{\rm e}c^2} - \frac{5}{6} - C_E - C_l\Big), \tag{2.8}$$

where $k_{\rm B}$ is the Boltzmann constant, $C_E = 0.5772$, and

$$C_l = \frac{6}{\pi^2}\sum_{k=2}^{\infty}\frac{\ln k}{k^2} = 0.5700.$$

Jones (1968) obtained the general equation for the scattered photon spectrum per electron as

$$\frac{dN_{\gamma,\epsilon}}{dtdE_\gamma} = (\gamma_{\rm e}m_{\rm e}c^2)\frac{dN_{\gamma,\epsilon}}{dtd\epsilon_1} = \frac{2\pi r_0^2 m_{\rm e}c^3 n(\epsilon)d\epsilon}{\gamma_{\rm e}\epsilon}\Big[2q\ln q + (1+2q)(1-q) + \frac{1}{2}\frac{(\Gamma_{\rm e}q)^2}{1+\Gamma_{\rm e}q}(1-q)\Big], \tag{2.9}$$

where $E_\gamma = \epsilon_1/\gamma_{\rm e}m_{\rm e}c^2$, $\Gamma_{\rm e} = 4\gamma_{\rm e}\epsilon/m_{\rm e}c^2$, and $q = E_\gamma/\Gamma_{\rm e}(1-E_\gamma)$ is a dimensionless parameter that determines the scattering regime. The spectrum of Compton-scattered photons by an electron distribution $N_{\rm e}$ is obtained by integrating the product of the electron distribution and Equation (2.9) over the electron Lorentz factor $\gamma_{\rm e}$ and soft-photon energy ϵ

$$\Big(\frac{dN_\gamma}{dtd\epsilon_1}\Big)_{\rm tot} = \iint N_{\rm e}(\gamma_{\rm e})d\gamma_{\rm e}\Big(\frac{dN_{\gamma,\epsilon}}{dtd\epsilon_1}\Big), \tag{2.10}$$

with the differential number of electrons per γ-interval $dN_{\rm e} = N_{\rm e}(\gamma_{\rm e})d\gamma_{\rm e}$ (Blumenthal & Gould, 1970) and the last factor in the integrand is defined in Equation (2.9). If the electron spectrum is described by a power-law distribution function, i.e., $N_{\rm e}(\gamma_{\rm e}) \propto \gamma_{\rm e}^{-p}$, then the spectrum of the scattered photons is also a power law. In the Thomson limit $\Big(\frac{d\dot{N}_\gamma}{d\epsilon_1}\Big)_{\rm tot} \propto \epsilon_1^{-(p+1)/2}$ and in the extreme K-N limit $\Big(\frac{d\dot{N}_\gamma}{d\epsilon_1}\Big)_{\rm tot} \propto \epsilon_1^{-(p+1)}$ (Rybicki & Lightman, 1979).

2.2.2 Synchrotron radiation

SR is the emission that occurs when relativistic and ultrarelativistic electrons spiral in a magnetic field. Several astronomical objects have been found to emit SR at radio to optical and X-ray

wavelengths. Therefore SR may be responsible for the low-energy component of the observed SED of a GC. Figure 2.6 illustrates an electron of energy $E_\mathrm{e} = \gamma_\mathrm{e} m_\mathrm{e} c^2$ and velocity $\vec{v}$ spiralling in a

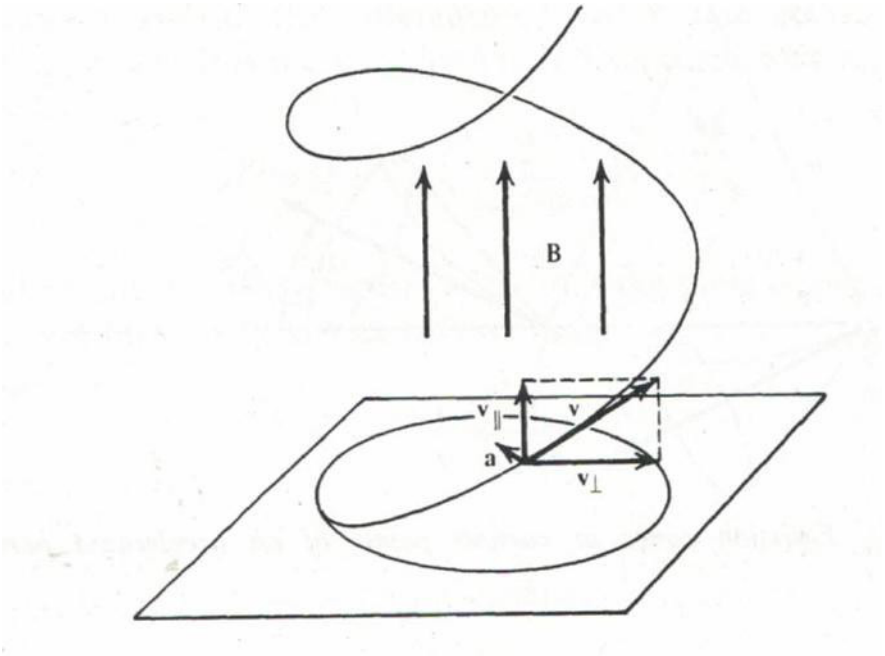

Figure 2.6: An electron spiralling around magnetic field lines emits SR due to the acceleration (change in direction) of the electron (Rybicki & Lightman, 1979).

magnetic field $\vec{B}$. Let the constant angle (i.e., the pitch angle) between its velocity and $\vec{B}$ be ϑ. The electron spirals with angular frequency $\omega_\mathrm{r} = eB/\gamma_\mathrm{e} m_\mathrm{e} c$ independent of ϑ (Blumenthal & Gould, 1970). In the non-relativistic case, a single particle spiralling in a magnetic field will emit power according to the Larmor formula (Blumenthal & Gould, 1970)

$$P_\mathrm{emitted} = -\left(\frac{dE}{dt}\right)_\mathrm{SR} = \frac{2ea^2}{3c^3}, \tag{2.11}$$

where a is the acceleration and e is the charge of the particle ($q = e$ for an electron). Considering the relativistic case and setting $d\vec{v}_{||}/dt = 0$ (since we assume a zero E-field and the B-field cannot change the parallel component of the velocity), the total power of emitted radiation is

$$P_\mathrm{SR} = \frac{2e^4}{3c^5} \gamma_\mathrm{e}^2 \frac{B^2}{m_\mathrm{e}^2} v_\perp^2, \tag{2.12}$$

where $v_\perp$ is the speed of the electron perpendicular to the magnetic field (Rybicki & Lightman, 1979). The SR energy loss rate is thus given by (Blumenthal & Gould, 1970) as

$$\dot{E}_{\rm SR} = -\frac{2r_0^2}{3c}\gamma_{\rm e}^2 B^2 v^2 \sin^2\vartheta. \tag{2.13}$$

The SR power emitted by a single electron of a given pitch angle ϑ may be rewritten as

$$\dot{E}_{\rm SR} = P = 2\sigma_{\rm T} c U_B \gamma^2 \beta^2 \sin^2\vartheta. \tag{2.14}$$

Averaging the term $\sin^2\vartheta$ over the solid angle in the case of an isotropic distribution of pitch angles gives

$$P_{\rm tot} = \dot{E}_{\rm SR} = \frac{4}{3}\sigma_{\rm T} c U_B \gamma_{\rm e}^2 \beta^2, \tag{2.15}$$

which is of the same form as Equation (2.5), where $\sigma_{\rm T}$ is the Thomson scattering cross section and $U_B = B^2/8\pi$ is the magnetic energy density (Blumenthal & Gould, 1970).

The SR spectrum radiated by a single electron is characterised by a critical frequency

$$\omega_{\rm c} = \frac{3}{2}\left(\frac{c}{v}\right)\gamma_{\rm e}^3 w_{\rm r} \sin\vartheta. \tag{2.16}$$

where $\omega_{\rm r} = eB/\gamma_{\rm e} m_e c$ is the gyration frequency of rotation (Longair, 2011). When $v \to c$ we have

$$\omega_{\rm c} = \frac{3}{2}\gamma^3 \omega_{\rm r} \sin\vartheta = \frac{3eB}{2mc}\gamma^2 \sin\vartheta, \tag{2.17}$$

The emitted power per frequency radiated by a single electron is (Rybicki & Lightman, 1979)

$$\left(\frac{dP}{d\omega}\right)_{\rm SR}(\gamma_{\rm e}, \vartheta, \omega) = \frac{\sqrt{3}e^3}{2\pi m_{\rm e} c^2} B \sin\vartheta F(x), \tag{2.18}$$

where $x = \omega/\omega_{\rm c}$ and

$$F(x) = x\int_x^\infty K_{5/3}(\xi)d\xi. \tag{2.19}$$

Here $K_{5/3}$ is the modified Bessel function of the second kind of order 5/3. For small and large

values of x, the function has different asymptotic forms

$$F(x) \propto \begin{cases} x^{1/3} & \text{for} \quad x \ll 1 \\ x^{1/2} e^{-x} & \text{for} \quad x \gg 1 \end{cases}$$

and it has a peak at $x = 0.29$ (Longair, 2011). If the electrons are described by a power-law distribution function, i.e., $N_{\rm e}(\gamma_{\rm e}) \propto \gamma_{\rm e}^{-p}$, the total SR power emitted by particles is

$$\left(\frac{dP}{d\omega}\right)_{\rm tot}(\vartheta, \omega) \propto \omega^{-\alpha'}, \tag{2.20}$$

with the spectral index $\alpha' = (p-1)/2$ (Rybicki & Lightman, 1979). Therefore

$$\frac{dN_\gamma}{dE_\gamma} \propto E_\gamma^{\frac{-(p+1)}{2}} \tag{2.21}$$

and

$$E_\gamma^2 \frac{dN_\gamma}{dE_\gamma} \propto E_\gamma^{\frac{-(p-3)}{2}}. \tag{2.22}$$

2.2.3 Blackbody radiation

A blackbody is defined as a body that fully/perfectly absorbs and radiates energy at all electromagnetic wavelengths. The electromagnetic radiation that a blackbody gives off at a given temperature is called blackbody radiation. The Stefan-Boltzmann law relates the total emitted energy per area per unit time to the absolute temperature, i.e.,

$$R(T) = \sigma T^4, \tag{2.23}$$

where $\sigma = 5.67 \times 10^{-5}\,\mathrm{erg\,cm^{-2}K^{-4}s^{-1}}$ is the Stefan-Boltzmann constant (Rybicki & Lightman, 1979).

The Planck distribution describes the energy density of blackbody radiation, per frequency interval, as

$$u_\nu = \frac{8\pi h\nu^3}{c^3} \frac{1}{e^{h\nu/k_{\rm B}T} - 1}, \tag{2.24}$$

where ν is the frequency, c is the speed of light, and h is Planck's constant (Rybicki & Lightman, 1979). In terms of specific intensity I_ν, the blackbody intensity can be written in the Rayleigh-Jeans

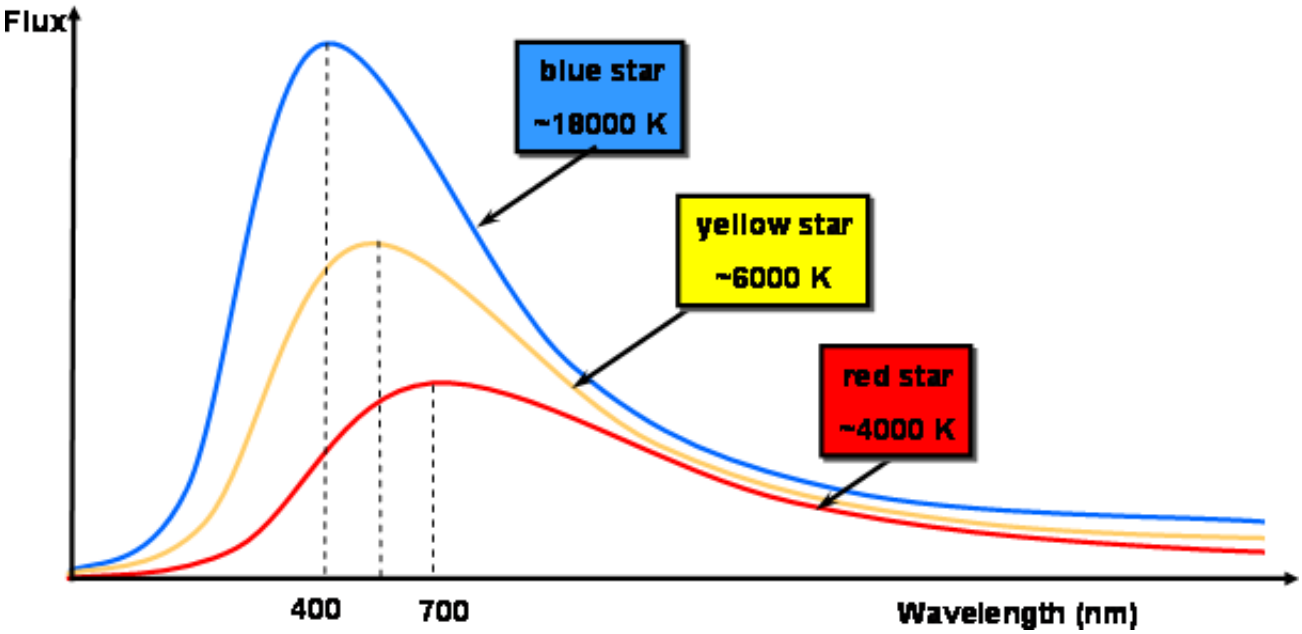

Figure 2.7: Blackbody spectra for three different temperatures, e.g., for $\sim$ 4 000 K (red), $\sim$ 6 000 K (yellow) and $\sim$ 18 000 K (blue) stars. The wavelength and intensity of the peak of each curves moves as the temperature change.

limit in cgs units ($\mathrm{erg^{-1}\,s^{-1}\,cm^{-2}\,Hz^{-1}\,steradian^{-1}}$) as:

$$I_\nu = \frac{2h\nu^3}{c^2}(e^{h\nu/k_\mathrm{B}T} - 1)^{-1} \equiv B_\nu = \frac{c}{4\pi}u_\nu. \tag{2.25}$$

Equation (2.25) can be transformed by using $\lambda = c/\nu$ and $B_\lambda d\lambda = B_\nu d\nu$, thus

$$B_\lambda = B_\nu \mid \frac{d\nu}{d\lambda} \mid = B_\nu \frac{c}{\lambda^2} = \frac{2hc^2}{\lambda^5}\frac{1}{e^{hc/\lambda k_\mathrm{B}T} - 1}. \tag{2.26}$$

To calculate the frequency or wavelength of the peak of a blackbody spectrum, one should take its derivative and equate it to zero, i.e.,

$$\frac{dB_\nu}{d\nu} = 0$$

or

$$\frac{dB_\lambda}{d\lambda} = 0.$$

This leads to Wien's law in two forms: $\lambda_\mathrm{max}T = 0.29$ cm K and $h\nu_\mathrm{max} = 2.8k_\mathrm{B}T$ (Rybicki & Lightman, 1979). Therefore the frequency of the emission (ν_max) is linearly proportional to absolute temperature (T). Figure 2.7 shows the spectra for three different blackbodies. The normalisation of the curve changes as a function of temperature, as does the wavelength at which the peak occurs,

moving to shorter wavelengths for higher temperatures.

2.3 IACT Technique and Observations

In this section, I will discuss how IACTs detect γ-rays. I will also discuss the H.E.S.S. telescope and the future CTA in some detail.

2.3.1 Detection of Gamma Rays with IACTs

Before the experimental detection of γ-rays from cosmic sources, scientists predicted that the Universe was producing these high-energy photons. Scientists believed that a number of different processes such as cosmic-ray interactions with interstellar gas, interactions of energetic electrons with magnetic and photon fields, and supernova explosions occurring in the Universe would result in the emission of γ-rays (Feenberg & Primakoff, 1948). Gamma-ray astronomy could not develop as quickly as other branches of astronomy because there were no detectors above the atmosphere (since γ-rays from space are absorbed by the Earth's atmosphere). High energy γ-ray denotes γ-ray radiation with photon energies 100 kev to tens of Mev, and this energy is detectable by *Fermi*. Very-high-energy γ-rays are detectable by IACTs, and have photon energies of hundreds MeV to 100 TeV. A method for measuring γ-rays from the ground with IACTs was later proposed using the Cherenkov light emitted by a shower particles (Weekes et al., 1989). It was discovered that when γ-rays hit the atmosphere, they produce a shower of relativistic particles that emit a faint blue flash of Cherenkov light. The emission angle of the Cherenkov light is about 1°, producing a light cone with a radius of roughly 100 m on the ground for a γ-ray that interact with the atmosphere at an altitude of about 10 km.

If telescopes are built with large mirrors, multiple light detectors, and fast sensitive cameras, they should be able to detect the Cherenkov light to indirectly 'see' the shower image generated by the incident high-energy γ-ray. To get a γ-ray sky image, a computer programme combines (currently) up to four or five (in case of H.E.S.S.) images of the air shower to find its direction, and also to know how much energy is deposited in the atmosphere. The arrival time of the γ-ray is also recorded. The original direction of the γ-ray is plotted as a point on a map of the sky. The combination of many such points in the sky provides an image of the γ-ray source, and one can determine the

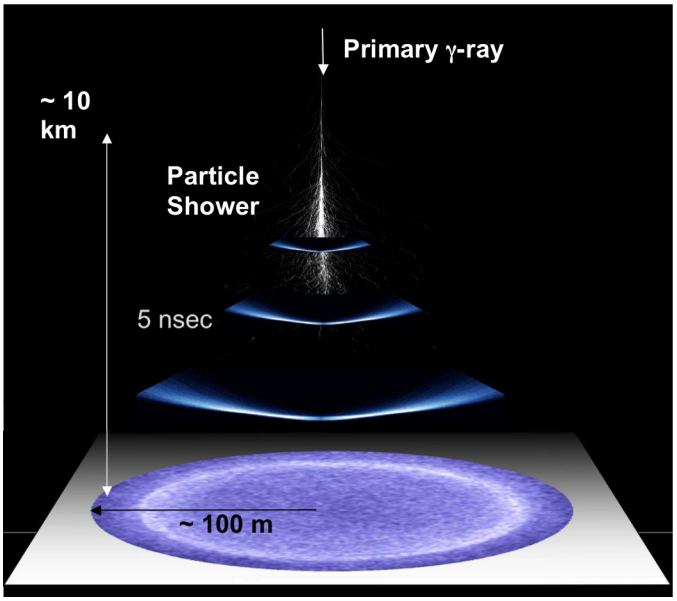

Figure 2.8: Detection of an air shower with an IACT (https://za.pinterest.com/pin/475974254340894468/).

morphology of a source, its temporal variability, and the variability of the energy spectrum of the γ-rays (see Section 3.3.3 for more details). Nowadays, γ-rays are detected using telescopes such as H.E.S.S. (Aharonian et al., 2006a), MAGIC (Teshima, 2008), and VERITAS (Swordy, 2008).

2.3.2 The H.E.S.S. Experiment

H.E.S.S. consists of five IACTs, four 13-m telescopes (H.E.S.S. I), arranged 120 m apart from each other on the vertices of a square, and one large 28-m telescope (H.E.S.S. II) constructed at the centre of the array. The telescopes are located at a height of about 1 800 m above sea level on farm Goellschau in the Khomas region of Namibia. Up there, they can observe γ-rays from the most violent phenomena in the Universe, from exploding stars to supermassive black holes.

The H.E.S.S. I telescopes have been in operation since 2003. H.E.S.S. II saw its first light on 26 July 2012 (Giebels, 2013) and with a gross weight of about 580 tonnes including a 3 tonne camera, this is the largest mirror surface created by mankind at this time. H.E.S.S. II was built to lower the energy threshold and to improve the sensitivity of the full system. The telescopes suffer from the harsh environmental conditions and ageing, and thus a major hardware upgrade was performed for H.E.S.S. I over a timespan of 2 years to allow continuous for stable operations of the array.

Figure 2.9: The H.E.S.S. site at the Goellschau farm. The five telescopes are visible: the four small telescopes H.E.S.S. I and the large telescope H.E.S.S. II at the centre (https://en.wikipedia.org/wiki/File:HESS_II_gamma_ray_experiment_five_telescope_array.jpg).

2.3.3 The Future CTA

The next VHE γ-ray observatory, CTA, will have a factor of 10 better sensitivity and improved angular resolution compared to the existing ground-based γ-ray telescopes. This telescope array will have an energy range from 30 GeV − 100 TeV (Vercellone, 2014). The array will consist of different types of telescopes to cover this wide energy range in a cost-efficient way. The telescopes that will observe at relatively low energies will have 23-m diameter mirrors with a 4.4° field of view (FoV). The medium-energy telescopes ($\sim 100\,\mathrm{GeV} - 10\,\mathrm{GeV}$) will consist of 12-m diameter mirrors with an FoV of at least 7°. The telescopes to observe at high energies (>10 TeV) will have 4-m diameter telescopes with an 8° FoV (Carr, 2016). To achieve full sky coverage, this array will have sites in both the northern and southern hemispheres. The decision was made that the Instituto de Astrofisica de Canarias (IAC), Roque de los Muchachos Observatory in La Palma, Spain (northern) and the European Southern Observatory (ESO) Paranal grounds in Chile (southern) will host CTA[2]. Construction is expected to begin in 2017.

2.4 Summary

In this chapter, I discussed the stellar populations in GCs and the estimation of their distances and ages. I also discussed MSPs found in GCs and the radiation mechanisms that take place in GCs. I then discussed IACTs including H.E.S.S. and the future γ-ray instrument, the CTA. We

[2] http://iopscience.iop.org/article/10.1088/2058-7058/28/9/18/pdf

know a lot about GCs in general but we do not know much about the VHE γ-ray radiation from GCs because we have only seen one GC with H.E.S.S. Next, I will discuss observations of GCs by H.E.S.S.

Chapter 3

H.E.S.S. Observations and Data Analysis

In the previous chapter I have discussed GCs in general, the radiation processes that take place in GCs, MSPs, the H.E.S.S. telescope, and CTA. In this chapter, I will discuss observations of GCs by H.E.S.S. and introduce the reader to the H.E.S.S. Analysis Package (HAP). Previously, the H.E.S.S. Collaboration analysed data for pointings in the direction of 15 GCs (without any detection), in addition to detecting the GC Terzan 5. I decided to reanalyse data for these selected sources, as well as for Terzan 5 and four other sources detected by *Fermi*. This was done because H.E.S.S. has accumulated more data since the previous analysis and I wanted to investigate whether I could find deeper flux upper limits that would be more constraining to the Kopp et al. (2013) model. I will also be using a different analysis chain, i.e., HAP (Aharonian et al., 2006a) whilst other researchers used Model++ (de Naurois & Rolland, 2009), which is more sensitive at lower energies than HAP. In Section 3.1 I will present the observational selection criteria of the sources previously used by Abramowski et al. (2013). Next, I will discuss some details of their analysis (Section 3.2). I will then give a step-by-step description of our data analysis with HAP (Section 3.3), and present the results including the energy thresholds, differential and integral fluxes or flux upper limits for each of the 16 GCs and also for the sources detected by *Fermi* (Section 3.4). Finally, I will compare our results with previous results obtained by Abramowski et al. (2013) in Section 3.5 and present a summary in Section 3.6.

3.1 Source Selection

Following the plausible discovery of Terzan 5 in the very-high-energy (VHE) band (Abramowski et al., 2011) it was realised that GCs could constitute a new class of such sources. This motivated the H.E.S.S. Collaboration to search for more VHE GCs in their archival data. Fortunately, many GC positions were covered by the H.E.S.S. Galactic Plane Survey (Aharonian et al., 2006b; Gast et al., 2011) or lay in the same FoV of other observed H.E.S.S. sources. Abramowski et al. (2013) therefore used the GC catalogue of Harris (2010) to select 15 GCs within 1.0° of the Galactic Plane. The data furthermore should have passed the standard quality selection criteria and the pointing position should have been $\leq 2.0°$ offset from the position of the GC. They also made sure that the GC had at least 20 runs passing the standard quality selection criteria (a run is about 28 minutes of observation). I added Terzan 5 to the list of candidates as it is the only GC that H.E.S.S. has firmly detected to date.

GC name	Date range	R.A. (J2000)	Dec. (J2000)	(l, b)	D_{Sun} (kpc)
NGC 104	Oct. 2005 – Aug. 2010	$00^h24^m05^s.67$	$-72°04'52''.6$	$305.89°, -44.89°$	4.5
NGC 6388	Jul. 2008 – Apr. 2013	$17^h36^m17^s.23$	$-44°4'07''.8$	$345.56°, -6.74°$	9.9
NGC 7078	May 2007 – Aug. 2007	$21^h29^m58^s.33$	$+12°10'01''.2$	$65.01°, -27.31°$	10.4
Terzan 6	Apr. 2004 – Aug. 2012	$17^h50^m46^s.38$	$-31°16'31''.4$	$358.57°, -2.16°$	6.8
Terzan 10	May 2004 – May 2005	$18^h03^m36^s.4$	$-26°04'21''$	$4.49°, -1.99°$	5.8
NGC 6715	Jun. 2006 – Jul. 2012	$18^h55^m03^s.33$	$-30°8'47''.5$	$5.61°, -14.09°$	26.5
NGC 362	Oct. 2008 – Sep. 2012	$01^h03^m14^s.26$	$-70°50'55''.6$	$301.53°, -46.25°$	8.6
Pal 6	May 2004 – Sep. 2010	$17^h43^m42^s.2$	$-26°13'21''$	$2.10°, 1.78°$	5.8
NGC 6256	May 2006 – Apr. 2008	$16^h59^m32^s.62$	$-37°07'17''.0$	$347.79°, 3.31°$	10.3
Djorg 2	Jun. 2004 – Sep. 2012	$18^h01^m49^s.1$	$-2°49'33''$	$2.77°, -2.50°$	6.3
NGC 6749	Jun. 2005 – May 2013	$19^h05^m15^s.3$	$+01°54'03''$	$36.20°, -2.21°$	7.9
NGC 6144	May 2006	$16^h27^m13^s.86$	$-26°01'24''.6$	$351.93°, 15.70°$	8.9
NGC 288	Sep. 2005 – Dec. 2005	$00^h52^m45^s.24$	$-26°34'57''.4$	$152.30°, -89.38°$	8.9
HP 1	Jun. 2004 – May 2005	$17^h31^m05^s.2$	$-29°58'54''$	$357.44°, 2.12°$	8.2
Terzan 9	May 2004 – May 2005	$18^h01^m38^s.8$	$-26°50'23''$	$3.61°, -1.99°$	7.1
Terzan 5	May 2004 – Sep. 2010	$17^h48^m04^s.80$	$-24°46'45''$	$3.84°, 1.69°$	5.9

Table 3.1: In this table I list the names of the observed GCs with their observational period (date range); right ascension (epoch J2000); declination (epoch J2000); Galactic longitude and latitude in degrees, and the distance from the Sun in kiloparsecs.

Table 3.1 contains information about the observational period (date range), i.e., the periods for which observations of specific sources were done. The table also indicates the position of each source in the equatorial coordinate system (right ascension and declination, which are the celestial equivalents of terrestrial longitude and latitude, respectively), Galactic coordinate system, and the

distance from the Sun to the source (Harris, 2010).

3.2 Previous H.E.S.S. Data Analyses

Terzan 5 is the only GC that has probably been detected in the VHE band. It is located at a distance of 5.9 kpc from Earth (Ferraro et al., 2009) at RA(J2000) $17^h48^m04^s.85$ and Dec $-24°46'44''.6$ (Galactic coordinates: $l = 3.84°$, $b = 1.69°$) and exhibits a core radius of $r_c = 0.15'$, a half-mass radius of $r_h = 0.52'$, and a tidal radius of $r_t = 4.6'$ (Lanzoni et al., 2010). Data on Terzan 5 were obtained by H.E.S.S. from 2004 to 2010 for 90 hours of 3- and 4-telescope data with an average zenith angle of 20.4° and a mean pointing direction offset of 0.95°. Abramowski et al. (2011) applied hard cuts (Section 3.3) and found that a point-like source of VHE γ-rays was detected (see Figure 3.1). Abramowski et al. (2011) noted that the significance (the confidence level at which H.E.S.S. has detected the source) of Terzan 5 reached 5.3σ. For a power-law spectral model (see Equation 3.3), the flux normalisation K at 1 TeV was $(5.2 \pm 1.1) \times 10^{-13}$ cm^{-2}s^{-1}TeV^{-1} and the spectral index was $2.5 \pm 0.3_{stat} \pm 0.2_{sys}$, which corresponded to an integral photon flux within the integration region of $(1.2 \pm 0.3) \times 10^{-12}$ cm^{-2}s^{-1}, or 1.5% of the Crab flux, in the 0.44−24 TeV range (Aharonian et al., 2006a).

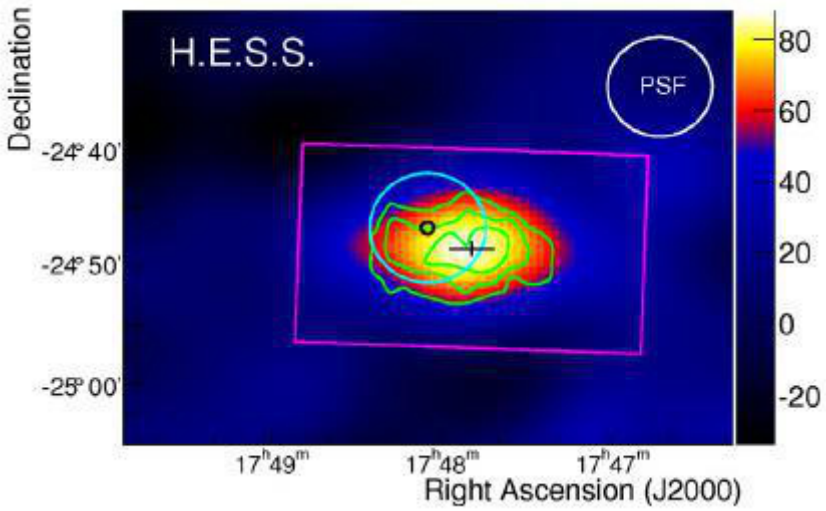

Figure 3.1: This figure illustrates the exposure-corrected excess image from H.E.S.S. data, produced using the template background estimation method (Rowell, 2003). The image was smoothed with a Gaussian function of 0.1° width and overlaid with $(4\sigma - 6\sigma)$ significance contours in RA-Dec J2000 coordinates. The rectangle shows the integration region used for the full source spectrum. The circle on the upper right corner shows the PSF of the instrument. The black circle shows the half-mass radius, and the cyan circle illustrates the larger tidal radius of the GC. The cross indicates the best-fit source position of HESS J1747-248. From Abramowski et al. (2011).

For the 15 GCs other (see Section 3.1), Abramowski et al. (2013) applied standard quality selection cuts on the observational runs to exclude data affected by bad weather conditions and poor performance of the instrument. They used the Model++ analysis chain (de Naurois & Rolland, 2009) that gave an improved sensitivity, especially at lower energies and better efficiency for γ-hadron separation. Abramowski et al. (2013) also used 'standard cuts' (Aharonian et al., 2006a) for the analysis which included a 60 photo electron (p.e.) cut on the image intensity. The analysis had an average point spread function (PSF) or 68% containment radius of 0.07°. The PSF represents the accuracy of the reconstructed arrival directions of the γ-ray events from a point source. In the case of H.E.S.S., the PSF is a function of the θ^2 values of the events, where θ^2 is defined as the square of the angular distance between the *true* event direction and the *reconstructed* event direction, θ is defined in Figure 3.3. The mathematical parametrisation of the H.E.S.S. PSF is given by the sum of two 1D Gaussian

$$PSF = A\Big(\exp\Big(\frac{-\theta^2}{2\sigma_1^2}\Big) + \mathrm{A_{rel}}\exp\Big(\frac{-\theta^2}{2\sigma_2^2}\Big)\Big) \tag{3.1}$$

as given in Aharonian et al. (2006a), where σ_1 and σ_2 are standard deviation parameters, A is the absolute amplitude, and $\mathrm{A_{rel}}$ is the relative amplitude of the second Gaussian. The PSF can therefore be seen as a measure of apparent extension of a point-like source.

Abramowski et al. (2013) used the reflected-background technique (see Figure 3.2; Aharonian et al. (2006a)) so that the regions used for ON (signal, i.e., the number of γ-ray events from the direction of the source) and OFF (background, i.e., the number of the γ-ray events from the background) extraction have the same acceptance in the FoV of the camera. The reflected-background method uses a number of background regions that are at equal distances from the observational position and are at the same distance at the ON positon. The combined events from these positions are used to estimate the background at the *ON* position, scaled by the relative area of the *ON* and *OFF* regions. Alternatively, the ring-background method determines the background for each position in the FoV by using the background rate contained in a ring around that position.

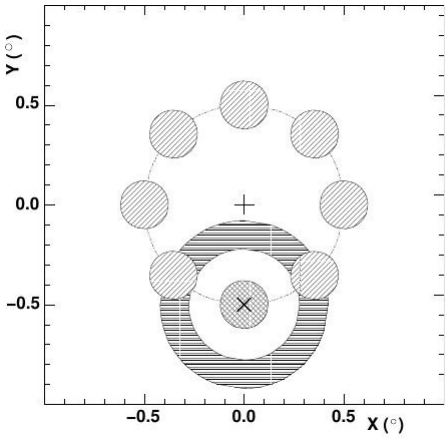

Figure 3.2: This figure illustrates the reflected and ring-background regions. The + in the figure illustrates the pointing direction of the telescope, whilst the X shows the target position. The *ON* region surrounding the target position is marked by a cross-hatched circle. The ring-background region (annulus) is marked with horizontal lines, while the reflected-background regions (circles) are filled by diagonal lines (Aharonian et al., 2006a).

Abramowski et al. (2013) calculated the ratio of the ON-source area to the OFF-source area α (Li & Ma, 1983), i.e.,

$$\alpha = \frac{\mathrm{A_{ON}}}{\mathrm{A_{OFF}}}. \tag{3.2}$$

Table 3.2 indicates the results of the analysis obtained by Abramowski et al. (2013) for each individual GC. I added a column to Table 3.4 for differential fluxes to compare our more recent results with those of Abramowski et al. (2013). In order to compute the flux I have assumed a power-law photon spectrum of the form (Paredes et al., 2008):

$$\frac{dN}{dE} = K\Big(\frac{E}{1\ \mathrm{TeV}}\Big)^{-\Gamma}. \tag{3.3}$$

where K is the normalisation constant and $\Gamma = -2.5$ is the spectral index chosen to allow comparison with the result of Terzan 5

GC name	$E_{\rm th}$ (TeV)	$N_{\rm ON}$ (counts)	$N_{\rm OFF}$ (counts)	$\frac{1}{\alpha}$	Sig (σ)	$F_{\rm UL}(E > E_{\rm th})$ ($\times 10^{-12}$) (ph cm^{-2}s^{-1})	Diff $F_{\rm UL}$ at 1 TeV ($\times 10^{-12}$) (cm^{-2}s^{-1}TeV^{-1})	Livetime (h)
(i) Standard cuts								
NGC 104	0.72	72	941	18.2	2.6	1.9	1.74	23.1
NGC 6388	0.28	180	2365	14.9	1.6	1.5	0.33	17.9
NGC 7078	0.40	119	1988	15.0	-1.2	0.72	0.27	12.3
Terzan 6	0.28	202	8194	42.0	0.5	2.1	0.47	15.2
Terzan 10	0.23	76	2455	36.0	0.9	2.9	0.48	4.2
NGC 6715	0.19	159	2361	15.2	0.3	0.93	0.12	11.8
NGC 362	0.59	18	533	33.0	0.4	2.4	1.63	5.0
Pal 6	0.23	363	10810	31.4	1.0	1.2	0.20	24.7
NGC 6256	0.23	64	1869	27.4	-0.5	3.2	0.53	5.3
Djorg 2	0.28	56	2387	39.4	-0.6	0.84	0.19	4.6
NGC 6749	0.19	84	2633	29.3	-0.6	1.4	0.17	8.2
NGC 6144	0.23	63	2196	30.8	-1.0	1.4	0.23	4.7
NGC 288	0.16	647	24148	38.5	0.8	0.53	0.05	46.7
HP 1	0.23	67	2771	34.3	-1.6	1.5	2.48	5.6
Terzan 9	0.33	89	2556	31.7	0.9	4.5	1.28	5.2
Stacking analysis								
-	0.23	2242	67826	31.2	1.6	0.33	-	195

Table 3.2: The colums in the table are the GC names, energy threshold of the analysis, defined as the location of the peak in the distribution of reconstructed photon energies; total number of ON and OFF counts; ratio between OFF and ON exposures when applying the reflected-background technique; detection significance following Li & Ma (1983); the integral and differential flux upper limits (99% confidence level or c.l. following Feldman & Cousins 1998) assuming a power law with an index of 2.5 (Abramowski et al., 2013); and livetime[1].

Abramowski et al. (2013) noted that no significant excess emission was seen above the estimated background for any of the 15 selected GCs. The significances for detection for each GC were well below the threshold of 5σ. They derived the photon flux upper limits above the energy threshold (99% c.l.) following Feldman & Cousins (1998) assuming a power-law spectrum for the photon flux, choosing $\Gamma = 2.5$ to compare with the results obtained for Terzan 5.

Abramowski et al. (2013) also performed a stacking analysis to search for a population of faint emitters. In this case, the total number of ON and OFF counts was the sum over all ON and OFF counts of the runs in the stack.

The total GC stack had an acceptance-corrected livetime of 195 hours of good quality data and an energy threshold of 0.23 TeV. Since Abramowski et al. (2013) were searching for VHE γ-rays from each GC, they performed two different kinds of analyses: assuming both point-like and extended

[1]A source is observed for some time, but some of the time in that observation time is "dead time", for example when the electronics is not triggering during transitions. The "dead time" is subtracted from the observation time to get the livetime.

sources. They noted that the total detection significances obtained with the stacking analyses were also below the threshold of 5σ which is required for a detection. Abramowski et al. (2013) therefore calculated upper limits on the photon flux for the full stack, assuming a power-law spectrum with an index of $\Gamma = 2.5$.

3.3 The H.E.S.S. Analysis Package

HAP is one of the supported analysis and reconstruction frameworks for H.E.S.S. data. HAP has been released in two flavours called HAP-HD and HAP-France. Different datasets are selected depending on the HAP flavours and the γ-hadron separation techniques. These could be standard cuts, loose cuts, and hard cuts that are used for reducing the cosmic-ray-dominated background remaining after the hardware trigger (Aharonian et al., 2006a).

H.E.S.S. uses the following separation techniques:

- Standard cuts are mostly used for sources with a flux at the level of ∼10% of the integral flux of the Crab Nebula and with a spectrum similar to that of the Crab Nebula, i.e., Γ ∼2.0. These cuts are based on Toolkit Multivariate Data Analysis (TMVA) analysis and include a 60-photo-electron cut on image intensity.
- Hard cuts are often used for weak sources exhibiting a ∼1% flux of the Crab Nebula with a hard spectrum Γ ∼2.0. They are also based on TMVA analysis and include a 160-photo-electron cut on image intensity. The hard cuts increase the energy threshold because of the stricter cut on the image amplitude.
- Loose cuts are optimised for strong sources with an integral flux similar to that of the Crab Nebula and a steeper spectrum of Γ ∼3.0. Loose cuts are also based on TMVA analysis and allow a 40-photo-electron cut on image intensity. These cuts require a low energy threshold and are the loosest in the sense of rejecting the smallest number of events.

3.3.1 HAP Installation

HAP is built on top of ROOT, which is an object-oriented data analysis package that is written in C++, on a Linux operating system and makes use of object-oriented design for the implemen-

tation of data storage and data processing. A suitable ROOT release must be installed before the installation of HAP. The Concurrent Versions System (CVS) tool (a version control system for collaborative software development) is used for maintaining the HAP source code.

The following command provides the SCons module which is needed for compiling the code:

```
cvs checkout -r hap-13-06 scons SConstruct thishess.sh
```

HAP uses the SCons Build System for compiling and linking. First the important environmental parameters are set with:

```
source ./thishess.sh
```

This sets important environment variables, e.g., `$HESSROOT`, which is the path where the software is installed.

Second the building process is initiated with:

```
scons --checkout-missing=hap-13-06 HAP
```

During building, SCons ensures that H.E.S.S. software modules needed for the build are retrieved from the CVS automatically during the building process. After building HAP, it should be tested to ensure that it was built properly. The following command will give the HAP version number and a list of command line arguments to configure the analysis:

```
$HESSROOT/hddst/bin/hap
```

A set of predefined analysis cuts must be chosen using cut configuration files to perform a proper analysis. There are different versions of cut configurations available and the older ones are needed if data are to be analysed using an old HAP version. Therefore, each version of the configuration is stored in a separate directory. The proper cut configuration is chosen depending on the type of source analysis.

The H.E.S.S. software is written in such a way that the image cleaning and image parametrisation are done automatically.

3.3.2 Image cleaning

Image cleaning is done so that only the pixels containing the Cherenkov light in an image are selected. This is performed by a *tail* procedure to cut away other pixels containing mainly night

sky background (NSB) and keeping only the pixels with more than 10 p.e. and, at the same time, neighbouring pixels of more than 5 p.e.

3.3.3 Image parametrisation

The cleaned shower image is parameterised using the Hillas method, i.e., after images of an air shower have been recorded they are processed to measure the *Hillas parameters* (Aharonian et al., 2006a). The Hillas parameters consist mostly of geometric parameters of the *ellipses* that each telescope records in the camera plane. These include the width, length, distance from camera centre, and the orientation of each ellipse. This method is called the *reconstruction of the γ-ray shower* (see Figure 3.3).

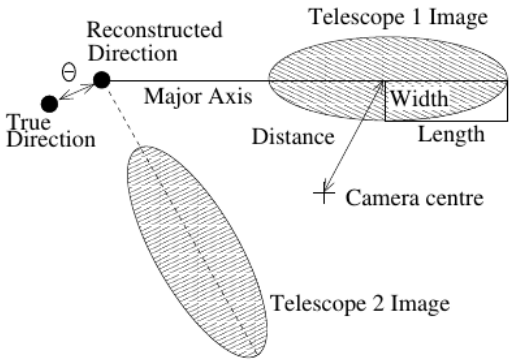

Figure 3.3: The Hillas parameters for determining the direction of the incident γ-ray (Aharonian et al., 2006a).

Figure 3.4 shows an image recorded in a typical camera of the H.E.S.S. Cherenkov Telescopes. The Hillas parameters are extracted from these images for further analysis.

As a first approximation, the shape of the shower image is assumed to be elliptical and characterised by the following parameters:

- **Width and length** - the lengths of the minor and major axes of the ellipse, respectively.
- **Centre of gravity of the light distribution** - the position of the Hillas ellipse in the camera.
- **Orientation** - the angle between the major axis of the ellipse and the x-axis of the camera.
- **Size** or **image amplitude** - the total collected light intensity in the image.

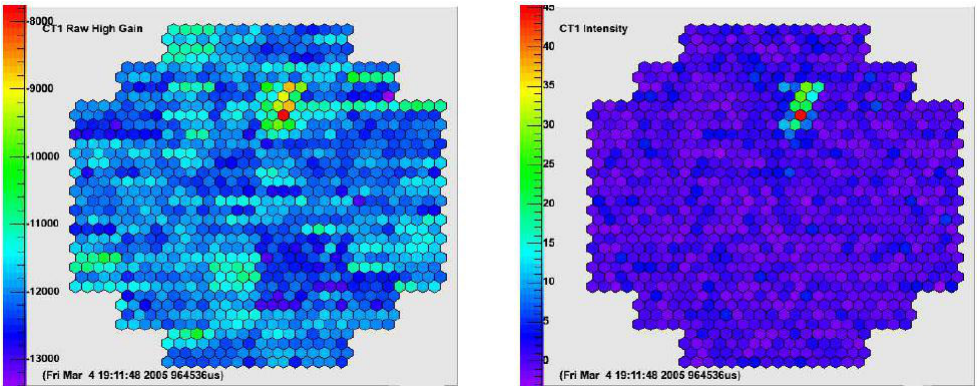

Figure 3.4: A typical image recorded in a Cherenkov Telescope camera of H.E.S.S. These images are used to deduce the corresonding Hillas parameters of the recorded γ-ray event. The Figure on the left shows the raw data (what the photo-tube-multipler sees before image cleaning is done). The Figure on the right shows the image after cleaning (Sebastian, 2005).

3.3.4 Shower Reconstruction

The direction of the shower and the `impact parameter` are derived geometrically. The impact paremeter is the distance of the core location of the main shower from a telescope. The impact parameter and the image of the source have to lie on the symmetric axis of the image. The images are then superimposed and their axes are intersected to derive the shower direction (see Figure 3.5(a)). The impact point (core location) is obtained by intersecting the image axes coming from the location of the telescope (see Figure 3.5(b)). The energy and the `scaled shape parameters` are reconstructed by using the impact parameter along with the image amplitude. For each observation run, the reconstructed data are stored as a dataset, called DST.

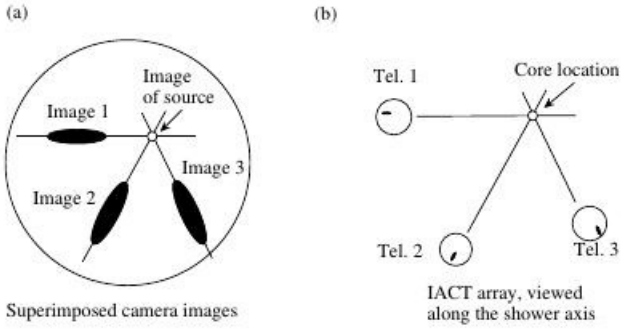

Figure 3.5: (a) Reconstruction of the shower direction and of (b) the impact point from the images observed in the cameras (Daum et al., 1997).

3.3.5 Run Selection

One should next execute a command that searches for the run list of the required source. The name or the position of the source should be specified within the command. For example:

```
/home/hfm/hess/hap-13-06/summary/scripts/findruns.pl --name "Terzan 5" 2
--selection detection
```

```
/home/hfm/hess/hap-13-06/summary/scripts/findruns.pl --name "Terzan 5" 2
--selection spectral
```

or

```
/home/hfm/hess/hap-13-06/summary/scripts/findruns.pl 267.020833 -24.780000 2
--galactic --selection detection
```

```
/home/hfm/hess/hap-13-06/summary/scripts/findruns.pl 267.020833 -24.780000 2
--galactic --selection spectrum
```

The first two commands search the database for observational runs of the source "Terzan 5", taken no more than 2 degrees away from the position of this cluster. These commands only select runs which have been flagged as suited for either detection or spectral analysis by the data quality selection criteria. The last two commands search for the observational runs by using the position (Galactic coordinates l, b) of the source and select only runs which have been flagged as suited for either detection or spectral analysis by the data quality selection criteria.

3.3.6 Gamma-Hadron Separation and Background Subtraction

In order to specify within HAP which region to analyse, which background technique to use, and what analysis products to produce, one can create a configuration file. An example of the HAP *configuration file* for Terzan 5 data analysis is as follow:

```
[OPTIONS]
    verbose = true
    config = std_zeta

    runlist = Terzan5_0_2_detection.lis
    outdir = /d1/hfm/pkrueger/Terzan5/terzan5_std_zeta
    outfile = Terzan5det

[Background]
    Method = RingBg
    TestPosRA = 267.02083
    TestPosDec = -24.78

#     ThetaSqr = 0.16
#[RingBgMaker]
#     InnerRingRadius = 0.5
#     RingThickness = 0.5
```

The configuration file contains information about the general analysis (ring-background technique). It also contains source-specific information, e.g., the run list (e.g.,`Terzan5_0_2_detection.lis`), and the choice of the cut configuration (standard in this example). One can then run the command below:

```
$HESSROOT/hddst/scripts/hap_split.pl --include Terzan5_detect.conf
```

The above command creates a directory called `Terzan5.hap` which contains the following subdirectories:

- **ROOT data** - the data and plotted output are sent to a file called `Terzan5_0_2_std.root`

- **Log file** - `Terzan5_0_2_std.log.conf` contains all of the configuration options used in the analysis (including default values). Each time the analysis is run, the new configuration is appended to this file.

- **Maker Chain** (the software pipeline) - one can view a plot of the MakerChain used to process the data.

3.3.7 Post Processing: Sky Maps and Spectral Graphs

The following command can now be run:

```
$HESSROOT/hdscan/bin/QuickPlot Detect_merged.root maps 0.1.
```

The QuickPlot command uses the analysis result *Detect_merged.root* with a correlation radius (related to the PSF) of 0.1° and displays the results, whereby most of the results are given as sky maps, which are put in the maps directory. A sky map is a diagrammatic representation of the night sky.

To obtain the spectrum of the cluster, one can run the command

```
$HESSROOT/hddst/scripts/hap_split.pl --include Terzan5spec.conf
```

where the `Terzan5spec.conf` contains the same information as in `Terzan5det.conf` except for the runlist name. One can then create a `Fitspec.conf` file which contains the following information

```
[OPTIONS]
   InputFile = "Terzan5spec_merged.root"
   OutputFile = "Terzan5spec"
   FitModels = PowerLaw ExpCutoffPL
   Emin = -1
   Emax = -1
   FitOption = QRP
   FitAlgo = ForwardFolded
#   RebinAlgo = NONE
   RebinAlgo = MinSignif
   RebinParameter = 2.
   Min-Livetime-Fraction = 1.
   DoNotPlotSpectrum = false
   PlotOption = RLC
   DoNotPlotDiagnostics = false
   Extension = ".png"
   NumberOfSimulations = 100
   BatchMode = true
```

The parameters have the following meaning:

- **FitModels** - A power law and a power law with an exponential cut-off is fitted.
- **Emax** - Maximum energy (TeV) over which to fit. (The -1 indicates that the maximum photon energy should be derived directly from the data.)
- **Emin** - Minimum energy (TeV) over which to fit. (The -1 indicates that the minimum photon energy should be derived directly from the data.
- **FitOption** - Option used when fitting the spectrum.
- **FitAlgo** - Algorithm used to fit the spectrum.
- **RebinAlgo** - Algorithm used to rebin the spectrum.

- **RebinParameter** - Parameter used to control the rebinning algorithm.
- **Min-Livetime-Fraction** - Minimum fraction of livetime used to determine energy range.
- **DoNotPlotSpectrum** - Optionally plot the spectrum.
- **PlotOption** - Control the flux plot.
- **DoNotPlotDiagnostics** - Optionally plot the statistics and diagnostics of the spectrum.
- **Extension** - Extension used for saving plots. If none is given then the plots are not saved.
- **NumberOfSimulations** - Number of times to simulate and fit the spectrum.
- **BatchMode** - Disable ROOT interactive mode.

Lastly,the following command can be run:

```
$HESSROOT/hddst/bin/FitSpectrum --include Terzan5Fitspec.conf
```

FitSpectrum fits the spectrum contained in a HAP output file and stores the result in ROOT format; it then produces a power-law spectrum.

3.4 Results

As mentioned in Section 3.1, the selection of the GCs was done by applying *a priori* cuts on the target and observational run list as stated in Abramowski et al. (2013). I applied the standard cuts TMVA to do the γ-hadron separation and then applied loose and hard selection TMVA cuts. I present the results for the analyses of each GC in Table 3.3. The ON and OFF counts, $1/\alpha$, and significance of the sources are recorded in Table 3.3. The significances for all GCs are below the threshold of 5σ, except for Terzan 5.

GC Name	Livetime (h)	N_{ON}	N_{OFF}	$\frac{1}{\alpha}$	Significance (σ)
(*i*) Standard cuts					
NGC 104	33.7	773	12 787	17.8	2.0
NGC 6388	51.1	886	14 964	17.7	1.4
NGC 7078	16.6	383	7 005	17.8	-0.5
Terzan 6	59.6	659	11 581	17.3	-0.4
Terzan 10	10.8	176	3 224	18.0	-0.2
NGC 6715	113.8	2587	45 367	17.7	0.5
NGC 362	25.5	330	6 220	17.9	-0.9
Pal 6	58.2	790	14 134	17.6	-0.4
NGC 6256	9.8	185	3 221	18.0	0.5
Djorg 2	14.1	155	2 935	18.6	-0.2
NGC 6749	17.7	287	5 141	17.9	0.03
NGC 6144	8.6	159	3 117	16.9	-1.9
NGC 288	110.7	1217	21 186	17.3	-0.3
HP 1	13.7	160	2 851	17.4	-0.3
Terzan 9	13.9	211	4 051	17.7	-1.1
Terzan 5	86.5	1727	26 383	17.8	6.0
(*ii*) Hard cuts					
NGC 104	33.7	148	2 994	22.5	1.2
NGC 6388	51.1	168	3 393	22.5	1.3
NGC 7078	16.6	75	1 576	23.0	0.8
Terzan 6	59.6	140	2 865	20.7	0.1
Terzan 10	10.8	20	682	22.6	-1.9
NGC 6715	113.8	349	8 097	22.4	-0.6
NGC 362	25.5	63	1 431	23.3	0.2
Pal 6	58.2	143	3 058	22.6	0.6
NGC 6256	9.8	34	668	22.8	0.8
Djorg 2	14.1	27	646	22.9	-0.2
NGC 6749	17.7	44	1 246	23.0	-1.4
NGC 6144	8.6	35	751	21.1	-0.09

GC Name	Livetime (h)	$N_{\rm ON}$	$N_{\rm OFF}$	$\frac{1}{\alpha}$	Significance (σ)
NGC 288	110.3	209	4 342	22.6	1.2
HP 1	13.7	25	627	22.2	-0.6
Terzan 9	13.9	28	867	22.8	-1.7
Terzan 5	86.5	372	5 597	22.3	7.1
(*iii*) Loose cuts					
NGC 104	33.7	1 774	19 191	11.2	1.3
NGC 6388	51.1	3 390	37 972	11.3	0.3
NGC 7078	16.6	1 082	11 888	11.2	0.7
Terzan 6	59.6	2 056	23 252	11.1	-0.7
Terzan 10	10.8	620	7 167	11.2	-0.8
NGC 6715	113.8	9 033	100 890	11.2	0.2
NGC 362	25.5	788	9 122	11.1	-1.1
Pal 6	58.2	2 793	30 830	10.9	-0.7
NGC 6256	9.8	628	7 314	11.3	-0.8
Djorg 2	14.1	613	6 801	11.7	1.3
NGC 6749	17.7	925	10 179	11.1	0.3
NGC 6144	8.6	544	6 531	10.7	-2.6
NGC 288	110.3	4 765	51 798	10.6	-1.4
HP 1	13.7	630	6 504	10.8	0.98
Terzan 9	13.9	809	9 257	11.0	-1.2
Terzan 5	86.5	5 722	58 884	11.2	6.0
Stacking analysis					
(*i*) Standard	-	8 958	157 784	17.6	0.1
(*ii*) Hard	-	1 508	33 243	22.4	0.6
(*iii*) Loose	-	30 450	338 696	11.1	-0.9

Table 3.3: In this table, I list the analysis details. The colums are GC names, livetime of H.E.S.S. observational runs passing standard, hard, and loose quality selection cuts; total number of ON and OFF counts; ratio of ON and OFF exposures when applying a reflected-background technique, and the detection significance (confidence level).

I obtained α from the analysis after running a command for producing sky maps.The significance

level for each GC was obtained from (Li & Ma, 1983)

$$S = \sqrt{2}\Big\{N_{\rm on}\ln\Big[\frac{1+\alpha}{\alpha}\Big(\frac{N_{\rm on}}{N_{\rm on}+N_{\rm off}}\Big)\Big] + N_{\rm off}\ln\Big[(1+\alpha)\Big(\frac{N_{\rm off}}{N_{\rm on}+N_{\rm off}}\Big)\Big]\Big\}^{\frac{1}{2}}. \quad (3.4)$$

I also performed a stacking analysis for all sources to increase the sensitivity. The stacking analysis was done as follows: I obtained the total number of ON and OFF counts as the sum over all ON and OFF counts of the runs in the stack respectively, and used $1/\alpha$ as the ratio between these sums.

The total detection significance obtained with the stacking analysis was 0.1σ for standard cuts, 0.6σ for hard cuts, and -0.9σ for loose cuts, which are well below the threshold of 5σ required for a firm detection by H.E.S.S. (see Table 3.3).

Table 3.4 shows the results for the energy threshold (the location of the peak in the distribution of reconstructed photon energies) of the analysis for each source, the differential flux upper limits at 1 TeV, the integral photon flux upper limits, and minimum and maximum energy. The flux upper limits were obtained at 99% c.l. using the Feldman & Cousin's method (Feldman & Cousins, 1998).

GC Name	$E_{\rm th}$ (TeV)	Diff $F_{\rm UL}$ at 1 TeV $\times10^{-12}$(cm^{-2}s^{-1}TeV^{-1})	$F_{\rm UL}(E>E_{\rm th})$ $\times10^{-12}$(ph cm^{-2}s^{-1})	$E_{\rm min}$ (TeV)	$E_{\rm max}$ (TeV)
(i) Standard cuts					
NGC 104	0.83	2.7	2.4	0.75	75.0
NGC 6388	0.46	0.97	2.0	0.29	61.9
NGC 7078	0.42	0.87	2.1	0.38	61.9
Terzan 6	0.56	1.0	1.6	0.26	90.9
Terzan 10	0.46	1.1	2.2	0.21	61.9
NGC 6715	0.26	0.58	2.8	0.24	68.1
NGC 362	0.83	0.75	0.67	0.75	90.9
Pal 6	0.51	0.85	1.5	0.21	90.9
NGC 6256	0.29	3.4	15	0.26	61.9
Djorg 2	0.46	1.7	3.6	0.26	46.4
NGC 6749	0.46	1.4	3.0	0.29	68.1
NGC 6144	0.42	4.3	11	0.26	61.9
NGC 288	0.42	0.38	0.93	0.24	61.9

GC Name	$E_{\rm th}$ (TeV)	Diff $F_{\rm UL}$ at 1 TeV $\times 10^{-12}$(cm^{-2}s^{-1}TeV^{-1})	$F_{\rm UL}(E > E_{\rm th})$ $\times 10^{-12}$(ph cm^{-2}s^{-1})	$E_{\rm min}$ (TeV)	$E_{\rm max}$ (TeV)
HP 1	0.42	1.3	3.1	0.21	61.9
Terzan 9	0.46	1.2	2.6	0.20	61.9
(*ii*) Hard cuts					
NGC 104	1.96	3.0	0.73	1.33	75.0
NGC 6388	0.75	0.78	0.80	0.50	61.9
NGC 7078	0.83	1.4	1.3	0.75	51.1
Terzan 6	0.83	0.68	0.60	0.46	68.1
Terzan 10	0.75	1.3	1.4	0.38	56.2
NGC 6715	0.46	0.45	0.96	0.42	56.2
NGC 362	2.15	1.5	0.31	1.33	90.9
Pal 6	0.62	0.43	0.59	0.38	90.9
NGC 6256	0.83	2.5	2.2	0.46	61.9
Djorg 2	0.75	1.2	1.2	0.51	42.2
NGC 6749	0.91	1.5	1.2	0.51	68.1
NGC 6144	0.10	3.1	1.8	0.46	56.2
NGC 288	0.91	0.45	0.34	0.42	61.9
HP 1	0.75	0.97	0.99	0.38	61.9
Terzan 9	0.75	1.2	1.2	0.38	56.2
(*iii*) Loose cuts					
NGC 104	0.83	2.0	3.3	0.68	82.5
NGC 6388	0.29	0.96	4.2	0.23	61.9
NGC 7078	0.42	0.99	2.4	0.35	61.9
Terzan 6	0.38	0.74	2.1	0.24	90.9
Terzan 10	0.29	1.2	5.3	0.18	61.9
NGC 6715	0.26	0.78	3.9	0.20	82.5
NGC 362	0.83	0.67	0.6	0.68	90.9
Pal 6	0.26	0.71	3.6	0.18	90.9
NGC 6256	0.26	3.6	18	0.22	61.9
Djorg 2	0.29	2.0	8.8	0.24	51.1

GC Name	$E_{\rm th}$ (TeV)	Diff $F_{\rm UL}$ at 1 TeV $\times 10^{-12}$(cm^{-2}s^{-1}TeV^{-1})	$F_{\rm UL}(E > E_{\rm th})$ $\times 10^{-12}$(ph cm^{-2}s^{-1})	$E_{\rm min}$ (TeV)	$E_{\rm max}$ (TeV)
NGC 6749	0.42	0.94	2.3	0.26	68.1
NGC 6144	0.26	4.9	25	0.22	61.9
NGC 288	0.26	0.55	2.8	0.22	61.9
HP 1	0.26	1.2	6.1	0.18	61.9
Terzan 9	0.29	1.2	5.2	0.18	61.9

Table 3.4: The table contains information about the energy threshold of the analysis; differential flux upper limits at 1 TeV and integral photon flux upper limits at a 99% c.l. assuming a power-law spectrum with an index of 2.5; and the minimum and maximum energy.

I added Terzan 5 to the list of sources as it is the only GC that H.E.S.S. has detected. The data I analysed for Terzan 5 were obtained by H.E.S.S. from 2004 to 2010, spanning for about 87 hours. I note that the significance for Terzan 5 reaches 6σ for standard and loose cuts and 7.1σ for hard cuts.

GC Name	Types of cuts	$E_{\rm th}$ (TeV)	Diff Flux at 1 TeV ($\times 10^{-12}$) (cm^{-2}s^{-1}TeV^{-1})	Flux($E > E_{\rm th}$) $\times 10^{-12}$ (ph cm^{-2}s^{-1})	$E_{\rm min}$ (TeV)	$E_{\rm max}$ (TeV)	Sig. (σ)
Terzan 5	Standard	0.26	0.97	4.9	0.20	75.0	6.0
-	Hard	0.91	0.61	0.47	0.38	75.0	7.1
-	Loose	0.26	1.5	7.8	0.18	75.0	6.0

Table 3.5: The table contains information about the energy threshold of the analysis; differential flux at 1 TeV and integral photon flux at a 99% c.l. assuming a power-law spectrum with an index of -2.5; the minimum and maximum energy, and the significance for Terzan 5.

In addition to this anaysis, I also analysed some sources that have been detected by *Fermi* LAT that operates in the energy range from 20 MeV to above 500 GeV. Zhang et al. (2016) reported the discovery of γ-ray emission from GCs M 15, NGC 6397, NGC 5904, NGC 6218, and NGC 6139. In the third *Fermi* catalogue (3FGL) there are 16 listed γ-ray GCs. I checked for data for these sources in the H.E.S.S. database, and I found and analysed data of four sources using HAP and applied standard cuts.

GC Name	Livetime (h)	$N_{\rm ON}$	$N_{\rm OFF}$	$\frac{1}{\alpha}$	Sig. (σ)	$E_{\rm th}$ (TeV)	Diff $F_{\rm UL}$ at 1 TeV ($\times 10^{-12}$) (cm^{-2}s^{-1}TeV^{-1})	$F_{\rm UL}(E > E_{\rm th})$ $\times 10^{-12}$ (ph cm^{-2}s^{-1})
(i) Standard cuts								
NGC 5139	11.8	241	3 991	17.9	1.1	0.46	2.5	5.5
NGC 6624	4.50	30	537	18.8	0.3	0.62	1.9	2.6
2MS-GC01	101.8	2374	19 956	8.80	2.1	0.26	3.1	15
NGC 6316	7.17	154	2 802	17.8	-0.3	0.26	1.1	5.3

Table 3.6: In this table, I list the details of the final analysis. The colums are GC names, livetime of H.E.S.S. observational runs passing standard quality selection cuts; total number of ON and OFF counts; ratio of ON and OFF exposures when applying a reflected-background technique; the detection significance; the energy threshold of the analysis; differential flux upper limits at 1 TeV and the integral photon flux upper limits at a 99% c.l.

I obtained the detection significance below the threshold of 5σ required for a firm detection by H.E.S.S. (see Table 3.6). In addition to this analysis, I also checked the entire Harris catalogue (Harris, 2010) to see if there were some new data for some souces and found data for a few sources but their detection significances were also below the 5σ.

3.5 Comparison of Analysis Results

In this section I compare our results with those of Abramowski et al. (2013). According Figure 3.6, the differential flux upper limits of the 2013 analysis using standard cuts are generally lower than those from the current analysis using standard cuts, except for NGC 362, HP 1, and Terzan 9. This is because Abramowski et al. (2013) had lower energy thresholds. Different cuts (standard, hard, and loose) give different results. From Figure 3.6 and Figure 3.7 it can seen that the loose cuts give higher differential flux and integral flux upper limits than all the other cuts. For the other cuts, the upper limits are quite close to the 2013 results.

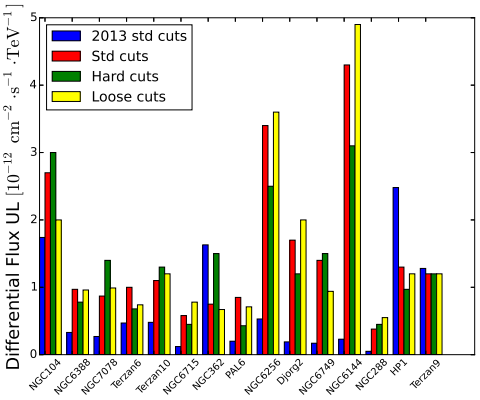

Figure 3.6: Comparison of differential flux upper limits for 2013 data (standard cuts) vs. standard, hard, and loose quality cuts for our analysis of various GCs.

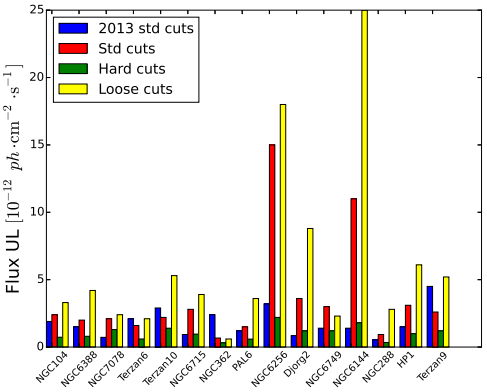

Figure 3.7: Comparison of integral photon flux upper limits assuming a power-law spectrum with an index of 2.5 for 2013 data (standard cuts) vs. standard, hard, and loose quality cuts for our analysis of various GCs.

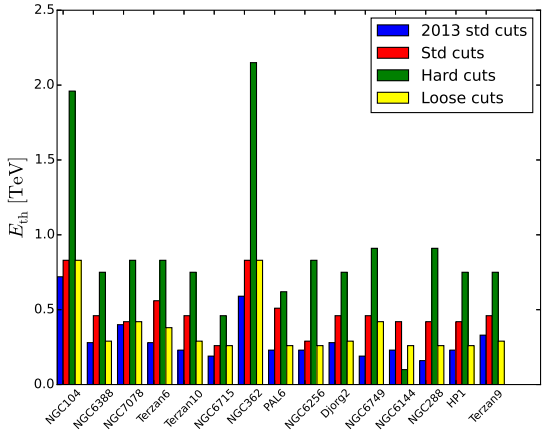

Figure 3.8: Comparison of the energy threshold of the 2013 analysis data (standard cuts), vs. standard, hard, and loose quality cuts for our analysis of various GCs.

One can observe the same effect in Figure 3.7 and Figure 3.8, where it can be seen that the flux upper limits and the energy theresholds for the current analysis with standard quality cuts are generally higher than those of the 2013 analysis (standard cuts). The energy thresholds are higher because the analysis chain used by Abramowski et al. (2013) is more sensitive to low-energy γ-rays than our analysis chain (HAP). According to Figure 3.8, the energy threshold using hard cuts is higher (almost double) than all the other quality selection cuts. This is because hard cuts allow a 160-p.e. cut on image intensity, and increases the energy threshold because of the stricter cut on the image amplitude.

The total detection significance with the stacking analysis obtained by Abramowski et al. (2013) was 2.4σ and I obtained 0.1σ for standard cuts. I used a different analysis chain than Abramowski et al. (2013); furthermore, I note that adding the ON and OFF counts of individual GCs do not give the totals they published. I rechecked their stacking analysis and obtained 1.2σ. However it can also be seen that the results for energy threshold by Abramowski et al. (2013) are quite similar to my results, i.e., the 2013 results using standard cuts are not that different from my results that were obtained using standard cuts.

3.6 Summary

I analysed the H.E.S.S. data of 15 GCs, and no individual GC or stacking analysis show significant excess emission above the threshold of 5σ. I also analysed Terzan 5 data and noted that Terzan 5 is the only Galactic GC detected by H.E.S.S. with a significance of 6σ for standard and loose cuts, and 7.1σ for hard cuts. I also found no detection for Fermi sources. My new results compare well with those of Abramowski et al. (2011) who obtained a significance of 5.3σ. I have also obtained differential and integral flux upper limits for the 15 non-detected GCs. Next, I will discuss the numeric emission model and use the analysis results to constrain this model in chapter 6.

Chapter 4

The Model

In the previous chapter I discussed H.E.S.S. observations and data analyses of GCs. The discussion included the selection criteria of the GCs that were analysed, previous data analysis of the selected sources, the HAP analysis chain, results of my analysis, and comparison between my results and those obtained by Abramowski et al. (2013). In this chapter I will discuss previous spectral modelling of GCs and the challenges necessitating a refined modelling approach. I will then discuss a spherical model also used in this study that calculates the particle transport (including diffusion and radiation losses) and predicts the SED emitted by GCs for a very broad energy range by considering SR as well as IC emission. This discussion is based on Kopp et al. (2013).

4.1 Earlier GC Modelling

Chen (1991) was first to estimate the γ-ray luminosity L_γ of GCs due to the collective emission of host MSPs. Wei et al. (1996) performed similar spectral calculations using an outer gap model. Harding et al. (2005) estimated the total contribution from the GC millisecond pulsars (MSPs) in the GeV band by summing up individual predicted pulsed CR spectra from members of an ensemble of MSPs. Next, Bednarek & Sitarek (2007) considered a model where leptons are injected by MSPs and accelerated to a power-law spectrum at the relativistic shocks that are created during collisions of pulsar winds inside the cores of GCs. These particles radiate unpulsed IC radiation and SR. Venter & de Jager (2008) modelled cumulative pulsed CR from $N_{\rm MSP} = 100$ GC MSPs by randomising over pulsar geometry as well as pulsar period P and period derivative $\dot{P}$. Harding et al.

(2005); Venter et al. (2009b) assumed a pair-starved polar cap (PSPC) electric field to estimate the GeV GC flux and according to Venter & de Jager (2005), the high-energy (HE) flux scales with the $N_{\rm MSPs}$, and thus observations may be used to constrain the average accelerating electric field and polar cap current. The procedure to estimate the cumulative CR flux was improved by Venter & de Jager (2010) and the resulting prediction (Venter et al., 2009a) corresponded to the measured spectrum of 47 Tucanae by *Fermi* LAT to within a factor of two in both energy and flux.

Cheng et al. (2010) explored an alternative model to produce GeV emission and calculated IC (not CR) radiation from electrons and positrons upscattering the cosmic microwave background (CMB), stellar photons, and the Galactic background radiation. They assumed a two-valued step-like spatial dependence for their diffusion coefficient and constrained the coefficient using spatial γ-ray details from *Fermi* LAT. Similarly, Büsching et al. (2011) (and later Kopp et al. 2013) attempted to constrain the diffusion coefficient by performing a line-of-sight (LOS) calculation to model diffuse X-rays for Terzan 5 finding roughly similar results to those of Cheng et al. (2010). Cheng et al. (2010) noted that IC emission should extend beyond 10 pc from the centre of the GC, giving rise to an extended source. Their model also predicts VHE (> 100 GeV) components in some cases. Hui et al. (2011) followed this idea and found a correlation between the GeV L_γ and the stellar encounter rate, and also between L_γ and the metalicity [Fe/H]. They also found a correlation between L_γ and the Galactic background soft-photon energy densities in different wavebands. This supports the idea of Cheng et al. (2010) that the GeV flux is due to ICS. On the other hand, Freire et al. (2011) and Johnson et al. (2013) detected energetic γ-ray pulsars in M 28 and NGC 6624, dominating the GeV emission, and thus pointing to a CR origin of the GeV emission. The GeV emission may therefore be a mixture of inverse Compton scattering (ICS) and CR.

Venter et al. (2009a) constrained $N_{\rm MSP}$ and cluster magnetic field B using *Fermi* LAT data and H.E.S.S. sensitivity curves for Terzan 5 and 47 Tucanae (NGC 104) by using their IC and CR calculations. They performed particle transport assuming a steady-state scenario, Bohm diffusion, calculating ICS on the CMB and stellar photons using a two-zone model. They also performed an SR calculation by assuming a homogeneous cluster magnetic field B. The data of Terzan 5 obtained by H.E.S.S. imply that reacceleration of particles may take place in the GC, because a power-law spectrum was measured in the TeV band, implying a power-law particle injection spectrum. Prinsloo et al. (2013) extended the model of Venter et al. (2009b) by calculating the

soft-photon energy density profile for many zones $u(r_s)$ (with r_s the radial distance from the centre) from first principles, to reproduce the result of Bednarek & Sitarek (2007). They noted that it is important to add a third large outer zone because the emission does not drop off within the first two zones as assumed by Venter et al. (2009a).

Bednarek (2012) discussed the contribution of non-accreting magnetised white dwarfs (WDs) to the γ-ray emission from GCs. He noted that relativistic leptons should upscatter the surrounding soft photons to GeV/TeV energies when leaving the magnetospheres of WDs, which is very similar to the MSPs scenario. Bednarek (2012) concluded that if one includes the decay of the WD magnetic fields and different scenarios for formation and evolution of WDs, then depending on the parameters of the model (e.g., if a few thousand WDs are formed within the lifetime of GCs) they might actually produce γ-ray emission at a flux level detectable by the CTA.

In contrast to the leptonic models discussed above, Domainko (2011) investigated a model based on γ-ray burst remnants as sources of hadrons and energetic leptons. When one considers a short burst that is a result of the merger of two neutron stars, some fraction of the shock wave energy might be tapped and accelerate hadrons following the explosion. Collisions of energetic hadronic cosmic rays with ambient target nuclei may lead to the subsequent formation of leptons and π^0 particles that decay into γ-rays. Domainko (2011) used the observed VHE extension of the γ-ray source associated with Terzan 5 to constrain the diffusion coefficient κ_0 and compared the burst age with the short burst occurrence rate. He noted that the extension would be compatible with a relatively slow diffusion of hadrons in the cluster. He also noted that there might be a number of multi-wavelength signatures that may provide support for this scenario, e.g., diffuse X-rays from IC by accelerated electrons by the blast wave, and diffuse thermal X-rays originating from hot plasma. For more detailed reviews of gamma-ray observations and modelling of GCs (see Bednarek 2013; Tam et al. 2016).

4.2 Challenges Necessitating a Refined Modelling Approach

Although the leptonic models have had some success in reproducing the observed multi-wavelength GC spectra, there are still some challenges, both observational and theoretical. The relative contribution of ICS versus CR in the GeV band is not clear (see Cheng et al. 2010). The GeV spectral cutoffs obtained by Venter et al. (2009a) were a little high, reflecting the uncertainty in the mag-

netospheric acceleration potential. Tam et al. (2011) showed that some GCs had large cutoffs, which might either point to an IC origin of the emission, reflect uncertainties in the diffuse soft photon background, or indicate that the GeV emission originated from other nearby contaminating sources that inhibits fitting of a spectral cutoff. In Abdo et al. (2010), there were large errors on the inferred $N_{\rm MSP}$, influencing the normalisation of the injection spectrum. Even though some GCs have been detected in γ-rays, there are no detected radio or X-ray MSPs in their direction, which is unexpected. The details of acceleration of injected particles are still unknown, hence the spectral shapes of the injected particles are uncertain.

On the other hand, there are a few observational facts that need to be explained specifically for Terzan 5. The VHE source is highly asymmetric and extended, and significantly offset from the centre of the GC, while the diffuse X-ray emission is more localised and centred on the cluster. To explain this, Cheng et al. (2010); Büsching et al. (2011); Tam et al. (2011) proposed possible causes such as MSPs originating near the tidal radius, a small sub-population of energetic MSPs possibly skewing spatial properties of the γ-ray emission, non-uniform soft-photon energy density profiles, contributions from non-optical soft-photon target fields, an asymmetric diffusion coefficient, proper motion of the GC (Bednarek & Sobczak, 2014), the contribution of non-MSP sources, or even background sources. The observed diffuse X-ray emission has a hard spectral index that is difficult to match in the leptonic model using SR, and hence raises the question of an alternative interpretation of this component. Also, the mismatch of γ-ray and X-ray source shapes and extensions raises questions on whether they are from the same origin with respect to the underlying leptonic population.

Some of the abovementioned issues are addressed by the model of Kopp et al. (2013). They implemented a power-law injection spectrum, an LOS calculation of the X-ray surface brightness to constrain the diffusion coefficient, an additional Galactic background soft-photon target energy density, a refined stellar soft-photon energy density profile $u(r_{\rm s})$, and full particle transport (including diffusion and radiation losses) with the assumption of spherical symmetry and in a steady-state regime. In this model, Kopp et al. (2013) used both a multi-wavelength and a population approach in which they averaged over several single-MSP properties to reduce uncertainties. Bednarek et al. (2016) developed a basic model for TeV γ-ray emission due to the Comptonisation of the background radiation within a GC by energetic leptons injected directly from the inner magnetosphere of the MSPs re-accelerated in their vicinity. Below, I describe the Kopp et al. 2013 model in more

detail, since I will apply it to several GCs in Chapter 6.

4.3 Spherically-Symmetric GC Model Used in this Study

The model by Kopp et al. (2013) calculates the particle transport (including diffusion and radiation losses) and predicts the SED from GCs for a very broad energy range by considering SR and IC.

4.3.1 Transport Equation

A Fokker-Planck type equation (Parker, 1965) prescribes the transport of charged energetic particles i.e., electrons and positrons, in phase space. Neglecting spatial convection, we have (Kopp et al., 2013):

$$\frac{\partial n_{\rm e}}{\partial t} = \vec{\nabla}\cdot(\vec{\kappa}\cdot\vec{\nabla}n_{\rm e}) - \frac{\partial}{\partial E_{\rm e}}(\dot{E}n_{\rm e}) + Q, \tag{4.1}$$

where $n_{\rm e}$ is the electron density per energy and volume and is a function of the central GC radius $r_{\rm s}$, $E_{\rm e}$ the electron energy, $\vec{\kappa}$ is the diffusion tensor, $\dot{E}$ the radiation losses, and Q the electron source term. Considering scalar diffusion, and time independence i.e., $\frac{\partial}{\partial t}=0$, $n_{\rm e}$ depends only on $\vec{r}_{\rm s}$ and $E_{\rm e}$, and Equation (4.1) becomes

$$0 = \vec{\nabla}\cdot(\vec{\kappa}\cdot\vec{\nabla}n_{\rm e}) - \frac{\partial}{\partial E_{\rm e}}(\dot{E}n_{\rm e}) + Q. \tag{4.2}$$

We next set $\vec{\nabla}n_{\rm e} = \frac{\partial n_{\rm e}}{\partial r_{\rm s}}\vec{e_{r_{\rm s}}}$ and $\frac{\partial}{\partial\theta} = \frac{\partial}{\partial\phi} = 0$, with $\vec{e}_{\rm r}$ the radial unit vector, giving

$$0 = \frac{1}{r_{\rm s}^2}\frac{\partial}{\partial r_{\rm s}}\left(r_{\rm s}^2\kappa\frac{\partial n_{\rm e}}{\partial r_{\rm s}}\right) - \frac{\partial}{\partial E_{\rm e}}(\dot{E}n_{\rm e}) + Q. \tag{4.3}$$

This Equation can be expressed as follows:

$$\frac{\partial}{\partial E_{\rm e}}(\dot{E}n_{\rm e}) = \frac{1}{r_{\rm s}^2}\frac{\partial}{\partial r_{\rm s}}\left(r_{\rm s}^2\kappa\frac{\partial n_{\rm e}}{\partial r_{\rm s}}\right) + Q \tag{4.4}$$

$$\dot{E}\frac{\partial n_{\rm e}}{\partial E_{\rm e}} + n_{\rm e}\frac{\partial\dot{E}}{\partial E_{\rm e}} = \frac{1}{r_{\rm s}^2}\frac{\partial}{\partial r_{\rm s}}\left(r_{\rm s}^2\kappa\frac{\partial n_{\rm e}}{\partial r_{\rm s}}\right) + Q \tag{4.5}$$

$$\frac{\partial n_{\rm e}}{\partial E_{\rm e}} = \frac{1}{\dot{E}}\left(\frac{1}{r_{\rm s}^2}\frac{\partial}{\partial r_{\rm s}}\left(r_{\rm s}^2\kappa\frac{\partial n_{\rm e}}{\partial r_{\rm s}}\right) - n_{\rm e}\frac{\partial\dot{E}}{\partial E_{\rm e}} + Q\right). \tag{4.6}$$

Equation (4.6) can be solved numerically using a Crank-Nicolson algorithm.

Assuming the source term Q is located at $\vec{r}_{\rm s} = \vec{r}_{\rm inj}$, and is a power law in energy, I have

$$Q = Q_0 \frac{\delta(\vec{r}_{\rm s} - \vec{r}_{\rm inj})}{E_{\rm e}^{\Gamma}}, \tag{4.7}$$

where Γ is the spectral index. Using the Gauss theorem and assuming $\dot{E} = 0$ for the innermost zone, the source term Q may be replaced by a boundary condition:

$$0 = \vec{\nabla}.(\kappa\vec{\nabla}n_{\rm e}) + Q_0 \frac{\delta(\vec{r}_{\rm s} - \vec{r}_{\rm c})}{E_{\rm e}^{\Gamma}} \tag{4.8}$$

$$-\frac{Q_0}{E_{\rm e}^{\Gamma}} = \oint \kappa(\vec{\nabla}n_{\rm e}) \cdot d\vec{A} \tag{4.9}$$

$$\left.\frac{\partial n_{\rm e}}{\partial r_{\rm s}}\right|_{r_{\rm s,min}} = -\frac{Q_0}{4\pi r_{\rm s,min^2} \kappa(E_{\rm e}, r_{s,\rm min}) E_{\rm e}^{\Gamma}}, \tag{4.10}$$

with $r_{\rm min}$ bounding the spherical region containing all particle sources. It is assumed that all the sources (MSPs) are contained within the inner boundary of the simulation region $r_{\rm min} = 0.01$ pc.

4.3.2 Spatial Diffusion

Two different diffusion coefficients are used. First, for Bohm diffusion we have

$$\kappa(r_{\rm s}, E_{\rm e}) = \kappa_B \frac{E_{\rm e}}{B(r_{\rm s})}, \tag{4.11}$$

where $\kappa_B = c/3e$, with c being the speed of light, and e is the elementary charge. Second, I also consider a diffusion coefficient inspired by Galactic cosmic-ray propagation studies.

$$\kappa(r_{\rm s}, E_{\rm e}) = \kappa_0 \Big(\frac{E_{\rm e}}{E_0}\Big)^{\alpha}, \tag{4.12}$$

with $E_0 = 1$ TeV and $\alpha = 0.6$, e.g., Moskalenko & Strong 1998.

4.3.3 Particle Injection Spectrum

Since H.E.S.S. detected a power-law spectrum for the VHE source associated with Terzan 5, it is assumed that the particle injection spectrum is also a power law (see Equation [4.7]):

$$Q(E_{\rm e}) \quad = \quad Q_0 E_{\rm e}^{-\Gamma} \tag{4.13}$$

between energies $E_{\rm e,min}$ and $E_{\rm e,max}$. The shape of the spectrum can be due to particle acceleration at the relativistic shocks that are formed during collisions of pulsar winds inside the cores of GCs (Bednarek & Sitarek, 2007). If this is the case and diffusive shock acceleration takes place, a power-law shape is expected (see, e.g., Longair 2011). The normalisation of the injection spectrum requires

$$L_{\rm e} \equiv \int_{E_{\rm e,min}}^{E_{\rm e,max}} E_{\rm e} Q dE_{\rm e} \quad = \quad N_{\rm MSP}\eta\langle\dot{E}_{\rm rot}\rangle, \tag{4.14}$$

with η the fraction of the average spin-down power $\dot{E}_{\rm rot}$ converted into particle power.

4.3.4 Radiation losses: Energy Loss Terms

For ICS and SR (Section 2.2), one needs to specify the energy loss ($\dot{E}$) per particle. For simplicity, I assumed isotropic photon and electron distributions in what follows. IC losses in the general case (Thomson and Klein-Nishina limits; Blumenthal & Gould 1970) are given by

$$\dot{E}_{\rm IC}(E_{\rm e}, r_{\rm s}, T) \quad = \quad -\sum_{j=0}^{k-1} \int \chi(E_\gamma, E_{\rm e}, u_{{\rm rad},j}, T_j) dE_\gamma, \tag{4.15}$$

where k is the total number of (blackbody) soft-photon components, E_γ represents the final energy of the upscattered photons, $u_{{\rm rad},j}$ is the energy density of the soft-photons, T_j is the photon temperature of component j, and h is Planck's constant. The function χ is given by

$$\chi(E_\gamma, E_{\rm e}, u_{{\rm rad},j}, T_j) \quad = \quad \int n_{\varepsilon,j}(r_{\rm s}, \varepsilon, T_j) \frac{E_\gamma}{E_0} \zeta(E_{\rm e}, E_\gamma, \varepsilon) d\varepsilon, \tag{4.16}$$

with $n_{\varepsilon,j}$ the photon density of the blackbody emitter, and E_0 the electron rest energy assuming isotropic photon and electron distributions. The collision rate ζ is given by

$$\zeta(E_\mathrm{e}, E_\gamma, \varepsilon) = \frac{2\pi e^4 E_0 c}{\varepsilon E_\mathrm{e}^2}\hat{\zeta}(E_\mathrm{e}, E_\gamma, \varepsilon), \tag{4.17}$$

where (Jones, 1968)

$$\hat{\zeta}(E_\mathrm{e}, E_\gamma, \varepsilon) = \begin{cases} 0 & \text{if} \quad E_\gamma \leqslant \frac{\varepsilon E_0^2}{4E_\mathrm{e}^2}, \\ \frac{E_\gamma}{\varepsilon} - \frac{E_0^2}{4E_\mathrm{e}^2} & \text{if} \quad \frac{\varepsilon E_0^2}{4E_\mathrm{e}^2} \leqslant E_\gamma \leqslant \varepsilon, \\ f(q, g_0) & \text{if} \quad \varepsilon \leqslant E_\gamma \leqslant \frac{4\varepsilon E_\mathrm{e}^2}{E_0^2 + 4\varepsilon E_\mathrm{e}}, \\ 0 & \text{if} \quad E_\gamma \geqslant \frac{4\varepsilon E_\mathrm{e}^2}{E_0^2 + 4\varepsilon E_\mathrm{e}}. \end{cases}$$

The function $f(q, g_0)$ is defined as:

$$f(q, g_0) = 2q \ln q + (1-q)(1 + (2 + g_0)q),$$

with $q = E_0^2 E_\gamma / (4\varepsilon E_\mathrm{e}(E_\mathrm{e} - E_\gamma))$ and $g_0(\varepsilon, E_\gamma) = 2\varepsilon E_\gamma / E_0$. All terms put together gives (with $g_\mathrm{IC} = 2\pi e^4 c$):

$$\dot{E}_\mathrm{IC}(E_\mathrm{e}, r_\mathrm{s}, T_j) = -\frac{g_{IC}}{E_\mathrm{e}^2} \sum_{j=0}^{k-1} \iint n_{\varepsilon,j}(r_\mathrm{s}, \varepsilon, T_j) \frac{E_\gamma}{\varepsilon} \hat{\zeta}(E_e, E_\gamma, \varepsilon) d\varepsilon dE_\gamma. \tag{4.18}$$

In the SR case, the loss rate (averaged over all pitch angles) is given by (Blumenthal & Gould, 1970)

$$\dot{E}_\mathrm{SR}(E_\mathrm{e}, r_\mathrm{s}) = -\frac{g_\mathrm{SR}}{8\pi} E_\mathrm{e}^2 B^2(r_\mathrm{s}), \tag{4.19}$$

with $g_\mathrm{SR} = 4\sigma_T c / 3E_0^2 = 32\pi(e/E_0)^4 c/9$, where σ_T denotes the Thomson cross section.

4.3.5 Target Soft-photon Energy Densities

One needs to specify the soft-photon densities in order to calcualte $\dot{E}_{\rm IC}$. For a blackbody, Kopp et al. (2013) used a photon density (see also Zhang et al. 2008):

$$n_{\varepsilon,j}(r_{\rm s},\varepsilon,T_j) = \frac{15u_{{\rm rad},j}(r_{\rm s},T_j)}{(\pi k_B T_j)^4}\frac{\varepsilon^2}{e^{\frac{\varepsilon}{k_{\rm B}T_j}}-1}, \tag{4.20}$$

where $u_{{\rm rad},j}$ is photon energy density of the j^{th} component of soft-photon field and $k_{\rm B}$ is Boltzmann's constant. Kopp et al. (2013) included the CMB, stellar photons, and the Galactic background radiation field at the position of the GC. For the soft-photon component they used an LOS integration (see Prinsloo et al. 2013)

$$n_{\varepsilon,j}(r_{\rm s},\varepsilon,T_1) = \frac{8\pi}{h^3c^3}\frac{\varepsilon^2}{e^{\frac{\varepsilon}{k_{\rm B}T_1}}-1}\left(\frac{1}{2}\frac{N_{\rm tot}R_\star^2}{R_{\rm c}^2\widetilde{R}}\right)\int_{r'=0}^{r'=R_t}\hat{\rho}(r')\frac{r'}{r_{\rm s}}\ln\left(\frac{\mid r'+r_{\rm s}\mid}{\mid r'-r_{\rm s}\mid}\right)dr', \tag{4.21}$$

where $N_{\rm tot}$ represents the total number of cluster stars that can be written as $N_{\rm tot} = M_{\rm tot}/m$, with $M_{\rm tot}$ the total mass of the cluster, and m the average stellar mass. Here, $R_\star$ is the average stellar radius, $R_{\rm c}$ indicates the core radius of the cluster, and $\widetilde{R} = 2R_{\rm h} - 2R_{\rm c}/3 - R_{\rm h}^2/R_{\rm r}$, with $R_{\rm h}$ the half-mass radius and $R_{\rm t}$ the tidal radius of the cluster. Kopp et al. (2013) used solar values for $R_\star$ and m, assuming that all stars in the simulation have a solar radius and temperature $T = 4\ 500\ K$. In this study I used only the CMB and stellar photon field.

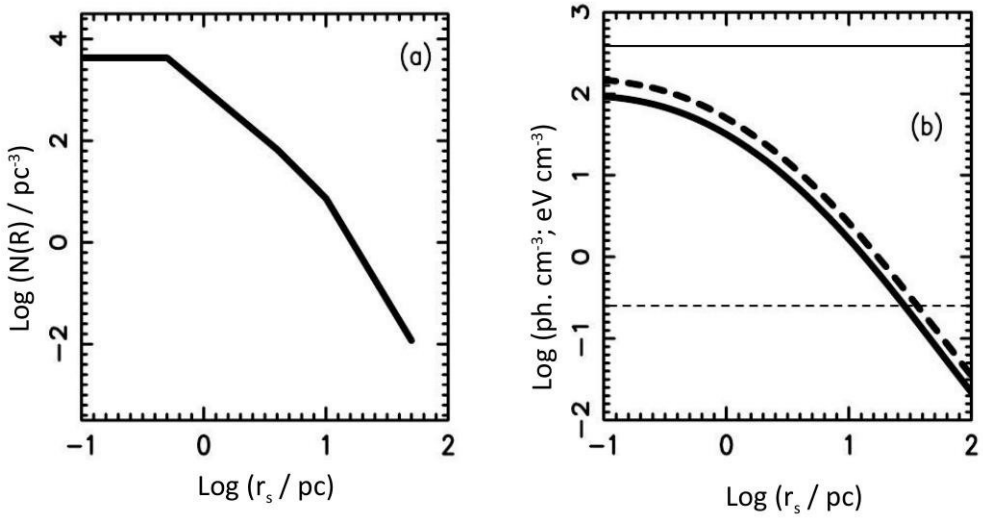

Figure 4.1: The assumed density of stars (a), and photon and energy density of stellar photons (b) as a function of distance $r_{\rm s}$ from the centre of a typical GC. The energy density and photon density are illustrated by thick dashed and solid curves. The thin horizontal lines show the corresponding values for the CMB. From Bednarek & Sitarek (2007).

The following normalised stellar density function was assumed (see Figure 4.1, Bednarek & Sitarek 2007):

$$\hat{\rho}(r') = \begin{cases} 1 & \text{if} \quad r' < R_{\rm c} \\ \left(\frac{R_{\rm c}}{r'}\right)^2 & \text{if} \quad R_{\rm c} \leqslant r' < R_{\rm h} \\ \frac{(R_{\rm c} R_{\rm h})^2}{r'^2} & \text{if} \quad R_{\rm h} \leqslant r' < R_{\rm t} \\ 0 & \text{if} \quad r' \geqslant R_{\rm t}. \end{cases}$$

4.3.6 Calculation of the Photon Spectra

To calculate the IC scattering emissivities, Kopp et al. (2013) used the following expression

$$X_{\rm IC}(E_\gamma, r_{\rm s}) = \left(\frac{dN_\gamma}{dE_\gamma}\right)_{\rm IC} \tag{4.22}$$

$$= \frac{g_{\rm IC}}{A} \sum_{j=0}^{k-1} \iint n_{\varepsilon,j}(r_{\rm s}, \varepsilon, T_j) \frac{N_{\rm e}(E_{\rm e}, r_{\rm s})}{\varepsilon E_{\rm e}^2} \hat{\zeta}(E_{\rm e}, E_\gamma, \varepsilon) d\varepsilon dE_{\rm e}, \tag{4.23}$$

where $A = 4\pi d^2$, with d being the distance from the source, and $N_{\rm e}$ the number of electrons per energy interval in a spherical shell around $r_{\rm s}$. For the SR emissivity, Kopp et al. (2013) used

$$X_{\rm SR}(E_\gamma, r_{\rm s}) = \frac{1}{A} \frac{1}{hE_\gamma} \int P_\nu(E_{\rm e}, \nu, r_{\rm s}) N_{\rm e}(E_{\rm e}) dE_{\rm e}, \tag{4.24}$$

where

$$P_\nu(E_{\rm e}, \nu, r_{\rm s}) = \sqrt{3} \frac{B(r_{\rm s})}{E_0} \int_0^{\pi/2} \tilde{\kappa}\left(\frac{\nu}{\nu_{\rm cr}(E_{\rm e}, \vartheta, r_{\rm s})}\right) \sin^2 \vartheta d\vartheta$$

and with the critical frequency

$$\nu_{\rm cr}(E_{\rm e}, \vartheta, r_{\rm s}) = \frac{3ec}{4\pi E_0^3} E_{\rm e}^2 B(r_{\rm s}) \sin \vartheta. \tag{4.25}$$

The function $\tilde{\kappa}$ is an integral involving a modified Bessel function of order 5/3 (see Equation 2.19):

$$F(x) = x \int_x^\infty K_{5/3}(y) dy. \tag{4.26}$$

We assumed $\vartheta = \pi/2$ for simplicity.

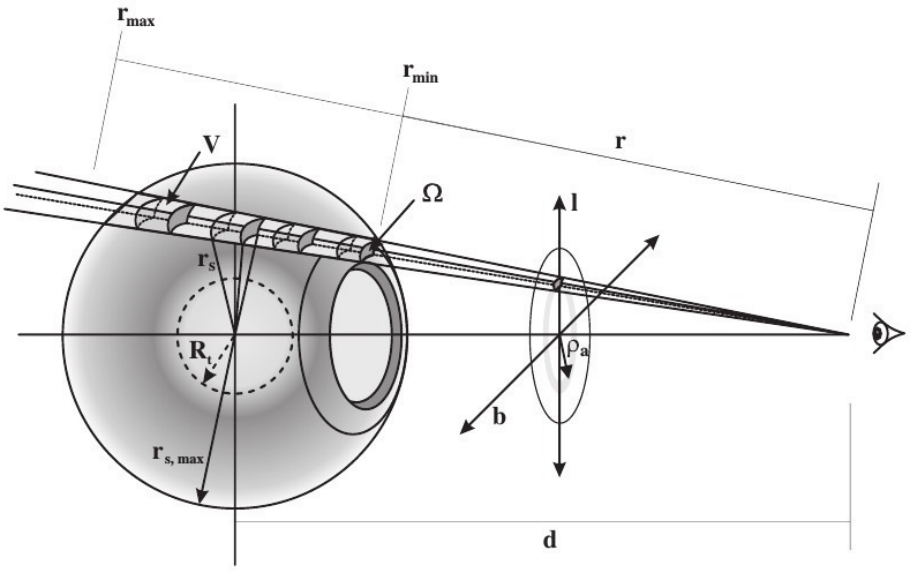

Figure 4.2: Illustration of the geometry assumed for the LOS procedure and the quantities introduced in the text (Kopp et al., 2013).

4.3.7 Calculation of the Sky Map: LOS Integration

To calculate a 2D projected sky map of radiation from the 3D emitting GC, Kopp et al. (2013) defined a Cartesian coordinate system with the observer at the origin and the cluster centre located at $\vec{d} = (d, 0, 0)$. Any observed point, expressed in spherical coordinates, is given by

$$\vec{r} = r(\sin\vartheta\cos\varphi, \sin\vartheta\sin\varphi, \cos\vartheta).$$

This becomes $\vec{r} = r(\cos b\cos l, -\cos b\sin l, \sin b)$ using latitude and longitude coordinates (l and b). The longitude is defined with $l \in (-\frac{\pi}{2}, \frac{\pi}{2})$ and the latitude with $b \in (-\frac{\pi}{2}, \frac{\pi}{2})$ for a hemisphere. Here $\vec{r_s} = \vec{r} - \vec{d}$ is the vector from the cluster centre to the observed point, with

$$r_s = |\vec{r_s}| = \sqrt{r^2 + d^2 - 2rd\cos l\cos b}. \tag{4.27}$$

The flux for a fixed photon energy is:

$$\Phi(l, b, E_\gamma) = \sum_{i=1}^{n_r} \frac{V(r_i, l, b)}{4\pi r_i^2} \chi(E_\gamma, r_s(r_i, l, b)), \tag{4.28}$$

where $n_{\rm r}$ is the number of radiation bins and

$$\chi = \frac{A}{V_{\rm shell}}(X_{\rm SR} + X_{\rm IC}), \tag{4.29}$$

and $V(r_i, l, b)$ is the volume element, with $V_{\rm shell}$ the volume of spherical shell. Kopp et al. (2013) converted Φ into a surface flux by calculating the total flux in a given annulus of the projected image, represented by the grey ring with radius $\rho_{\rm a}$ in Figure 4.2. They used a grid in l and b whereby they denoted the grid points by (r_i, l_j, b_k) and wrote:

$$\Phi_{\rm tot}(E_\gamma, \rho_a) = \sum_{jk} \Phi_{jk}(E_\gamma)\delta_{jk}^{(a)}, \tag{4.30}$$

where $\delta_{jk}^{(a)} = 1$ for grid points belonging to annulus $\rho_{\rm a}$. The surface brightness ($B_\star$) is then

$$B_\star(E_\gamma, \rho_a) = \frac{\Phi_{\rm tot}(E_\gamma)}{\Omega_{\rm tot}^{(a)}}. \tag{4.31}$$

where $\Omega_{\rm tot}^{(a)}$ is the total solid angle subtended by the annulus of radius $\rho_{\rm a}$. The surface brightness profile is lastly obtained by multiplying $B_\star$ with E_γ and integrating over the photon energy:

$$S(\rho_a) = \int_{E_\gamma,{\rm min}}^{E_\gamma,{\rm max}} E_\gamma B_\star(E_\gamma, \rho_a) dE_\gamma. \tag{4.32}$$

4.4 Summary

In this chapter I described the model that I will apply in Chapter 6 to the GCs listed in Chapter 3 to produce SR and IC spectra for each individual cluster. The model includes a transport equation, and I specify the particle injection spectrum, radiation losses, and soft-photon energy densities; I will also calculate photon spectra and perform an LOS integration. In the next chapter I will use the model to study the effect of changing the following parameters: number of stars in the cluster, magnetic field in the cluster, the spectral index, particle injection spectral normalisation, the size of the cluster by changing the distance to the cluster, and the spatial diffusion coefficient.

Chapter 5

Parameter study

In the previous chapter, I have discussed a spherical model that calculates the particle transport and predicts the emitted spectrum from GCs by considering SR as well as IC emission. In this chapter I will perform a parameter study to further investigate the model's behaviour.

5.1 Timescales and Reference Model

I will use several different timescales to study the dominant transport effects as a function of radius, r_s and electron energy, E_e. The Bohm diffusion timescale is given by:

$$t_\mathrm{diff} = \frac{r_\mathrm{s}^2}{2\kappa}, \tag{5.1}$$

$$\kappa(E_\mathrm{e}) = \kappa_\mathrm{B}\frac{E_\mathrm{e}}{B}, \tag{5.2}$$

$$\kappa_\mathrm{B} = \frac{c}{3e}, \tag{5.3}$$

where c denotes the speed of light and e denotes the elementary charge. The SR cooling timescale is given by

$$t_\mathrm{SR} = \frac{E_\mathrm{e}}{\dot{E}_\mathrm{SR}}, \tag{5.4}$$

with (see Equations [2.15] and [4.19])

$$\dot{E}_\mathrm{SR} = -g_\mathrm{SR}E_\mathrm{e}^2U_\mathrm{mag} = \frac{-g_\mathrm{SR}}{8\pi}E_\mathrm{e}^2B^2 \tag{5.5}$$

where

$$g_{\rm SR} = \frac{4}{3}\frac{\sigma_T c}{m_{\rm e}^2 c^4} = \frac{32\pi}{9}\left(\frac{e}{m_{\rm e}c^2}\right)^4 c. \tag{5.6}$$

Also, the IC cooling timescale is given by $t_{\rm IC} = E_{\rm e}/\dot{E}_{\rm IC}$, with (see Equation 4.15)

$$\dot{E}_{\rm IC}(E_{\rm e}, r_{\rm s}, T) \quad = \quad -\sum_{j=1}^{k-1}\int \chi(E_\gamma, E_{\rm e}, u_{{\rm rad,j}}, T_j)\frac{1}{h}dE_\gamma. \tag{5.7}$$

Finally, the total radiation timescale is:

$$t_{\rm rad} \quad = \quad \frac{E_{\rm e}}{\dot{E}_{\rm SR} + \dot{E}_{\rm IC}}. \tag{5.8}$$

The effective timescale (Zhang et al., 2008) is given by:

$$t_{\rm eff}^{-1} = t_{\rm esc}^{-1} + t_{\rm rad}^{-1}. \tag{5.9}$$

In this section I used the parameters listed in Table 5.1 to calculate a reference model for the timescales, particle spectrum, and SED graphs.

Parameters	Parameter values
Diffusion coefficient (κ_0)	Bohm diffusion
Magnetic field (B)	$5\,\mu$G
Injected spectral index (Γ)	2.0
Number of stars ($N_{\rm tot}$)	4.6×10^5
Injected spectral normalisation (Q_0)	6.33×10^{33}erg^{-1} s^{-1}
Distance (d)	5.9 kpc

Table 5.1: In this table I list parameter for the refence model. I used the structural parameter for Terzan 5 (i.e., $R_{\rm c} = 0.21$ pc, $R_{\rm t} = 17.4$ pc, $R_{\rm h} = 0.94$ pc).

In what follows I fix all parameters for the reference model but then just change one parameter at a time as indicated in the subsequent sections.

In Figure 5.1 I plot the timescales of the reference model for diffusion (dash-dotted lines), radiation losses (dashed lines), and the effective timescale (solid lines). The IC cross section drops as one goes from the Thomson regime at low energies to the K-N regime at high energies and therefore SR dominates over IC at the highest energies. From Equations (5.5, 5.6) I note that $t_{\rm SR}$ scales as E^{-1} as seen in Figure 5.1. Close to the core, diffusion dominates (i.e., particles will escape before radiating). At larger radii the situation is reversed and SR losses dominate over diffusion (since

the diffusion timescale scales as r_s^2). At intermediate radii, one can see the change in regime: for $r_s = 0.12R_t$, with R_t the tidal radius, the SR timescale is only slightly lower than the diffusion timescale at the highest particle energies, while SR dominates diffusion at $r_s = 1.2R_t$.

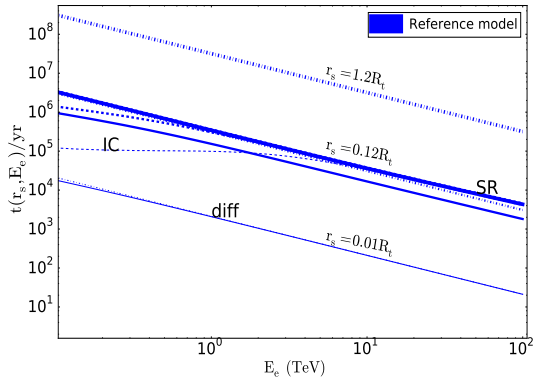

Figure 5.1: Loss timescales as a function of energy at different radii. Dominating processes at different radii and particle energies are indicated in the graph.

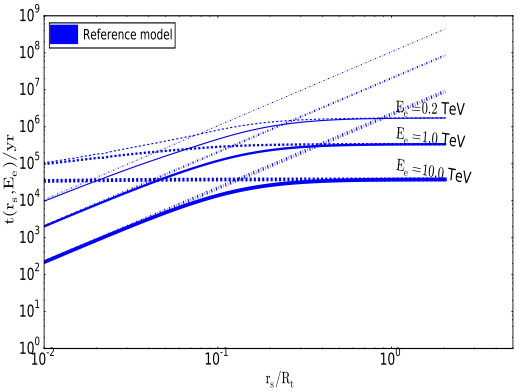

Figure 5.2: Loss timescales as a function of radius at different energies.

As an alternative view, in Figure 5.2 I plot the timescales as a function of radius for diffusion (dash-dotted lines), radiation losses (dashed lines), and the effective scale (solid lines) for different energies. For diffusion, the graph of $t_{\rm diff}$ versus r_s has a slope of 2 (see Equation 5.1). Also, $t_{\rm diff}$ is higher for lower energies, since such particles diffuse slower (this is evident at smaller r_s, where diffusion dominates). At higher particle energies, SR dominates (i.e., $t_{\rm SR}$ is lower). Since I assume that the cluster B-field is not a function of r_s, the graph of $t_{\rm SR}$ versus r_s will be flat for constant E_e. However, $t_{\rm SR}$ is larger for lower particle energies since $t_{\rm SR} \propto E_e^{-1}$. From the plot, it is clear that the effective timescale 'takes the minimum' between $t_{\rm diff}$ and $t_{\rm SR}$ (or $t_{\rm rad}$), always being the lowest timescale. This is what determines the effect of particle transport on n_e. One can again see that diffusion dominates radiation processes at low radii. The inverse is true at larger radii.

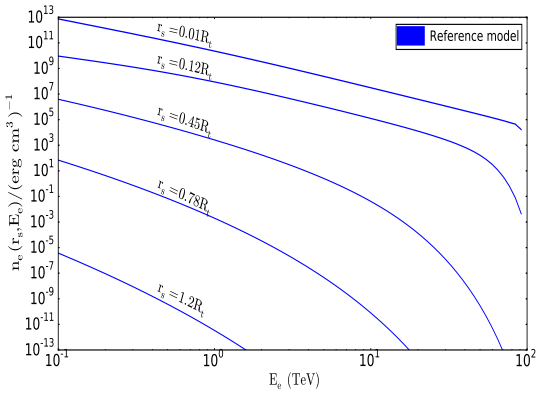

Figure 5.3: The steady-state particle spectrum as a function of energy E_e at different r_s.

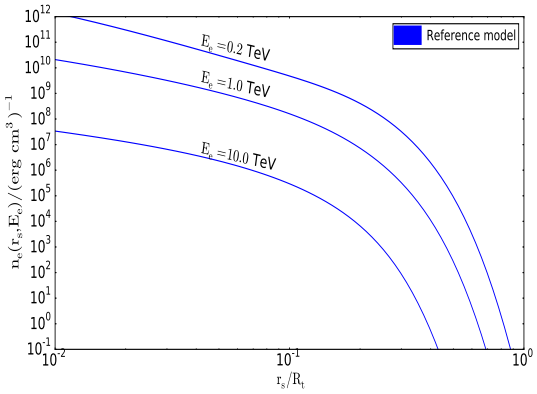

Figure 5.4: The steady-state particle spectrum as a function of radius r_s at different particle energies E_e.

In Figure 5.3 I plot the steady-state particle spectrum as a function of energy E_e at different r_s for the reference model. At a fixed radius, n_e is higher at low energies and become low at higher energies due to the assumed injection spectrum. At small radius, the particle spectrum follows the injection spectrum ($\Gamma = 2.0$), but it becomes softer with distance because high energy particles diffuse faster than low energy particles. One can see that there is a cutoff introduced at higher energies due to SR. The cutoff becomes increasingly lower at larger radii since high-energy particles continue to lose energy due to SR, i.e., the SR losses give rise to the cutoff at high energy (Figure 5.3) and large distances (Figure 5.4).

Figure 5.5 shows the SED predicted by the reference model. It is clear that there are two components associated with the two soft-photon target densities for the IC spectrum. It violates the slope of the X-ray data for Terzan 5. It can be seen that one may potentially fit data for Terzan 5 and therefore one needs to constrain the model parameters (see Chapter 6). In Figure 5.6, I plot the relative contributions from a number of representative radii r_s. The high-energy part of the IC component dominates the SR component at very small distances where the soft-photon background is larger, while the SR one starts to slightly dominate the IC component at larger distances.

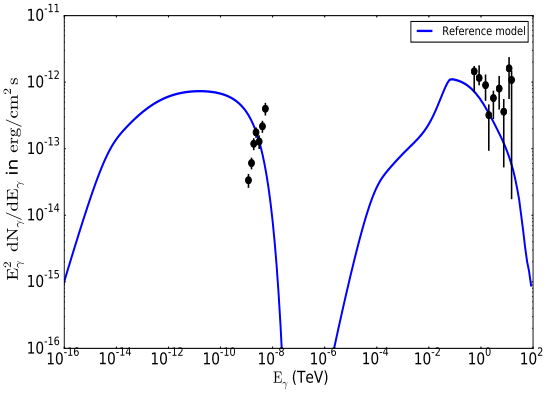

Figure 5.5: SED plot for reference model for Terzan 5.

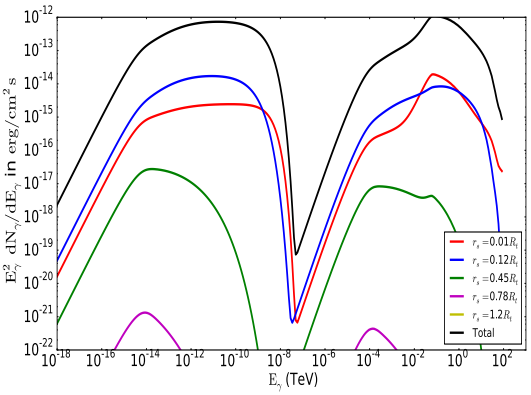

Figure 5.6: Spectra for the reference model.

5.2 Changing the number of stars ($N_{\rm tot}$)

From Equation (19b) in Kopp et al. (2013), I note that the number density of soft photons n_ϵ scales linearly with $N_{\rm tot}$ (see Equation [4.21], where $N_{\rm tot}$ is the number of stars). I therefore note that the IC loss rate also scales linearly with $N_{\rm tot}$ (see Equation [4.15]). In Figure 5.7 I plot the timescales for diffusion (dash-dotted lines), radiation losses (dashed lines), and the effective scale (solid lines). Thicker lines represent larger radii. The colours represent two different values of $N_{\rm tot}$ as noted in the legend. For a smaller number of stars, the photon number density is lower and hence the IC loss rate is lower. It therefore takes a longer time for the particles to lose energy in this way. This effect is evident at lower particle energies and smaller radii (as measured from the cluster centre) where IC dominates over SR due to the high value of n_ε there. At larger radii, the photon number density rapidly declines (leading to smaller $\dot{E}_{\rm IC}$ and longer $t_{\rm IC}$); thus SR dominates over IC.

In Figure 5.8, I plot $n_{\rm e}$ versus $E_{\rm e}$. At a fixed radius, the steady-state particle spectrum $n_{\rm e}$ is higher for a smaller value of $N_{\rm tot}$ (at low energies). This is because $\dot{E}_{\rm IC}$ is lower in this case and more particles survive. At large energies, this effect vanishes because SR dominates IC and SR is not a function of $N_{\rm tot}$. At larger radii, the effect of changing $N_{\rm tot}$ on the value of $n_{\rm e}$ is smaller, because n_ε and therefore $\dot{E}_{\rm IC}$ decreases rapidly with distance. Furthermore, the overall level of $n_{\rm e}$ decreases with radius since it represents a particle density, and the volume scales as $r_{\rm s}^3$. One can observe the same effect in Figure 5.9 for $n_{\rm e}$ versus $r_{\rm s}$: $n_{\rm e}$ decreases with radius due to an increase in volume; $n_{\rm e}$ decreases with energy due to the injection of fewer particles at higher energy; the effect of changing $N_{\rm tot}$ is only apparent at low particle energies, where IC dominates SR.

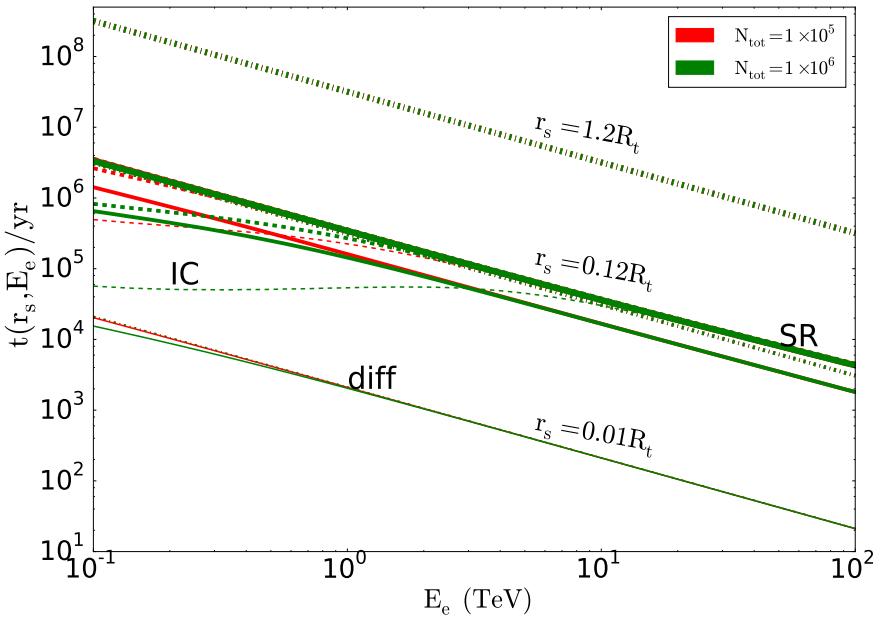

Figure 5.7: Timescales as a function of energy for diffusion (dash-dotted lines), radiation losses (dashed lines), and the effective scale (solid lines). Thicker lines represent larger radii. Dominating processes at different radii and particle energies are indicated in the graph. The colours represent different values of $N_{\rm tot}$ as noted in the legend.

Figure 5.10 shows the SED components in the case of changing $N_{\rm tot}$. When one increases $N_{\rm tot}$, there will be less energy available for SR and IC on the CMB, hence suppressing the low-energy IC and SR spectral fluxes. In Figure 5.11 I plot the relative contributions from a number of representative $r_{\rm s}$ to study the radial dependence of the cluster radiation for the case of changing $N_{\rm tot}$ assuming Bohm diffusion, $B = 5.0\,\mu$G, and $\Gamma = 2.0$, $\mathrm{Q}_0 = 6.33 \times 10^{33}\,\mathrm{erg}^{-1}\mathrm{s}^{-1}$, $d = 5.9\,$kpc and $N_{\rm tot} = 10^5$ or 10^6.

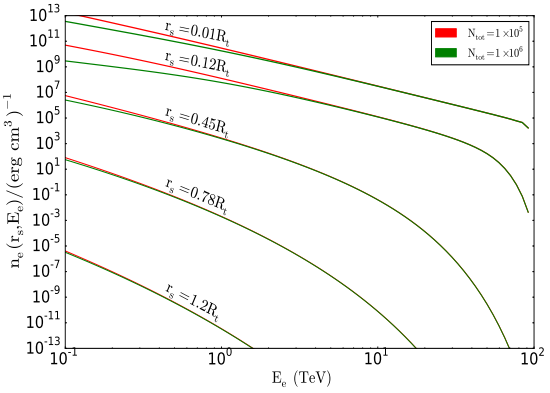

Figure 5.8: The steady-state particle spectrum as a function of energy E_e at different r_s assuming Bohm diffusion, $B = 5.0\,\mu$G, $\Gamma = 2.0$, $Q_0 = 6.33 \times 10^{33}\,\mathrm{erg^{-1}s^{-1}}$, $d = 5.9\,$kpc and $N_{tot} = 10^5$ or 10^6.

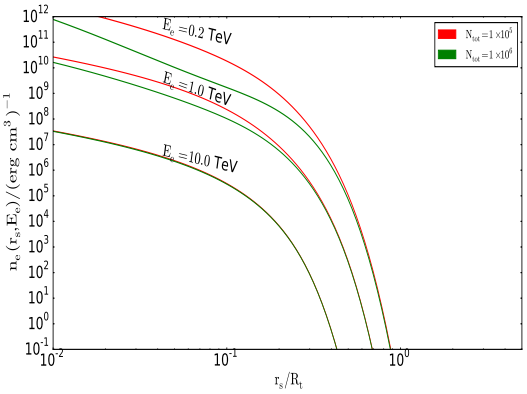

Figure 5.9: The steady-state particle spectrum as a function of radius r_s at different particle energies E_e assuming Bohm diffusion, $B = 5.0\,\mu$G, $\Gamma = 2.0$, $Q_0 = 6.33 \times 10^{33}\,\mathrm{erg^{-1}s^{-1}}$, $d = 5.9\,$kpc and $N_{tot} = 10^5$ or 10^6.

The dashed lines represent a larger N_{tot} and the solid lines indicate a smaller N_{tot}. The colours represent different values of radius. At small radii, the IC loss rate is lower for a smaller N_{tot} at the highest energies. One can see that at the lowest energies, the SR loss rate is lower for a higher number of stars at both smaller and larger radii since IC is boosted. As one goes out to larger radii, the effect of changing the N_{tot} is very small on the IC loss rate since n_ε decreases rapidly with r_s. (At $0.01R_t$, there is only a small effect since diffusion dominates.)

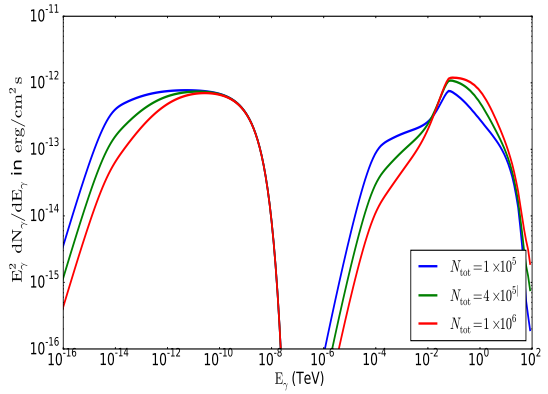

Figure 5.10: SED plot indicating the effect of changing the number of stars in the cluster on SR and IC components, assuming Bohm diffusion, $\Gamma = 2.0$ and $B = 5\ \mu$G.

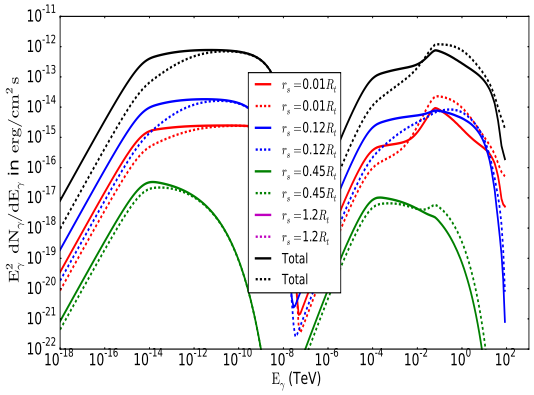

Figure 5.11: Spectra when changing the number of stars in the cluster for the case of Bohm diffusion, $B = 5\,\mu$G, $\Gamma = 2.0$, $Q_0 = 6.33 \times 10^{33}\,\mathrm{erg^{-1}s^{-1}}$, $d = 5.9\,$kpc, and $N_{tot} = 10^6$ indicated by dashed lines and $N_{tot} = 10^5$ represented by solid lines. The colours indicate representative radii in the cluster.

5.3 Changing the magnetic field

As above, Figure 5.12 presents different timescales versus particle energy. The colour indicates different magnetic fields in the cluster, and I use the following parameters: Bohm diffusion, $\Gamma = 2.0$, $Q_0 = 6.33 \times 10^{33}\,\mathrm{erg^{-1}s^{-1}}$, $d = 5.9\,\mathrm{kpc}$, $N_{\mathrm{tot}} = 4.6 \times 10^5$, and $B = 3\,\mu\mathrm{G}$, $10\,\mu\mathrm{G}$. I note that particles escape by diffusion at small radii (i.e., diffusion dominates at small radii). The energy dependence of the escape time is quite steep (i.e., $t_{\mathrm{esc}} \propto E_{\mathrm{e}}^{-1}$) and thus high-energy particles escape faster. It can be seen that for a lower B-field, the SR timescale is longer (i.e., $t_{\mathrm{SR}} = E_{\mathrm{e}}/\dot{E}_{\mathrm{SR}} \propto E_{\mathrm{e}}^{-1}B^{-2}$). Hence it takes a longer time for particles to lose energy due to SR in this case. IC dominates SR at low energies whilst radiation dominates diffusion at large r_{s} (same as Figure 5.7). An interesting regime change occurs between IC and SR domination around $\lesssim 1$ TeV for these two B-field strengths.

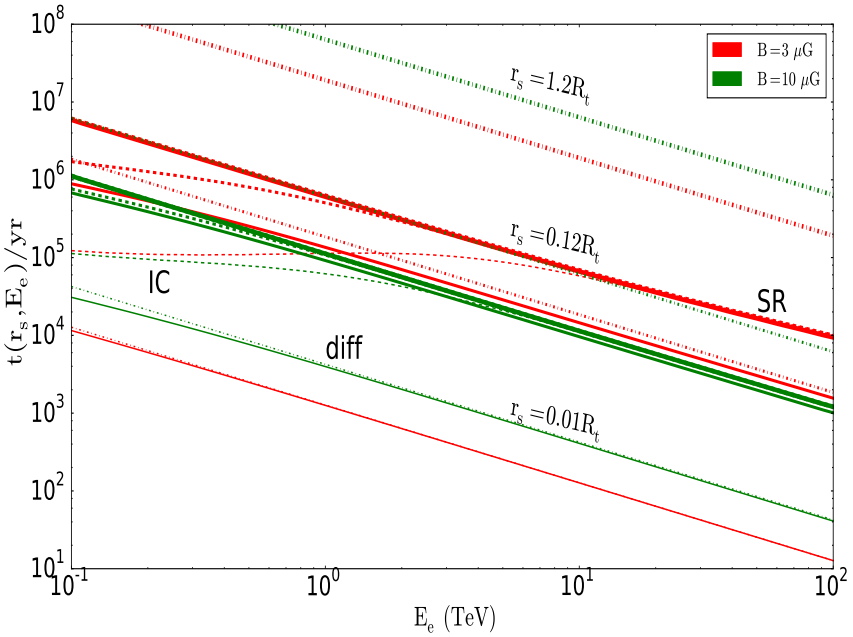

Figure 5.12: Loss timescales as a function of energy. The solid lines indicate effective timescales, the dashed lines represent radiation losses, and diffusion is shown by dash-dotted lines. The colours correspond to the magnetic fields shown in the legend.

In Figure 5.13, at fixed radius, n_{e} is higher for a lower magnetic field beyond $r_{\mathrm{s}} \gtrsim 0.05R_{\mathrm{t}}$. This is because $\dot{E}_{\mathrm{SR}}$ is lower in this case and more particles survive. There is a cutoff at higher energies due to SR. As before, the cutoff becomes increasingly lower at larger radii. I note that the particle spectrum is very small at larger radii for $B = 10\,\mu\mathrm{G}$ (i.e., the green line for a larger B-field is very

low at larger radii, i.e., $r_s = 1.2R_t$ and $r_s = 0.78R_t$, thus these lines are not visible). In Figure 5.14, the effect of changing the magnetic field on the value of n_e is very small at smaller radii because IC dominates there. However, at large r_s, it is evident that a larger B-field leads to a substantially lower cutoff energy due to increased $\dot{E}_{SR}$ in this case.

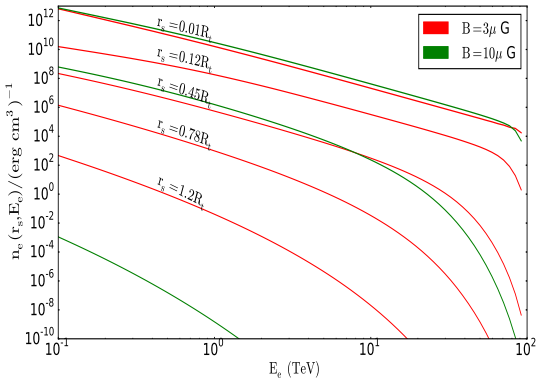

Figure 5.13: Steady-state particle spectrum as a function of energy at different magnetic fields $B = 3\,\mu G$, and $10\,\mu G$, assuming Bohm diffusion, $\Gamma = 2.0$, $Q_0 = 6.33 \times 10^{33}\,\mathrm{erg^{-1}s^{-1}}$, $d = 5.9\,\mathrm{kpc}$, and $N_{\mathrm{tot}} = 4.6 \times 10^5$. The colours correspond to the magnetic field in the cluster, as shown in the legend.

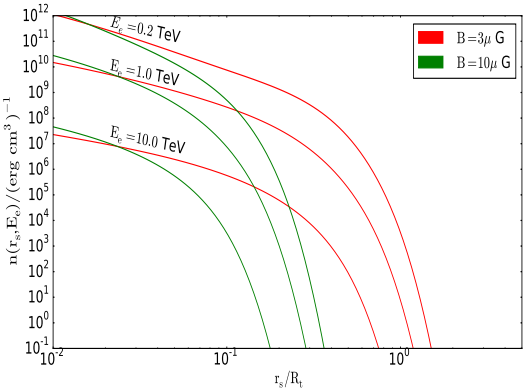

Figure 5.14: Steady-state particle spectrum for different magnetic fields $B = 3\,\mu G$, and $10\,\mu G$, assuming Bohm diffusion, $\Gamma = 2.0$, $Q_0 = 6.33 \times 10^{33}\,\mathrm{erg^{-1}s^{-1}}$, $d = 5.9\,\mathrm{kpc}$, and $N_{\mathrm{tot}} = 4.6 \times 10^5$. The colours correspond to the magnetic field in the cluster, as shown in the legend.

Figure 5.15 shows the SED components of a cluster in the case of Bohm diffusion, $\Gamma = 2.0$, $B = 1\ \mu$G, $3\ \mu$G, $5\ \mu$G, $Q_0 = 6.33 \times 10^{33}\,\mathrm{erg^{-1}s^{-1}}, d = 5.9\,\mathrm{kpc}$, and $N_{\mathrm{tot}} = 4.6 \times 10^5$. The SR loss rate strongly depends on the magnetic field strength. One can see that if the magnetic field is increased from 1μG to 5μG, the SR increases rapidly because $\dot{E}_{SR} \propto E_e^2 B^2$. Therefore, higher-energy particles lose more energy leaving fewer particles available at higher energies to radiate IC. Thus the IC flux is lower for higher magnetic fields. In Figure 5.16, I study the radial dependence of the cluster radiation for Bohm diffusion, $\Gamma = 2.0$, $B = 3.0\,\mu$G, $10\,\mu$G, $Q_0 = 6.33 \times 10^{33}, d = 5.9\,\mathrm{kpc}$, and $N_{\mathrm{tot}} = 4.6 \times 10^5$. The colours indicate different radii, and the higher B-field is shown by dashed lines whilst the lower B-field is shown by solid lines. At small radii, both SR and IC emission increase with an increase in B-field because of slower diffusion in this case, leading to particles spending a longer time there. For different diffusion coefficients, one has different source sizes. If particles moves faster then the source becomes bigger. If they move slower, the source becomes smaller, thus a higher B-field leads to more losses at small r_s, and a compact source is predicted. This explains the line swap in the graph, i.e., the non-monotonic behaviour of lines as r_s is increased (cf. Figure 6 from Kopp et al. 2013). It can be seen that both IC and SR fluxes

decrease with an increase in B-field at large radii.

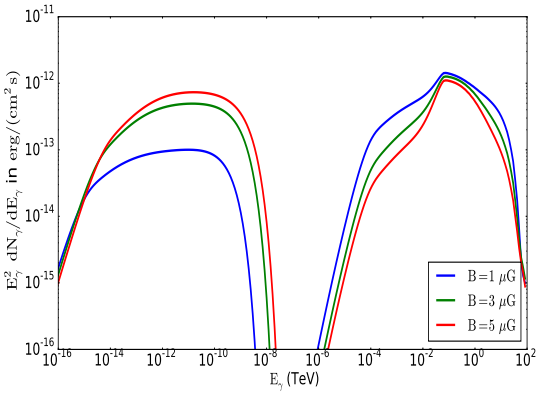

Figure 5.15: SED plot indicating the effect of changing the magnetic field in the cluster on SR and IC components, assuming Bohm diffusion, and $\Gamma = 2.0$, $Q_0 = 6.33 \times 10^{33}\,\mathrm{erg^{-1}s^{-1}}$,$d = 5.9\,\mathrm{kpc}$, and $N_{\mathrm{tot}} = 4.6 \times 10^5$.

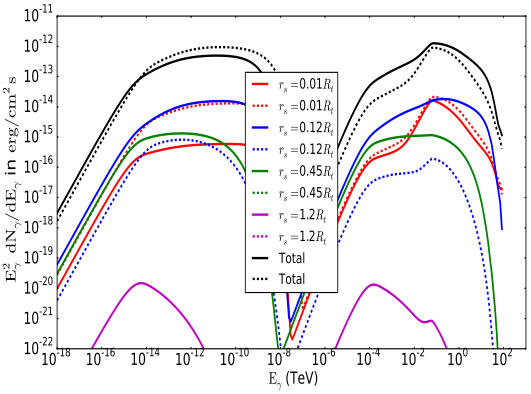

Figure 5.16: Spectra for different magnetic fields in the cluster for the case of Bohm diffusion, $\Gamma = 2.0$, $Q_0 = 6.33 \times 10^{33}\,\mathrm{erg^{-1}s^{-1}}$,$d = 5.9\,\mathrm{kpc}$, and $N_{\mathrm{tot}} = 4.6 \times 10^5$, and $B = 10\,\mu$G indicated by dashed lines and $B = 3\,\mu$G represented by solid lines.

5.4 Changing electron source term: Spectral index Γ

I note that changing Γ does not change the timescales versus E_{e} or r_{s}, however it does change the source term (see Equations [4.13] and [4.14], where I change Γ and keep L_{e} constant) (see Equation 4.14 for evaluation of L_{e}). I used $N_{\mathrm{MSPs}} = 25$ for most of GCs, $\eta = 0.1$ and $\langle \dot{E}_{\mathrm{rot}} \rangle = 2 \times 10^{34}\,\mathrm{erg\,s^{-1}}$. Figure 5.17 shows the steady-state particle spectrum as a function of energy for different spectral indices Γ as denoted by the colours in the legend. I note that, at a fixed radius, the steady-state particle spectrum n_{e} is higher for a hard spectrum at large radii and energies. However, close to the GC core the low-energy tail of the spectrum is slightly higher for a softer spectral index because the L_{e} is kept constant (same total power in particles). At low energies and smaller radii the effect of changing the Γ is smaller. Similarly, in Figure 5.18 the particle spectrum slope decreases (becomes softer) at larger radii. This is because the particles lose energy due to radiation as they diffuse through the cluster. There is a greater effect at larger E_{e} in Figures 5.17 and 5.18.

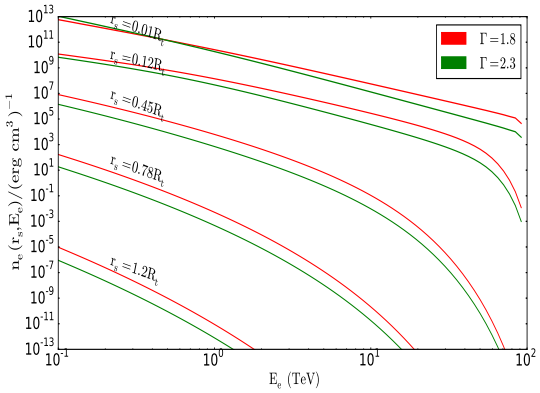

Figure 5.17: Steady-state particle spectrum as a function of energy at different radii r_s, for Bohm diffusion, $B = 5\,\mu$G, and $\Gamma = 1.8$ and 2.3. The colours indicate different spectral indices, shown in the legend.

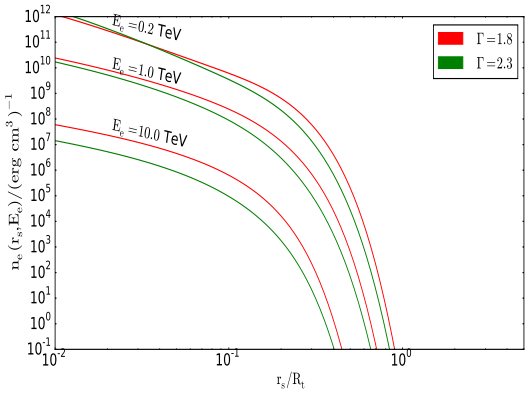

Figure 5.18: Steady-state particle spectrum as a function of radius at different r, for Bohm diffusion, $B = 5\,\mu$G, and $\Gamma = 1.8$ and 2.3. The colours indicate different spectral indices, shown in the legend.

Figure 5.19 shows the SED plot in the case of changing the spectral index. The colours represent different values of spectral index as indicated in the legend. I used Bohm diffusion, $B = 5\,\mu G$, $Q_0 = 6.33 \times 10^{33}\mathrm{erg}^{-1}\mathrm{s}^{-1}$, $d = 5.9\,\mathrm{kpc}$, and $N_{\mathrm{tot}} = 4.6 \times 10^5$. Both SR and IC decline for a soft Γ and increase for a harder injection spectrum (more high-energy particles are injected into the GC). In Figure 5.20 I study the radial dependence of the cluster radiation when changing the spectral index. I used Bohm diffusion, $B = 5.0\,\mu G$, $Q_0 = 6.33 \times 10^{33}\mathrm{erg}^{-1}\mathrm{s}^{-1}$, $d = 5.9\,\mathrm{kpc}$, and $N_{\mathrm{tot}} = 4.6 \times 10^5$. The solid lines represent $\Gamma = 1.8$ and the dashed lines represent $\Gamma = 2.3$. The colours again indicate different values of radius. At large radii, both SR and IC flux decrease for a softer Γ. At smaller radii, the SR flux increases for softer Γ at the lowest values of particle energy due to the normalisation of Q_0 and a constant L_{e}.

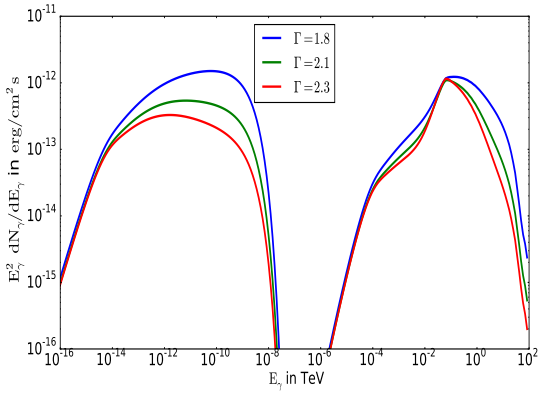

Figure 5.19: SED plot indicating the effect of changing the spectral index on SR and IC components, assuming Bohm diffusion, $B = 5\,\mu$G, $Q_0 = 6.33 \times 10^{33}\mathrm{erg}^{-1}\mathrm{s}^{-1}, d = 5.9\,$kpc, and $N_{\rm tot} = 4.6 \times 10^5$.

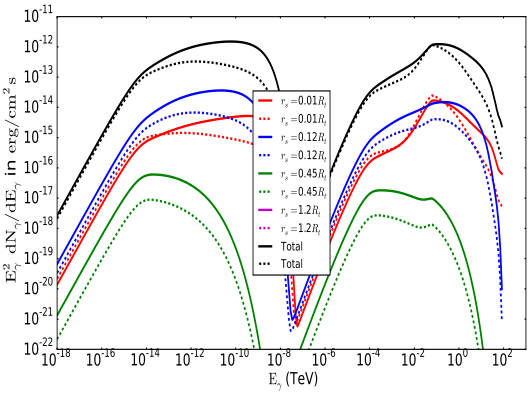

Figure 5.20: Spectra when changing the spectral index for the case of Bohm diffusion, $B = 5\,\mu$G, $Q_0 = 6.33 \times 10^{33}\mathrm{erg}^{-1}\mathrm{s}^{-1}, d = 5.9\,$kpc, and $N_{\rm tot} = 4.6 \times 10^5$. $\Gamma = 2.3$ is indicated by dashed lines and $\Gamma = 1.8$ is represented by solid lines.

The IC flux increases for a harder spectrum at the highest energies. I note that energy loss rates are very small at larger radii (i.e., the magenta lines are very low at larger radii are thus not visible).

5.5 Changing electron source term: Normalisation Q_0

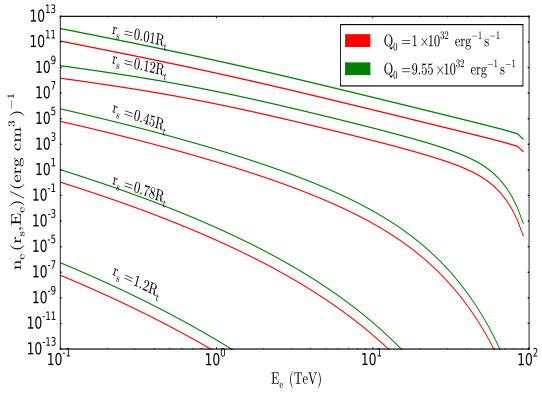

Figure 5.21: Steady-state particle spectrum as a function of energy for different Q_0, assuming Bohm diffusion, $B = 5\,\mu$G, $\Gamma = 2.0, d = 5.9\,$kpc, and $N_{\rm tot} = 4.6 \times 10^5$. The colours correspond to the source term normalisation shown in the legend.

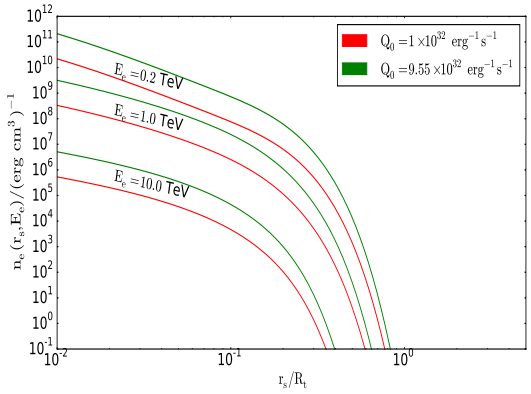

Figure 5.22: Steady-state particle spectrum as a function of radius for different Q_0, assuming Bohm diffusion, $B = 5\,\mu$G, $\Gamma = 2.0, d = 5.9\,$kpc, and $N_{\rm tot} = 4.6 \times 10^5$. The colours correspond to the source term normalisation shown in the legend.

Changing the source term does not affect the timescales versus $E_{\rm e}$ or $r_{\rm s}$. In Figure 5.21 I plot the steady-state particle spectrum versus energy. At fixed radius, $n_{\rm e}$ is higher for larger source terms

(injection rates) since n_e scales linearly with Q_0. There is a cutoff at higher energies due to SR. As before, one can see that the overall level of n_e decreases with radius due to an increase volume. In Figure 5.22 I plot the steady-state particle spectrum as a function of radius for different Q_0, assuming Bohm diffusion, $B = 5\,\mu$G, $\Gamma = 2.0, d = 5.9\,$kpc, and $N_{tot} = 4.6 \times 10^5$. Figure 5.23 shows the effect of changing the source term (particle injection). If more particles are injected into the cluster, both SR and IC fluxes will increase. A change in the source strength value does not influence the shape of the SED but simply increases or decreases the amount of the particles in the cluster, and thus the level of radiation received from the cluster.

Figure 5.24 shows the radial dependence of the cluster radiation when changing the number of particles injected into the cluster. The colours represent different radii. I considered Bohm diffusion and $B = 5\,\mu$G. The dashed lines indicate increased particle injection whilst the solid lines indicate reduced particle injection in the cluster. One can see that SR and IC fluxes increase with an increase in particle injection, at all radii. Again, the energy loss rates are very small at larger radii (i.e., the magenta lines are very low at larger radii and are thus not visible).

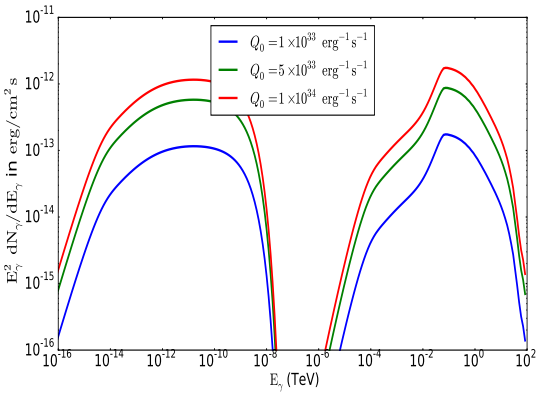

Figure 5.23: SED for a cluster with a change in the source term normalisation (change in Q_0), assuming Bohm diffusion, $B = 5\,\mu$G, $\Gamma = 2.0, d = 5.9\,$kpc, and $N_{tot} = 4.6 \times 10^5$.

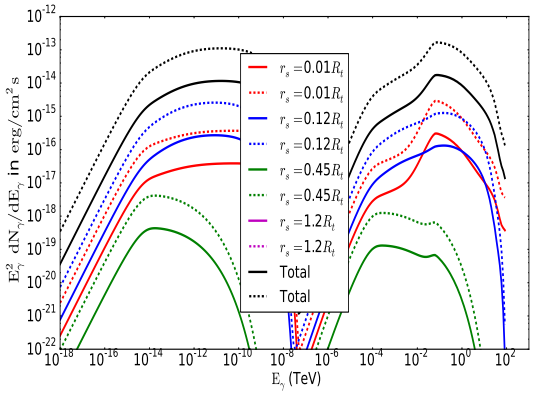

Figure 5.24: Spectra for changing particle source term normalisation in the cluster for the case of Bohm diffusion,$B = 5\,\mu$G, $\Gamma = 2.0, d = 5.9\,$kpc, and $N_{tot} = 4.6 \times 10^5$. $Q_0 = 9.55 \times 10^{32}\,$erg^{-1}s^{-1} is indicated by dashed lines and $Q_0 = 1 \times 10^{32}\,$erg^{-1}s^{-1} is represented by solid lines.

5.6 Changing the source distance d

Changing the distance to the cluster changes the physical size of the cluster, as I keep the angular size constant (e.g., the core radius $r_c = \theta_c d$, with θ_c the 'angular radius' of the core). Figure 5.25

shows radiative loss timescales as a function of particle energy for different distances, as indicated by the coloured lines and the legend. The line thickness indicates different radii, dashed lines represent timecales for radiation losses, dash-dotted lines represent diffusion timescales, and the solid lines indicate the effective timescales. As found previously, at small radii particles escape by diffusion, while radiation losses dominate at large radii. At low energies, IC dominates and SR dominates at high energies. One can see that, for a smaller distance (physically smaller cluster size), the IC timescale is lower (i.e., for a smaller d, the volume is smaller and thus the energy density becomes larger, leading to an increased IC loss rate) and thus it takes a shorter time for the particles to lose energy. I note that high-energy particles diffuse and radiate faster than low-energy particles. Furthermore, since $\tau_{\rm diff} \propto r_{\rm s}^2 \propto d^2$, the distance decreases particles escape faster from a particular zone, leading to lower diffusion timescales. SR is not influenced by a change in distance, because I assumed a constant B-field everywhere in the cluster. In Figure 5.26 one can see that the steady-state particle spectrum (per volume) is higher for a smaller distance than for a larger one due to a decrease in volume. At smaller radii, diffusion dominates and radiation dominates over diffusion at larger radii.

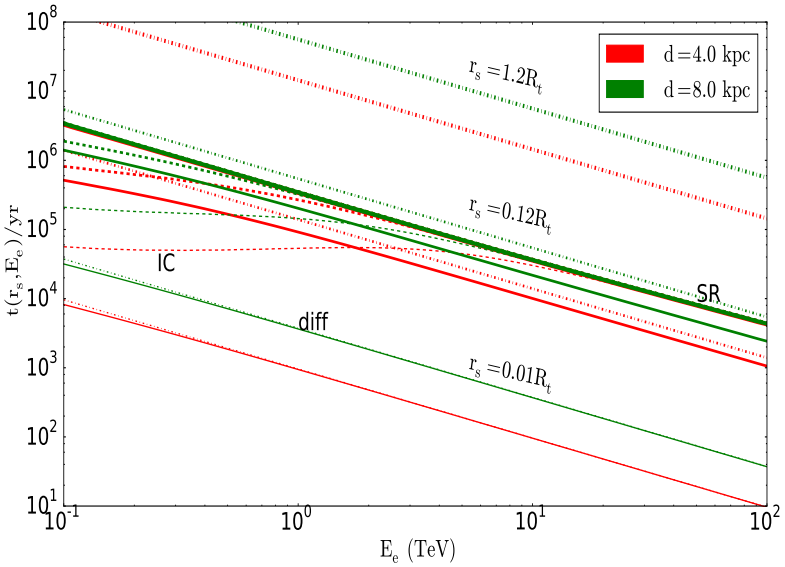

Figure 5.25: Different timescales as a function of energy for different distances.

In Figure 5.27 the effect of changing the distance to the cluster is lower at small radii. We observe the same effect in Figure 5.26. I used the number of zones but the actual $R_{\rm t}$ might change because of change in distance, thus zone radii change. Physically, the green lines indicate a larger cluster than

the red lines. Thus particles take longer to escape and therefore lose more energy while diffusing through the cluster. This explains the cutoff which is lower for larger d. The particle spectrum is very small at larger radii for $d = 8.0\,\mathrm{kpc}$, i.e., the green line for a larger distance (larger source size) is very low at larger radii, and is thus not visible.

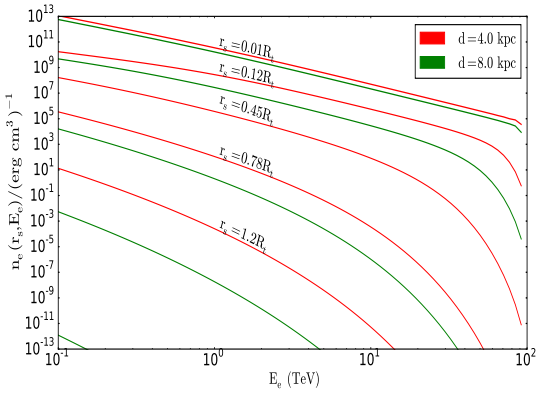

Figure 5.26: Steady-state particle spectrum as a function of energy for different distances (see legend).

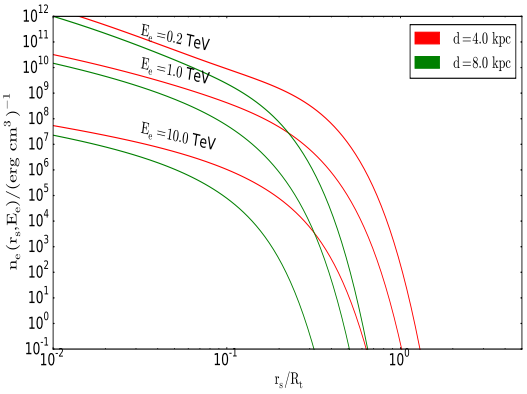

Figure 5.27: Steady-state particle spectrum as a function of radius for different distances (see legend).

Figure 5.28 shows the SED components of a cluster in the case of Bohm diffusion, $\Gamma = 2.0$, $B = 5\mu\mathrm{G}$, $\mathrm{Q}_0 = 6.33 \times 10^{33}\mathrm{erg}^{-1}\mathrm{s}^{-1}$, $N_{\mathrm{tot}} = 4.6 \times 10^5$ and different values of source distance as indicated in the legend. I note that as the distance to the cluster increases from 2 kpc, to 8 kpc, both the SR and IC fluxes decrease. Particles diffusing through clusters that are more distant (larger physical size source) tend to lose more energy than those that are nearer in both SR and IC. Fluxes furthermore scale as $1/d^2$.

In Figure 5.29 I plot IC and SR flux versus energy to study the radial dependence of the cluster radiation upon changing the distance to the cluster. The dashed lines indicate $d = 8.0$ kpc and the solid lines represent $d = 4$ kpc. The colours indicate different values of radius. I again used Bohm diffusion, $B = 5\,\mu\mathrm{G}$, $\Gamma = 2.0$. I note that the IC and SR fluxes decrease with an increase in distance at all radii.

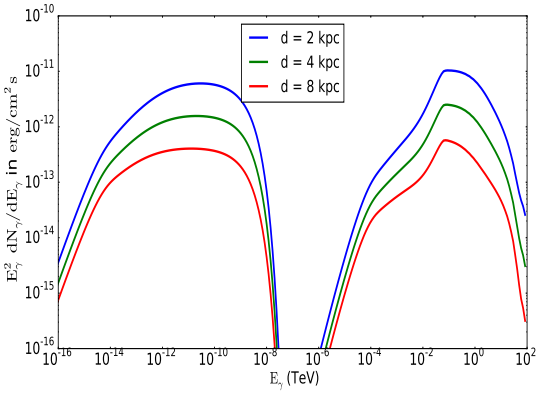

Figure 5.28: SED plot showing the effect of changing the distance to the cluster on SR and IC compnents.

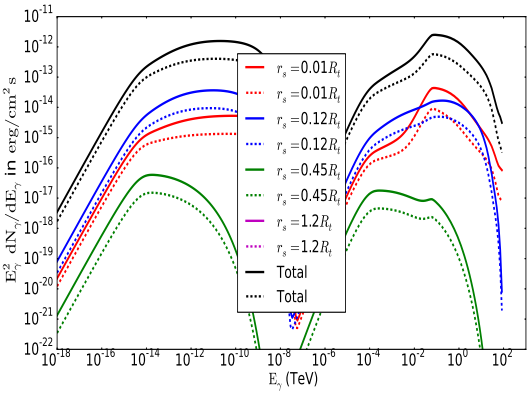

Figure 5.29: Spectra when changing the distance to the cluster for the case of Bohm diffusion $B = 5\,\mu$G, $\Gamma = 2.0$, and $d = 8.0\,$kpc indicated by dashed lines and $d = 4.0\,$kpc represented by solid lines.

5.7 Changing the spatial diffusion coefficient (κ_0)

In Figure 5.30 I plot the timescale graph for diffusion (dash-dotted lines), radiation losses (dashed lines), and effective timescale (solid lines). The colours represent different diffusion coefficients as shown in the legend. I note that IC still dominates at low energies and SR dominates at higher energies. High-energy particles diffuse faster than low-energy particles. I used two diffusion coefficients, Bohm diffusion at $\sim 6 \times 10^{24}\,\mathrm{cm}^2/\mathrm{s} \sim 2 \times 10^{-5}\mathrm{kpc}^2/\mathrm{Myr}$ that goes like $\kappa \propto E^1$, and $\kappa_0 \sim 2 \times 10^{25}\,\mathrm{cm}^2/\mathrm{s} \sim 7 \times 10^{-5}\mathrm{kpc}^2/\mathrm{Myr}$ that goes like $\kappa \propto E^{0.6}$. The Bohm diffusion timescale has a slope of -1 whilst in the second case, τ_{diff} has a slope of -0.6. The values of these diffusion coefficients are evaluated at 1 TeV. The Bohm diffusion timescale is larger at $E_\mathrm{e} \lesssim 10\,\mathrm{TeV}$ (low energies) and smaller at $E_\mathrm{e} \gtrsim 10\,\mathrm{TeV}$ (higher energies).

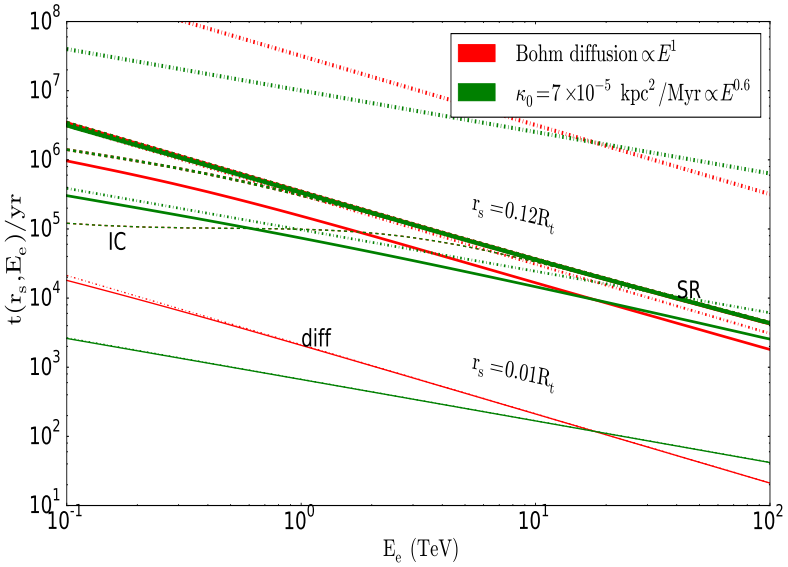

Figure 5.30: Timescales as a function of energy for different diffusion coefficients.

In Figure 5.31, at intermediate radius, n_e is higher for the second lower κ value for the diffusion coefficient at low energies. For particle energies around 10 TeV and low radius, the effect of changing the diffusion coefficient on the value of n_e is very small. One can observe the same effect in Figure 5.32: n_e decreases with a decrease in the diffusion coefficient (hence the residence time of particles is increased for a particular zone). At higher energies, diffusion does not influence the particle spectrum so much as it does at low energies, since SR dominates there.

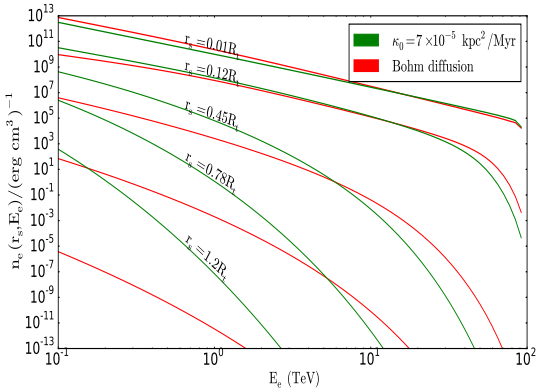

Figure 5.31: Steady-state particle spectrum as a function of energy for different diffusion coefficients.

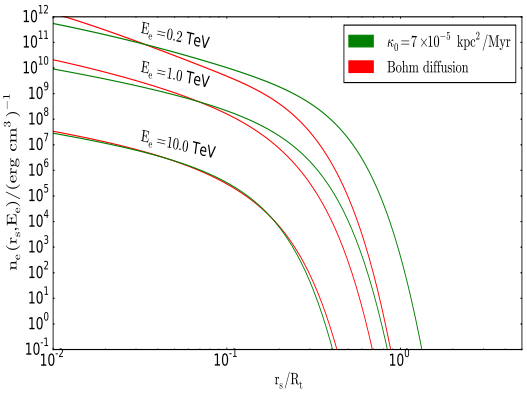

Figure 5.32: Steady-state particle spectrum as a function of radius for different diffusion coefficients.

From Figure 5.33 it can be seen that the SR flux scales with the spatial diffusion coefficient at low

energies (since B is not a function of r but n_ε is). The IC loss rate is lower for a larger diffusion coefficient at the highest energies because particles escape before radiating.

In Figure 5.34 I plot the spectra for changing diffusion coefficients in the cluster for the case of $B = 5\,\mu$G, $\Gamma = 2.0$, Bohm diffusion indicated by dashed lines and $\kappa_0 = 0.7 \times 10^{-4}\,\mathrm{kpc}^2/\mathrm{Myr}$ represented by solid lines. Again, coloured lines show different values of cluster radii. At large radii, the SR loss rate increases with an increase in diffusion coefficients at the lowest particle energies. At small radii, the SR energy loss rate decreases with an increase in diffusion coefficient at low energies. I note that the IC loss rate decreases with an increase in diffusion coefficient at the highest energies.

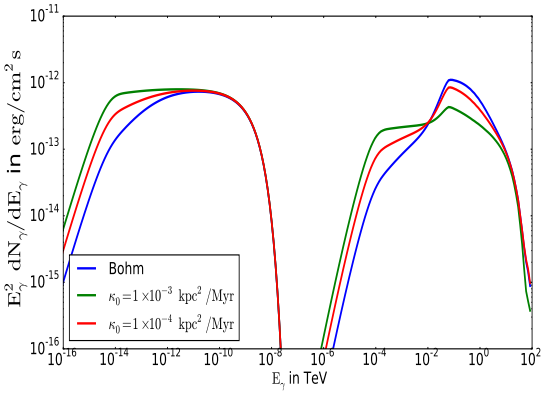

Figure 5.33: SED plot for a cluster with a change in spatial diffusion coefficient.

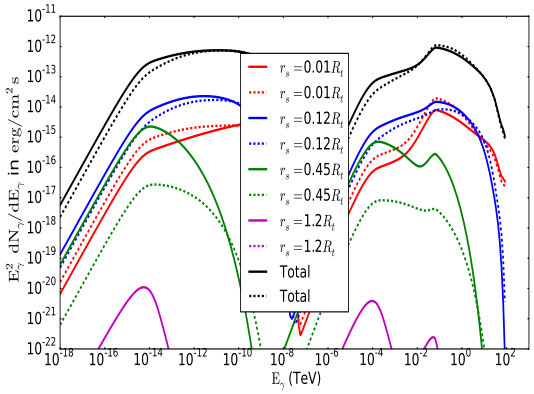

Figure 5.34: Spectra for changing diffusion coefficients in the cluster for the case of $B = 5\,\mu$G, $\Gamma = 2.0$, Bohm diffusion indicated by dashed lines and $\kappa_0 = 0.7 \times 10^{-4}\,\mathrm{kpc}^2/\mathrm{Myr}$ represented by solid lines.

5.8 Summary

In this chapter, I discussed the effects of changing the number of stars (N_{tot}) in the cluster, the magnetic field (B) in the cluster, the spectral index of the injected spectrum (Γ), the normalisation of this source term (Q_0), the distance to the cluster(d) (i.e., the size of the cluster), and the spatial diffusion coefficient (κ_0 andδ) on the energy loss and diffusion timescales to show where radiation dominates, and in which regions particle escape dominates. I also showed the effect on the steady-state particle spectrum as well as the radiated SED.

Table 5.2 summarises the effect of increasing the model parameters on the particle spectrum and in Table 5.3 I summarise the effect on the SED plot when increasing the model parameters listed

in the tables.

Model parameters	**Close to the core**		$r \approx R_{\mathrm{t}}$	
	Low energies	**High energies**	**Low energies**	**High energies**
Number of stars (N_{tot})	-	=	=	=
Magnetic field (B)	=	$\approx$	-	-
Spectral index (Γ)	$\approx$	-	-	-
Electron source term (Q_0)	+	+	+	+
Distance (d)	-	-	-	-
Diffusion coefficient (κ_0)	$\approx$	=	-	-

Table 5.2: In this table I described the effect of increasing model parameters on the steady-state particle spectrum.

Model parameters	**Close to the core**			$r \approx R_{\mathbf{t}}$		
	Radio	**X-rays**	**γ-rays**	**Radio**	**X-rays**	**γ-rays**
Number of stars (N_{tot})	-	=	+	$\approx$	$\approx$	$\approx$
Magnetic field (B)	+	+	$\approx$	-	-	-
Spectral index (Γ)	$\approx$	-	-	-	-	-
Electron source term (Q_0)	+	+	+	+	+	+
Distance (d)	-	-	-	-	-	-
Diffusion coefficient (κ_0)	+	+	$\approx$	-	-	$\approx$

Table 5.3: In this table I described the effect of increasing model parameters on the SED plot.

Chapter 6

Spectral Modelling of Globular Clusters

In the previous chapter I performed a parameter study to investigate the behaviour of the model. In this chapter I will list some structural parameters of the analysed GCs (Chapter 3) and discuss the parameters that I have constrained using multi-wavelength data for some of the sources. Lastly, I will list the five most promising GCs for both H.E.S.S. and CTA according to their predicted VHE flux.

6.1 Structural and Other Characteristics of Selected GCs

For the 16 selected GCs for which I analysed data in Chapter 3, I now list some structural parameters that I used to model the SED of the 16 GCs (Figure 6.4). Table 6.1 shows the core ($R_{\rm c}$), tidal ($R_{\rm t}$) and half-mass ($R_{\rm h}$) radius (Harris 1996, 2010) and the number of stars ($N_{\rm tot}$) estimated from $N_{\rm tot} = 10^{0.4(4.79-M_V)}$ hosted by each cluster, where M_V is the integrated absolute magnitude (Lang, 1992); also listed is the estimated number of MSPs in each GC (Abdo et al., 2010; Venter & Kopp, 2015) and the GC's distances from the Sun (Harris, 2010).

GC name	R_c(pc)	R_{hm} (pc)	R_t (pc)	Estimated $N_{tot}/10^5$	N_{MSP}	d (kpc)
NGC 104	0.47	4.1	56.1	4.57	> 33	4.5
NGC 6388	0.16	0.68	8.13	5.81	100	9.9
NGC 7078	0.18	1.31	28.1	4.13	25	10.4
Terzan 6	0.07	0.58	22.8	0.29	25	6.8
Terzan 10	1.18	2.03	6.62	0.30	25	5.8
NGC 6715	0.12	1.07	9.78	4.79	25	26.5
NGC 362	0.24	1.07	21.1	1.58	25	8.6
Pal 6	0.86	1.57	10.9	0.31	25	5.8
NGC 6256	0.03	1.13	9.94	0.21	25	10.3
Djorg 2	0.43	1.31	13.8	0.51	25	6.3
NGC 6749	0.81	1.44	6.82	1.78	25	7.9
NGC 6144	1.23	2.13	43.5	0.48	25	8.9
NGC 288	1.77	2.92	16.9	0.32	25	8.9
HP 1	0.04	4.06	10.8	0.48	25	8.2
Terzan 9	0.04	1.02	10.8	0.02	25	7.1
Terzan 5	0.21	0.94	17.4	0.77	> 34	6.9

Table 6.1: Structural and other parameters of 16 clusters used in this study. The columns are: cluster identification; core radius in parsec; half-mass radius in parsec; tidal radius in parsec; estimated number of stars; estimated number of MSPs, and distances in kiloparsec.

6.2 Constraining Parameters using X-ray and γ-ray Data

I used diffuse X-ray and γ-ray observations to constrain the cluster parameters for three sources (i.e., Terzan 5, 47 Tucanae, and NGC 6388) so as not to violate the data. I first present the results for Terzan 5. The γ-ray (Abramowski et al., 2011) and X-ray (Eger et al., 2010) data are plotted in Figure 6.1. Our model cannot reproduce the flat slope of the X-ray data. Hence, one might have to postulate a new radiation component (Venter et al., in preparation) to explain these data. I therefore treat the X-ray data as upper limits and therefore my predicted component must be below these. I am not fitting the data using rigorous statistical tests, but I am trying to find sample parameters so that the predicted SR component is not in conflict with the X-ray "upper limits"

while still fitting the γ-ray data. Figure 6.1 shows the predicted differential SED components of Terzan 5 indicating the predicted SR (integrated between $55' < r_s < 174'$[1] corresponding to the X-ray data, Eger et al. 2010) and IC (integrated over all r_s) components using a combination of parameters so as not to violate the *Chandra* and H.E.S.S. data. I show the blue component as an example of a parameter combinations which violates data. On the other hand, both the green and the red components satisfy the constrained data. The following parameter values are used as sample parameters so that the predicted SR component satisfy the X-ray while fitting the γ-ray data for Terzan 5.

Line colours	κ (kpc^2/Myr)	B (μG)	Γ	Q_0 (erg^{-1}s^{-1})	d (kpc)	$N_{\rm tot}$	$\gamma_{\rm max}$ (TeV)
Blue	Bohm diffusion	5	2.0	6.33×10^{33}	5.9	4.6×10^5	100
Red	Bohm diffusion	1	1.8	6.33×10^{33}	5.9	8.0×10^5	20
Green	0.7×10^{-4}	2	2.0	9.84×10^{33}	5.9	8.0×10^5	50

Table 6.2: In this table I list the line colours as shown in Figure 6.1 and the parameters that I chose so that the SR component is not in conflict with the X-ray upper limits while fitting the γ-ray data.

Other combinations of parameters also exist that can give the similar fits. One should be able to break this degeneracy by adding more data in future.

[1] In Figures 6.1, 6.2, and 6.3 the dash-dotted lines represent the inner part of the source, and the solid lines indicate the whole source visible in γ-rays. The FoV of the γ-ray telescope is large, and therefore one can see the whole source, whilst only a small part of the source is seen in X-rays since the FoV of *Chandra* is small.

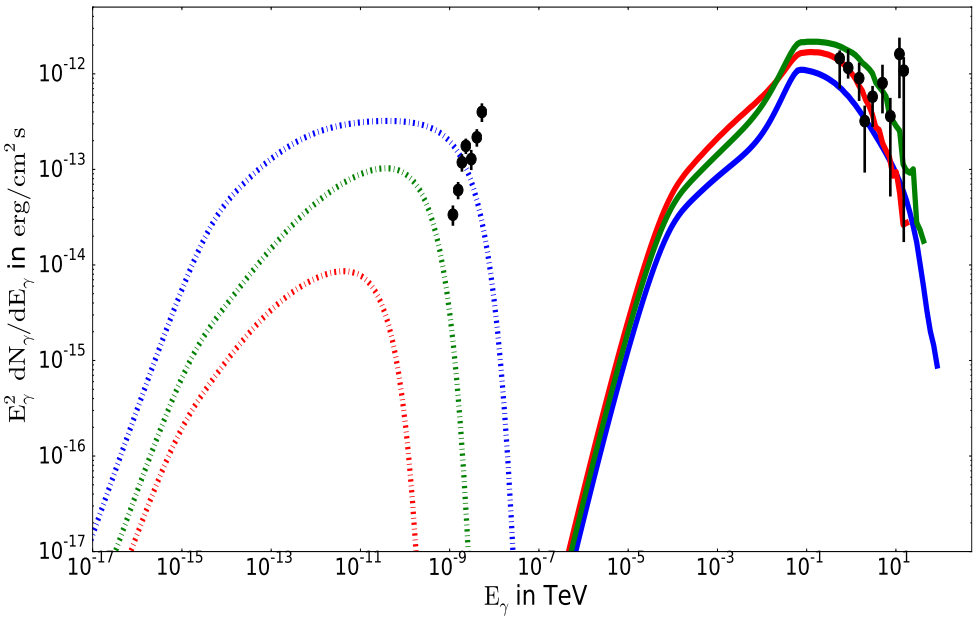

Figure 6.1: The SED for Terzan 5 indicating the SR (integrated between $55' < r_s < 174'$, the dash-dotted lines) for the inner part of the source and IC (integrated over all r_s, solid lines) components for different combinations of parameters, as well as *Chandra*(Eger et al., 2010) and H.E.S.S. (Abramowski et al., 2011) data.

Thus one can actually allow $\gamma_{\rm max}$ to be $\sim$ 30 TeV to 100 TeV and the B-field can be $\sim$ 1 μG to 4 μG, depending on other parameters. We could not constrain the radio and optical part of the spectrum. There might be some radio data available (Clapson et al., 2011), but it is not certain that these data are associated with the diffuse SR component that we predict. In this work I mainly focused on γ-ray and X-ray data. The predicted optical diffuse flux level is so small and that makes it extremely difficult to find upper limits or data that would at all be constraining, given the number of optical sources ($N_{\rm tot}$) that dominate the radiation in this band.

Similarly, I present results for 47 Tucanae and NGC 6388 using diffuse X-ray (Wu et al., 2014; Eger & Domainko, 2012) and H.E.S.S. upper limits Abramowski et al. (2013) to constrain cluster parameters. There are no VHE γ-ray data available for 47 Tucanae and NGC 6388, as these two sources are not yet detected by H.E.S.S. (We don't model the *Fermi* component in this model.)

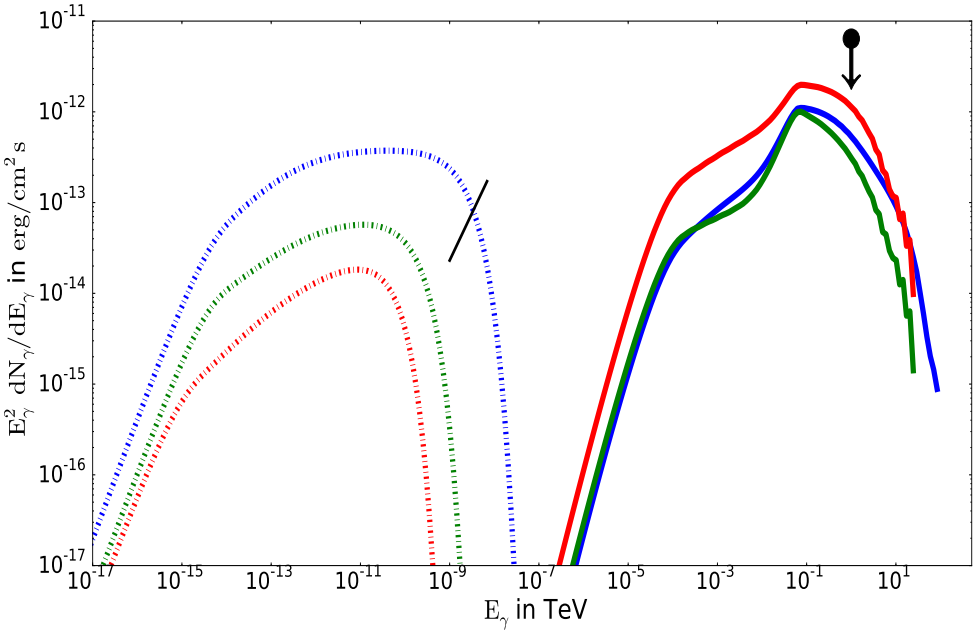

Figure 6.2: The predicted SED for 47 Tucanae indicating the SR (integrated between $0.72' < r_s < 3.835'$ the dash-dotted lines), and IC (integrated over all r_s, solid lines) components for different combinations of parameters, as well as *Chandra* and H.E.S.S. data. The power-law in the SR component represent the X-ray data whilst the dot-arrow in the IC component represent the H.E.S.S. upper limit.

Figure 6.2 shows the predicted SED for 47 Tucanae indicating the predicted SR (integrated between $0.72' < r_s < 3.835'$) and IC (integrated over all r_s) components using several combinations of parameters. The blue line i.e., the reference model violates X-ray data (treated as "upper limit") but for a distance of $d = 4.5$ kpc for 47 Tucanae. The red and green lines do not violet the X-ray upper limits. The following parameter values are used as sample parameters so that the predicted SR component is not in conflict with the X-ray upper limits while fitting the γ-ray upper limit for 47 Tucanae.

Line colours	κ (kpc^2/Myr)	B (μG)	Γ	Q_0 (erg^{-1}s^{-1})	d (kpc)	$N_{\rm tot}$	$\gamma_{\rm max}$ (TeV)
Blue	Bohm diffusion	5	2.0	6.33×10^{33}	4.5	4.6×10^5	100
Red	1.1×10^{-4}	1	2.0	9.55×10^{33}	4.5	4.6×10^5	100
Green	1.1×10^{-4}	4	2.3	3.18×10^{33}	4.5	4.6×10^5	30

Table 6.3: In this table I list the line colours as shown in Figure 6.2 and the parameters that chose so that the SR componet is not in conflict with the X-ray upper limits while fitting the γ-ray data.

Thus changing different combinations of parameters will lead to the model satisfying the data constraint.

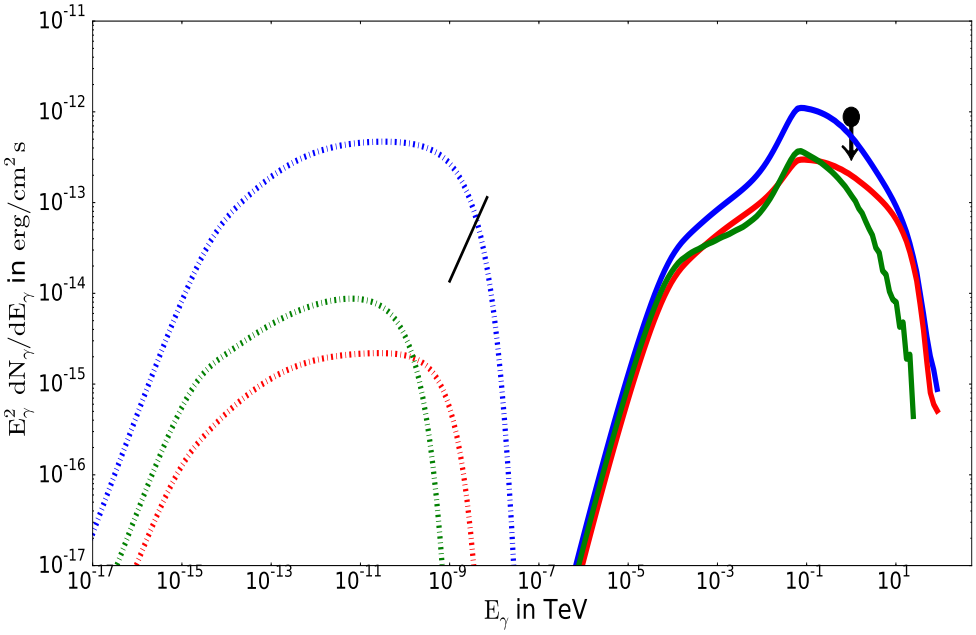

Figure 6.3: The predicted SED for NGC 6388 indicating the SR (integrated between $25' < r_s < 139'$, the dash-dotted lines) and IC (integrated over all r_s, solid lines) components for different combinations of parameters. The power-law in the SR component represent the X-ray data whilst the dot-arrow in the IC component represent the H.E.S.S. upper limit.

Figure 6.3 shows the predicted SED for NGC 6388 indicating the predicted SR (integrated between $25' < r_s < 139'$) and IC (integrated over all r_s) component for several combinations of parameters. The blue line is again a reference model for NGC 6388. The following parameter values are used as sample parameters so that the predicted SR component is not in conflict with the X-ray upper limits while fitting the γ-ray upper limit for NGC 6388.

Line colours	κ (kpc^2/Myr)	B (μG)	Γ	Q_0 (erg^{-1}s^{-1})	d (kpc)	$N_{\rm tot}$	$\gamma_{\rm max}$ (TeV)
Blue	Bohm diffusion	5	2.0	6.33×10^{33}	9.9	4.6×10^5	100
Red	Bohm diffusion	1	2.0	3.47×10^{33}	9.9	5.8×10^5	100
Green	1.1×10^{-4}	2	2.3	5.21×10^{33}	9.9	5.8×10^5	30

Table 6.4: In this table I list the line colours as shown in Figure 6.3 and the parameters that chose so that the SR componet is not in conflict with the X-ray upper limits while fitting the γ-ray data.

The reference (blue line) model violates X-ray data("upper limits"), whilst red and green lines satisfy the model (i.e., they do not violate the X-ray data). I note that there are different combinations of parameters that satisfy the data constraint, e.g., small B, $\gamma_{\rm max}$ or both small Q_0 and Γ. I could not constrain the parameters for other sources as there are no X-ray data. Also, I did not constraint the *Fermi* data because we do not model the curvature component.

6.3 Ranking the GCs according to their predicted VHE flux

I applied the model described in Chapter 4 to 15 non-detected GCs and to Terzan 5 using fixed parameters (see Table 6.1). I have used the values for $N_{\rm MSP}$, e.g., Abdo et al. (2010), and $N_{\rm tot}$ values from Lang (1992) and obtained distances d and structural parameters from Harris (1996, 2010). I assumed Bohm diffusion, $\Gamma = 2.0$, and $B = 5\mu G$ as reference parameters to produce SR and IC spectra for each individual cluster.

In tables 6.5 - 6.7 at the end of this chapter, I summarised, the differential flux upper limits from the H.E.S.S. analysis, the predicted flux from the model at 1 TeV, and the ratio x = Diff $\rm F_{UL}$/Model flux between them. This was done for the following reason: if the source strength Q_0 of each cluster is multiplied by this ratio the upper limits are not violated. This is the simplest solution (but not unique) that would satisfy upper limits, keeping all other parameters fixed. If x is larger than 1, then the predicted flux is below the upper limit (i.e., the model is compatible with the upper limit). If x is smaller than 1, then the model is not compatible with the upper limit, and this can be due to so many uncertainties in the parameters; then, e.g., Q_0 may be lowered. I also compared the model flux with the upper limits for different analyses, i.e., standard, hard, and loose cuts and also for two different diffusion cases. I note that the model is compatible with upper limits for all the GCs except NGC 6388.

From Figure 6.4, it can be seen that H.E.S.S. may possibly detect three GCs, i.e., Terzan 5 (orange), 47 Tucanae (blue), and NGC 6388 (green) if the clusters were to be observed for 100 hours. 47 Tucanae and NGC 6388 are currently not detected by H.E.S.S. yet they have only been observed for about 20 hours (see Table 3.1). I note, however, that this flux prediction and therefore ranking is very sensitive to the choice of parameters (implying large errors on the predicted fluxes). The CTA will be 10 times more sensitive than H.E.S.S. and should therefore detect many more GCs (we find that more than half of the known Galactic population may be visible, depending on observation time and model parameters). However if there are many non-detection by CTA, this will imply strong parameter constraints or even model constraints (i.e., the model might be not viable any more). The top five most promising GCs for CTA are NGC 6388, 47 Tucanae, Terzan 5, Djorg 2, and Terzan 10.

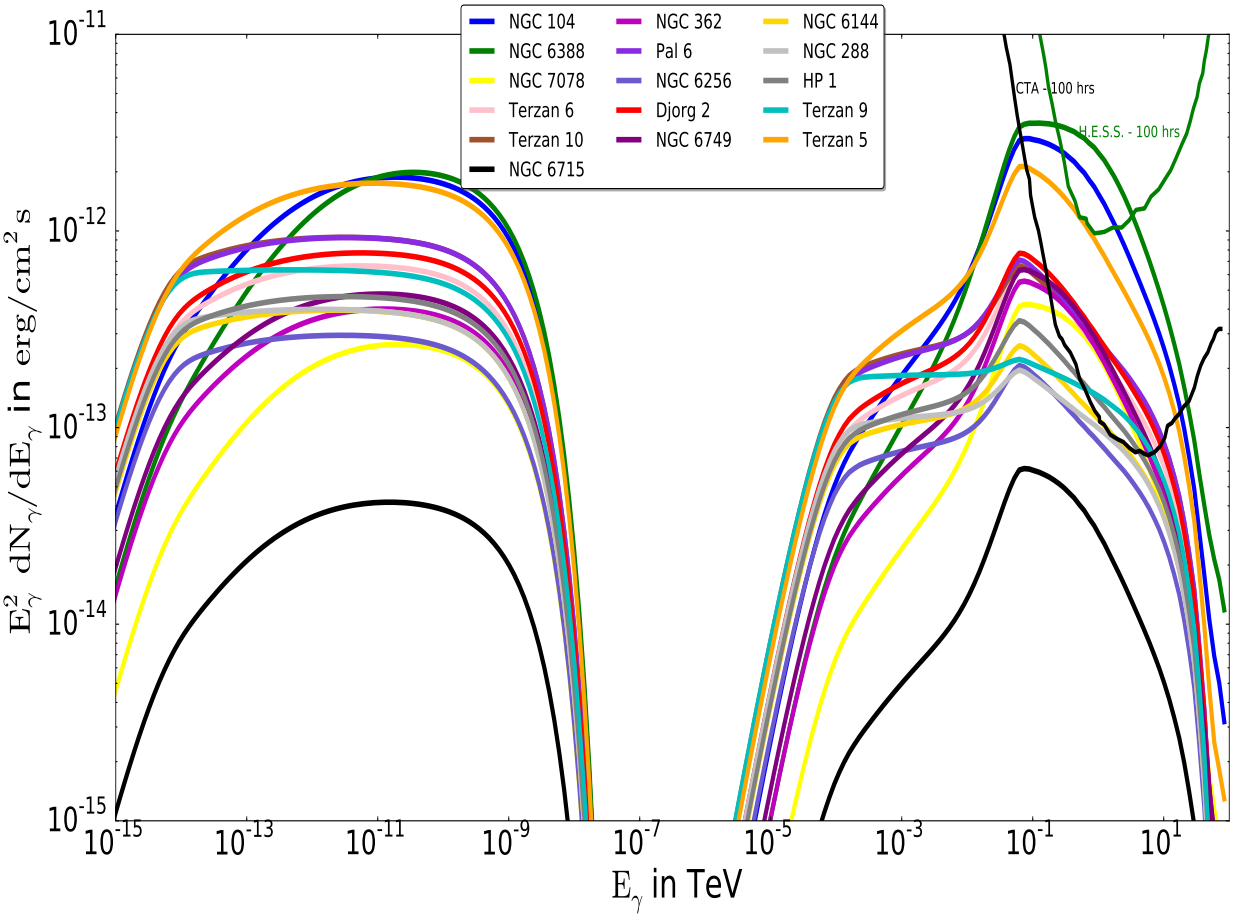

Figure 6.4: Predicted differential spectra $E_\gamma^2\, dN_\gamma/dE_\gamma$ in erg/(cm^{2}s) for 15 non-detected GCs and for Terzan 5. The two components represent the SR and IC spectra. The H.E.S.S. and CTA sensitivities (for 100 hours) are also shown. The colours indicate different GCs (see legend).

6.4 Summary

The parameters of the individual GCs are uncertain. I noted that there are different combinations of parameters that satisfy the observational constraints for three GCs. This makes parameter fitting degenerate. I also noted that only the model I present for NGC 6388 violates the observed upper limit in VHE. For the rest of the sources, the predicted fluxes are below the H.E.S.S. sensitivity limit, but CTA may detect many more GCs (possibly tens of sources) because it will be 10 times more sensitive than H.E.S.S. Future multi-wavelength studies should allow us to better constrain some parameters as well as discriminate between competing radiation models.

GC Name	Diff νF_ν upper limit at 1 TeV $\times 10^{-12}$(cm^{-2}s^{-1}TeV^{-1})	Model flux νF_ν at 1 TeV $\times 10^{-12}$(ph cm^{-2}s^{-1})	Ratio (x) Diff F_{UL}/Model flux
Standard cuts			
(i) Bohm diffusion			
NGC 104	2.7	1.5	1.8
NGC 6388	0.97	1.4	0.69
NGC 7078	0.87	0.23	3.8
Terzan 6	1.0	0.24	4.2
Terzan 10	1.1	0.28	3.9
NGC 6715	0.58	0.028	21
NGC 362	0.75	0.24	3.1
Pal 6	0.85	0.28	3.0
NGC 6256	3.4	0.084	40
Djorg 2	1.7	0.2	6.8
NGC 6749	1.4	0.14	10
NGC 6144	4.3	0.11	39
NGC 288	0.38	0.098	3.9
HP 1	1.3	0.14	9.3
Terzan 9	1.2	0.14	8.6

GC Name	Diff νF_ν upper limit at 1 TeV $\times 10^{-12}$(cm^{-2}s^{-1}TeV^{-1})	Model flux νF_ν at 1 TeV $\times 10^{-12}$(ph cm^{-2}s^{-1})	Ratio (x) Diff F_{UL}/Model flux
(*ii*) $\kappa_0 = 1.1 \times 10^{-4}$kpc^2/Myr			
NGC 104	2.7	1.0	2.7
NGC 6388	0.97	0.94	1.0
NGC 7078	0.87	0.15	5.8
Terzan 6	1.0	0.19	5.3
Terzan 10	1.1	0.24	4.6
NGC 6715	0.58	0.021	28
NGC 362	0.75	0.16	4.7
Pal 6	0.85	0.24	3.5
NGC 6256	3.4	0.074	46
Djorg 2	1.7	0.20	8.5
NGC 6749	1.4	0.13	11
NGC 6144	4.3	0.10	43
NGC 288	0.38	0.095	4.0
HP 1	1.3	0.12	11
Terzan 9	1.2	0.14	8.6

Table 6.5: This table contains information about the differential flux upper limits at 1 TeV from the analysis using standard cuts; differential fluxes at 1 TeV from the model, and the ratio of the differential flux upper limits to the predicted model flux.

GC Name	Diff νF_ν upper limit at 1 TeV $\times 10^{-12}$(cm^{-2}s^{-1}TeV^{-1})	Model flux νF_ν at 1 TeV $\times 10^{-12}$(ph cm^{-2}s^{-1})	Ratio (x) Diff F_{UL}/Model flux
Hard cuts			
(i) Bohm diffusion			
NGC 104	3.0	1.5	2.00
NGC 6388	0.78	1.4	0.56
NGC 7078	1.4	0.23	6.09
Terzan 6	0.68	0.24	2.83
Terzan 10	1.3	0.28	4.64
NGC 6715	0.45	0.028	16.1
NGC 6362	1.5	0.24	6.25
Pal 6	0.4	0.28	1.54
NGC 6256	2.5	0.084	29.8
Djorg 2	1.2	0.25	4.80
NGC 6749	1.5	0.14	10.7
NGC 6144	3.1	0.11	28.2
NGC 288	0.45	0.098	4.59
HP 1	0.97	0.14	6.93
Terzan 9	1.2	0.14	8.57

GC Name	Diff νF_ν upper limit at 1 TeV $\times 10^{-12}$(cm^{-2}s^{-1}TeV^{-1})	Model flux νF_ν at 1 TeV $\times 10^{-12}$(ph cm^{-2}s^{-1})	Ratio (x) Diff F_{UL}/Model flux
(*ii*) $\kappa_0 = 1.1 \times 10^{-4}$kpc^2/Myr			
NGC 104	3.00	1.0	3.00
NGC 6388	0.78	0.94	0.83
NGC 7078	1.4	0.15	9.33
Terzan 6	0.68	0.19	3.58
Terzan 10	1.3	0.24	5.42
NGC 6715	0.45	0.021	21.4
NGC 6362	1.5	0.16	9.38
Pal 6	0.43	0.24	1.79
NGC 6256	2.5	0.074	33.8
Djorg 2	1.2	0.20	6.00
NGC 6749	1.5	0.13	11.5
NGC 6144	3.1	0.10	31.0
NGC 288	0.45	0.095	4.74
HP 1	0.97	0.12	8.08
Terzan 9	1.2	0.14	8.57

Table 6.6: This table contains information about the differential flux upper limits at 1 TeV from the analysis using hard cuts; differential fluxes at 1 TeV from the model, the ratio of the differential flux upper limits to the predicted model flux.

GC Name	Diff νF_ν upper limit at 1 TeV $\times 10^{-12}$(cm^{-2}s^{-1}TeV^{-1})	Model flux νF_ν at 1 TeV $\times 10^{-12}$(ph cm^{-2}s^{-1})	Ratio (x) Diff F_{UL}/Model lux
Loose cuts			
(i) Bohm diffusion			
NGC 104	2.0	1.5	1.33
NGC 6388	0.96	1.4	0.69
NGC 7078	0.99	0.23	4.30
Terzan 6	0.74	0.24	3.08
Terzan 10	1.2	0.28	4.29
NGC 6715	0.78	0.028	27.9
NGC 6362	0.67	0.24	2.79
Pal 6	0.71	0.28	2.54
NGC 6256	3.6	0.084	42.9
Djorg 2	2.0	0.25	8.00
NGC 6749	0.94	0.14	6.71
NGC 6144	4.9	0.11	44.6
NGC 288	0.55	0.098	5.61
HP 1	1.2	0.14	8.57
Terzan 9	1.2	0.14	8.57

GC Name	Diff νF_ν upper limit at 1 TeV $\times 10^{-12}$(cm^{-2}s^{-1}TeV^{-1})	Model flux νF_ν at 1 TeV $\times 10^{-12}$(ph cm^{-2}s^{-1})	Ratio (x) Diff F_{UL}/Model lux
(*ii*) $\kappa_0 = 1.1 \times 10^{-4}$kpc^2/Myr			
NGC 104	2.0	1.0	2.00
NGC 6388	0.96	0.94	1.02
NGC 7078	0.99	0.15	6.60
Terzan 6	0.74	0.19	3.89
Terzan 10	1.2	0.24	5.00
NGC 6715	0.78	0.021	37.1
NGC 6362	0.67	0.16	4.19
Pal 6	0.71	0.24	2.96
NGC 6256	3.6	0.074	48.7
Djorg 2	2.0	0.2	10.0
NGC 6749	0.94	0.13	7.23
NGC 6144	4.9	0.1	49.0
NGC 288	0.55	0.095	5.79
HP 1	1.2	0.12	10.0
Terzan 9	1.2	0.14	8.57

Table 6.7: This table contains information about the differential flux upper limits at 1 TeV from the analysis using loose cuts; differential fluxes at 1 TeV from the model, the ratio of the differential flux upper limits to the predicted model flux.

Chapter 7

Summary, Conclusions, and Future Work

This study focused on analysing VHE H.E.S.S. data and constraining model parameters for Galactic GCs using γ-ray and X-ray data, with the main aim being to study the detectability of GCs for H.E.S.S. and CTA. I used a leptonic emission code that models the SEDs of GCs by solving a Fokker-Planck-type transport equation. I accumulated necessary parameters for 16 Galactic GCs in order to rank them according to their predicted TeV flux. The main results found from the analysis and the constraining of model parameters will be summarised below.

7.1 H.E.S.S. Observations and Data Analysis

H.E.S.S. has accumulated more data since the previous analysis of 15 Galactic GCs (with no reported detection) and I therefore reanalysed H.E.S.S. data to investigate whether I could find deeper flux upper limits that would be more constraining for the GC emission model. I also analysed H.E.S.S. data in the direction of Terzan 5. I applied the HAP analysis chain for three different cuts, i.e., standard, hard, and loose TMVA cuts. The significances for all GCs were below the threshold of 5σ, except for Terzan 5, which was detected with a significance of 6σ for standard and loose cuts, and 7.1σ for hard cuts. I compared my results to the previous results of Abramowski et al. (2013) and found that for most of the GCs, the differential flux upper limits of the previous analysis was generally deeper than those of the current analysis. This was because Abramowski et al. (2013)

had lower energy thresholds and they used a different analysis chain whilst I used HAP. Also, the energy thresholds obtained with standard cuts were generally slightly higher for the current analysis than in the previous one. I noted that the upper limits were similar to published results, but less constraining. In addition to the above analysis, I also analysed data for some GCs that have been observed by H.E.S.S. and detected by *Fermi* LAT. I again obtained significances below the threshold of 5σ required for a firm detection by H.E.S.S. The total detection significance for the stacking analysis was 2.4σ (for standard cuts, Abramowski et al. (2013)) and I obtained 0.1σ for standard cuts. I found that the energy threshold for the previous study were quite similar to my results i.e., the 2013 results using standard cuts are not that different from my results that were obtained using standard cuts. In addition to this analysis, I also checked the entire Harris catalogue (Harris, 2010) to see if there were new data for some sources. I found data for a few sources, but their significances were also below the 5σ level. I also performed a stacking analysis for 15 non-detected sources to increase the sensitivity, and found that the total detection significance was 0.1σ for standard cuts, 0.6σ for hard cuts, and -0.9σ for loose cuts, which are well below the 5σ-thresholds. The new data therefore do not provide any more constraints than what was published before.

7.2 Parameter Study

I next performed a parameter study with the modelling code by varying the following parameters: the number of stars $N_{\rm tot}$, the magnetic field B, the spectral index Γ of injection spectrum, the electron source strength Q_0, the distance to the cluster d, and the diffusion coefficient κ. Close to the core, diffusion dominated, but for the low-energy particles IC also had some effect. At larger radii, SR dominated. Thus, varying these parameters lead to varying escape and radiation timescales, which in turn influenced the leptonic spectral shape. Since the particle spectrum changed, the SED was different. For a summary of effects on the particle spectrum and radiated SED refer to Tables 5.2 and 5.3.

7.3 Spectral Modelling of Globular Clusters

I constrained the model parameters by selecting some combinations of parameters, i.e., B-field, diffusion coefficient κ, spectral index Γ, normalisation constant Q_0, and the maximum energy $\gamma_{\rm max}$. I found that $\gamma_{\rm max}$ could be varied between 30 TeV and 100 TeV for Terzan 5 and the B-field between 1 μG and 4 μG while still fitting the SED by fixing the other parameters. The parameters of the individual GCs were uncertain and I noted that there were different combinations of parameters that satisfied the observational constraints (i.e., they were degenerate). The main aim of the project was to study the detectability of GCs for H.E.S.S. and CTA. I ran the GC emission code using typical model parameters and structural characteristics of GCs, e.g., assuming Bohm diffusion, $\Gamma = 2.0$, and $B = 5$ μG to produce SR and IC emission components for all the selected GCs and rank them according to their predicted flux.

I also noted that most of the GCs were below the H.E.S.S. sensitivity limit, and that CTA might detect many more GCs (possibly more than half of the known Galactic population, depending on observation time and model parameters), the top five most promising GCs being NGC 6388, 47 Tucanae, Terzan 5, Djorg 2, and Terzan 10. This was because CTA will be 10 times more sensitive than H.E.S.S. On the other hand, H.E.S.S. may detect two more GCs, i.e., 47 Tucanae and NGC 6388, if the clusters were observed for 100 hours.

Future multi-wavelength studies should allow us to constrain some parameters better as well as discriminate between competing radiation models.

7.4 Future work

The GC emission model I used assumed embedded pulsars in the clusters to be the sources of relativistic particles that are injected at the core of the cluster. It also assumed cluster stars to have the same mass. As a next step, one may improve the current emission model in several respects:.

- The current emission model can be improved by modelling the effect of stellar winds from the red giant population to the existing model (Bednarek et al., 2016). Such additional bulk flow may impact the convective properties of the emitting particles injected by the embedded

pulsars, leading to sources with X-ray and γ-ray morphologies that depart from spherical symmetry.

- The effect of different positions of pulsars in the cluster may be investigated, departing from the assumption that they are all situated in the cluster centre. This will also lead to morphological changes in the emission from the cluster (Bednarek et al., 2016).

- The effect of including stars with a range of masses and surface temperatures may also be investigated. This should be done consistently, so as to reproduce the measured Hertzsprung-Russell (HR) diagram as well as the surface-brightness (King) profile in the optical band. Such a refinement will influence the background soft-photon field, because the individual stars radiate as blackbodies, and the surface temperature of each star should be a function of its mass. This will lead to an improved treatment of particle transport and the IC spectral calculations. However, this will require some substantial effort and I anticipate that a Monte Carlo approach may be more amenable to solving the particle transport equation.

- Using a refined model, as well as the latest multi-wavelength data, one may be able to constrain several model quantities. This will increase our understanding of the cluster environment, e.g., constraining the cluster magnetic field and particle diffusion coefficient. Furthermore, continued confronting of the model with more detailed spectral data will constrain the properties of the particle sources, e.g., the number of embedded millisecond pulsars as well as their average rotational spin-down and their average efficiency of converting their rotational energy into particle acceleration. This will present a substantial contribution to the Galactic science of *Fermi* LAT, H.E.S.S., the future CTA and that of satellites operating in lower wavebands.

- If new data become available, especially those taken by H.E.S.S. Phase 2, one can analyse these data to further constrain the low-energy part of the TeV spectrum. H.E.S.S. Phase 2 has a much lower energy threshold than H.E.S.S. Phase 1, reaching tens of GeV, and it also overlaps with *Fermi*'s energy range. Accumulated *Fermi* data may also play an important role here (i.e., upper limits around tens of GeV).

- In addition to modelling individual clusters, one can make predictions about the population of Galactic GCs. A refined code will predict what fraction of the Galactic population would be

visible for CTA. Such an approach would also yield constraints on ensemble averages of several parameters by comparing model predictions with the results from stacked data analyses.

Bibliography

Abdo, A. A., et al. 2010, A&A, 524, A75

Abramowski, A., et al. 2011, A&A, 531, L18

—. 2013, A&A, 551, A26

Aharonian, F., et al. 2006a, A&A, 457, 899

—. 2006b, ApJ, 636, 777

Anderhub, H., et al. 2009, A&A, 498, 83

Becker, W., Huang, H. H., & Prinz, T. 2010, ArXiv e-prints

Bednarek, W. 2012, J. of Phys, 39, 065001

—. 2013, Astroparticle Physics, 43, 81

Bednarek, W., & Sitarek, J. 2007, MNRAS, 377, 920

Bednarek, W., Sitarek, J., & Sobczak, T. 2016, MNRAS, 458, 1083

Bednarek, W., & Sobczak, T. 2014, MNRAS, 445, 2842

Benacquista, M. J. 2002, Living Reviews in Relativity, 5, doi:10.1007/lrr-2002-2

Benedict, G. F., McArthur, B. E., Fredrick, L. W., et al. 2002, AJ, 123, 473

Blumenthal, G. R., & Gould, R. J. 1970, Rev. Mod. Phys., 42, 237

Büsching, I., et al. 2011, International Cosmic Ray Conference, 7, 32

Carr, J. 2016, in European Physical Journal Web of Conferences, Vol. 121, European Physical Journal Web of Conferences, 04004

Carretta, E., Gratton, R. G., Clementini, G., & Fusi Pecci, F. 2000, ApJ, 533, 215

Chaboyer, B. 1999, Globular Cluster Distance Determinations, ed. A. Heck & F. Caputo (Dordrecht: Springer Netherlands), 111–124

Chen, K. 1991, Nature, 352, 695

Cheng, K. S., Chernyshov, D. O., Dogiel, V. A., Hui, C. Y., & Kong, A. K. H. 2010, ApJ, 723, 1219

Clapson, A.-C., Domainko, W., Jamrozy, M., Dyrda, M., & Eger, P. 2011, A&A, 532, A47

Daum, A., et al. 1997, Astroparticle Physics, 8, 1

de Naurois, M., & Rolland, L. 2009, Astropart. Phys., 32, 231

Domainko, W. F. 2011, A&A, 533, L5

Eger, P., & Domainko, W. 2012, A&A, 540, A17

Eger, P., Domainko, W., & Clapson, A.-C. 2010, A&A, 513, A66

Feenberg, E., & Primakoff, H. 1948, Phys. Rev., 73, 449

Feldman, G. J., & Cousins, R. D. 1998, Phys. Rev. D, 57, 3873

Ferraro, F. R., Dalessandro, E., Mucciarelli, A., et al. 2009, Nature, 462, 483

Freire, P. C. C., et al. 2011, Science, 334, 1107

Gast, H., et al. 2011, International Cosmic Ray Conference, 7, 158

Gendre, B., Barret, D., & Webb, N. 2003, A&A, 403, L11

Giebels, B. 2013, ArXiv e-prints

Gratton, R. G. 1998, MNRAS, 296, 739

Harding, A. K., Usov, V. V., & Muslimov, A. G. 2005, ApJ, 622, 531

Harris, W. E. 1996, AJ, 112, 1487

—. 2010, arXiv:1012.3224

Hui, C. Y., Cheng, K. S., & Taam, R. E. 2010, ApJ, 714, 1149

Hui, C. Y., Cheng, K. S., Wang, Y., et al. 2011, ApJ, 726, 100

Iben, I., & Renzini, A. 1984, Phys. Rep., 105, 329

Jimenez, R. 1998, Proceedings of the National Academy of Science, 95, 13

Jimenez, R., Thejll, P., Jorgensen, U. G., MacDonald, J., & Pagel, B. 1996, MNRAS, 282, 926

Johnson, T. J., et al. 2013, ApJ, 778, 106

Jones, F. C. 1968, Phys. Rev., 167, 1159

Jørgensen, B. R., & Lindegren, L. 2005, A&A, 436, 127

Kopp, A., Venter, C., Büsching, I., & de Jager, O. C. 2013, ApJ, 779, 126

Krauss, L. M., & Chaboyer, B. 2003, Science, 299, 65

Lang, K. R. 1992, Astrophysical Data I. Planets and Stars, Berlin: Springer-Verlag

Lanzoni, B., Ferraro, F. R., Dalessandro, E., et al. 2010, ApJ, 717, 653

Li, T.-P., & Ma, Y.-Q. 1983, ApJ, 272, 317

Longair, M. 1992, High Energy Astrophysics (Cambridge University Press)

—. 2011, High Energy Astrophysics (Cambridge University Press)

Massari, D., Ferraro, F. R., Dalessandro, E., et al. 2013, Memorie della Societa Astronomica Italiana, 84, 236

Milone, A. P., Bedin, L. R., Piotto, G., & Anderson, J. 2009, A&A, 497, 755

Moskalenko, I. V., & Strong, A. W. 1998, ApJ, 493, 694

Mould, J., & Aaronson, M. 1979, ApJ, 232, 421

Nolan, P. L., et al. 2012, ApJS, 199, 31

Pan, Z., Hobbs, G., Li, D., et al. 2016, MNRAS, 459, L26

Paredes, J. M., Reimer, O., & Torres, D. F. 2008, The Multi-Messenger Approach to High-Energy Gamma-Ray Sources, 1st edn., Vol. 309 (Berlin: Springer)

Parker, E. N. 1965, P&SS, 13, 9

Prinsloo, P., Venter, C., Büsching, I., & Kopp, A. 2013, in Proc. SAIP 2013, (arXiv:1311.3791)

Renzini, A., Bragaglia, A., Ferraro, F. R., et al. 1996, ApJ, 465, L23

Rowell, G. P. 2003, A&A, 410, 389

Rybicki, G. B., & Lightman, A. P. 1979, Radiative processes in astrophysics (New York, Wiley-Interscience)

Sebastian, F. 2005, Online Analysis of Gamma-ray Sources with H.E.S.S., Unpublished diploma dissertation, Humboldt University, Berlin, Germany

Strader, J., Brodie, J. P., Cenarro, A. J., Beasley, M. A., & Forbes, D. A. 2005, AJ, 130, 1315

Swordy, S. 2008, The Astronomer's Telegram, 1422

Tam, P.-H. T., Hui, C. Y., & Kong, A. K. 2016, Journal of Astronomy and Space Sciences, 33, 1

Tam, P. H. T., Kong, A. K. H., Hui, C. Y., et al. 2011, ApJ, 729, 90

Teshima, M. 2008, The Astronomer's Telegram, 1491

Van den Berg, D. A., Bolte, M., & Stetson, P. B. 1996, ARA&A, 34, 461

Venter, C., & de Jager, O. C. 2005, ApJ, 619, L167

—. 2008, ApJ

—. 2010, ApJ, 725, 1903

Venter, C., de Jager, O. C., & Clapson, A.-C. 2009a, ApJ, 696, L52

Venter, C., Harding, A. K., & Guillemot, L. 2009b, ApJ, 707, 800

Venter, C., & Kopp, A. 2015, Proc. SAIP2014, ed. C Engelbrecht and S Karataglidis, ISBN: 978-0-620-65391-6, 394

Vercellone, S. 2014, Nuclear Instruments and Methods in Physics Research, 766, 73

Weekes, T. C., , et al. 1989, ApJ, 342, 379

Wei, D. M., Cheng, K. S., & Lu, T. 1996, ApJ, 468, 207

Wu, E. M. H., et al. 2014, ApJL, 788, L40

Zhang, L., Chen, S. B., & Fang, J. 2008, ApJ, 676, 1210

Zhang, P. F., Xin, Y. L., Fu, L., et al. 2016, MNRAS, 1603.02358